Synthesis, Morphological and Photophysical Characterization of Squaraine Based Chromophores

Preface

This master´s thesis titled “Synthesis, Morphological and Photophysical Characterization of Squaraine based Chromophores” was performed at the department of chemistry at NTNU in Trondheim, during spring 2019.

The greatest of thanks to my awesome supervisor Solon Oikonomopoulos who has provided me with all the information, instrument guidance and general tips and tricks needed to make this master´s thesis a reality.

A huge thanks to my family for being the wonderful supportive bunch they are, and for always lending a hand whenever I am in need of one.

An aditional tanks to Sindre Stene for luuking over my English gramar and fur drenking beer witt me after long labratory days.

Anche un grazie a Velia per essere stata un grande motivazione per me in questo semestre.

Mats Henden *11/06/2019*

SAMMENDRAG

I dette studiet har squaraine-kinolin kromoforer blitt undersøkt mot deres fotofysiske, elektrokjemiske og morfologiske egenskaper. Effekten av forskjellige alkylkjeder på stoffenes adferd ble undersøkt ved bruk av absorpsjon (UV / vis), steady-state og time-resolved emisjonsspektroskopi. Morfologisk karakterisering ble utført ved hjelp av atomkraftmikroskopi. Til sist ble en utvalgt kromofor brukt til fremstilling av organiske solceller.

Høye aggregeringstendenser, følsomhet for løsningsmiddelendringer samt lav alkylkjedebidrag ble funnet til å dominere i fotofysiske egenskaper. Morfologiske forandringer på grunn av alkylkjede og løsningsmiddelforskjeller samt aggregering av høy orden ble avslørt og brukes til å forklare fotovoltaisk effektivitet. Et valgt fargestoff ble sent til videre solcelleprøving som en elektrondonor og viste moderat effektomformingseffektivitet (n = 0,02%) på grunn av omfattende krystallinitet som alvorlig hindret solcellens morfologi. En analyse av grunner for lav effektivitet ble gjort for å hjelpe fremtidig syntetisk forskning.

ABSTRACT

In this study, squaraine quinoline chromophores has been investigated towards their photophysical, electrochemical and morphological properties. The effect of different alkyl chains on the behavior of the dye was explored via the use of absorption (UV/vis), steady state and time-resolved emission spectroscopy. Morphological characterization was carried out using atomic force microscopy. Finally a selected dye was used for the fabrication of organic solar cells.

High aggregation tendencies, susceptibility to solvent changes and low alkyl chain contribution were found to dominate in photophysical properties. Morphological changes due to alkyl chain and solvent differences and high order aggregation were also revealed. A selected dye was chosen for further solar cell testing as an electron donor which revealed moderate power conversion efficiencies (n = 0.02%) due to extensive crystallinity that severely hampered the morphology of the solar cell. An analysis of the reasons for poor efficiency was carried out to help guide future synthetic attempts.

SYMBOLS AND ABBREVIATIONS

^{1}HNMR	Proton nuclear magnetic resonance
^{13}CNMR	Carbon-13 nuclear magnetic resonance
AFM	Atom force microscopy
BHJ	Bulk hetero junction
COSY	Correlation spectroscopy
d	Doublet in NMR
dd	Doublet of doublets in NMR
DMF	Dimethylformamide
DPV	Differential pulse voltammetry
DSSC	Dye sensitized solar cell
EDG	Electron donating group
E_g	Energy band gap
eq	Equivalent
EQE	External quantum efficiency
EtOAc	Ethyl acetate
EWG	Electron withdrawing group
eV	Electron Volt
FAB	Fast electron bombardment
FF	Fill factor
HMBC	Heteronuclear multiple-quantum correlation spectroscopy.
HOMO	Highest occupied molecular orbital
HSQC	Heteronuclear single-quantum correlation spectroscopy
IR	Infra-red spectroscopy
J_{sc}	Short circuit current
L_d	Exciton diffusion length
LUMO	Lowest unoccupied molecular orbital
M	Molar
m	Multiplet in NMR
MeOH	Methanol
MHz	Mega Hertz
mM	Millimolar
mmol	Millimol
MOS	Metal oxide semiconductor
mV	Millivolt
nm	Nano meter
NMP	N-methylpyrrolidone
NMR	Nuclear magnetic resonance
NTNU	Norwegian University of Science and Technology
OPV	Organic photovoltaics
Ox	Oxidation
p	Pentet in NMR
PCE	Power conversion efficiencies
$Pd(OAc)_2$	Palladium (II) acetate
PL	Photoluminescence
PMT	Photomultiplier tube
ppm	parts per million

Red	Reduction
RPM	Rounds per minute
s	Singlet in NMR
S*	Excited state of the molecule
SPhos	2-Dicyclohexylphosphino-2',6'-dimethoxybiphenyl
t	Triplet in NMR
TCSPC	Time-correlated single photon counting
THF	Tetrahydrofuran
TLC	Thin layer chromatography
UV	Ultraviolet
UV-Vis	Ultraviolet-visible spectroscopy
V	Volt
Vis	Visible
V_{oc}	Open circuit voltage
W	Watt
µL	Microliter
%T	%transmittance

Introduction

Squaraine dyes have gained considerable attention due to their remarkable optical characteristics, durable zwitterionic structure, simple synthetic route and susceptibility towards environmental influence [1, 2]. These dyes are characterized by their electron deficient cyclobutene core derived from squaric acid and have been exploited for the purpose of applications such as ion sensing, photovoltaics and imaging [3-5]. The theory part of this study begins with Kasha´s exciton theory, which will be explained to present a basic understanding of how aggregation works in general, and is an important section that sets the precedence for various interpretations in the "Results and Discussion" part of this thesis. Afterwards some literature will be presented as a means to acquire an intuition of how squaraines and aggregation are affected by changes in environment such as temperature and solvents, as well as a brief introduction to symmetric/asymmetric molecule differences and more direct changes like extending the pi-system, incorporating electron donating or withdrawing groups and polymerization. These will be reviewed with regards to optical property changes. The dyes in this study has been synthesized for BHJ OPV application, however since a substantial portion of reference material are obtained from DSSC related work, a basic working principle for both applications have been added. Moreover, simple synthetic variations on the functional end of the molecule allows for DSSC applications.

The most important understanding one can obtain before the results are discussed lies within the instruments themselves and therefore, the theoretical part will end with the general working principles of instruments used.

This study has primarily focused on photophysical and morphological properties. It should be noted that this is a continuation of a previous study which has had a larger focus on synthesis. Therefore theoretical background regarding the reactions are not presented here, but are thoroughly explained with additional interesting details in reference [6] and is a recommended read.

1. Theory

1.1 Kasha´s Exciton Theory [7].

To explain the reason for aggregate behaviour, one must firstly be familiar with how dipole moments vary between a single dye molecule and its aggregate, i.e. the transition dipole moment and how excited electrons behave according to this difference. The dipole moment can be considered a vector where the arrow goes towards the electron withdrawing parts of the molecule dye. An exciton is a combination of an electron in the LUMO and a positive hole in the ground state of a molecule, i.e. an excited molecule. The time a electron stays in a LUMO energy level is a key factor underlying this understanding.

Based on the exciton theory by Kasha *et. al*. When a monomer with a certain dipole moment vector adds up with another of same species (aggregates to dimer), two extreme cases may occur. A vector of same magnitude (90^0) can be formed or they can cancel each other out (180^0). In the first case, the dipole moment would remain the same as a monomer, hence the excited electron would stay in the LUMO for the same amount of time. In the second case the vectors would add up to zero, hence, no dipole moment for the aggregate is formed. This means that the excited electron path from S to S* or back would have no difference, hence a very fast relaxation would occur. Keep in mind that there are many factors which affect excimer behaviour and that these two extreme cases have been strongly exaggerated opposed to how it really works. Below are the concepts of H- and J-aggregates in the two extreme cases and how they would affect an absorption spectrum .

H-aggregates

This type of aggregation can first and foremost be observed by a positional change in spectral bands such as absorption and emission spectra to a shorter wavelength (higher energy - hypsochromic shift). These changes in shift positions are commonly caused by a face to face aggregation of dye molecules, and are correlated to a very small difference between the dipole moment of the monomer and that of its aggregate. Figure 1 shows a simple schematic of how two different extreme alignments of dipole moments give a hypsochromic shift in absorption

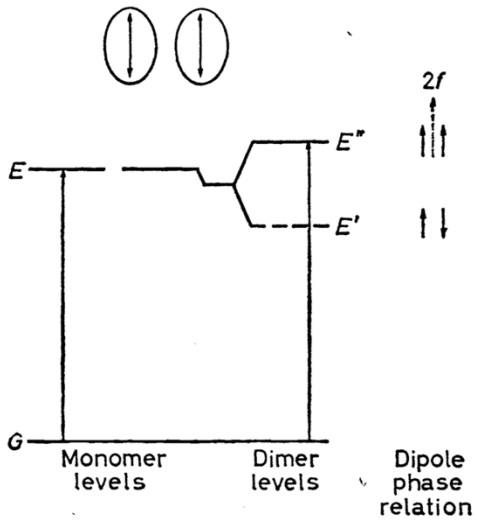

Figure 1 Face-to-face aggregation (Hypsochromic shift) exciton theory

spectra, i.e. higher energy shift. The first excited state (E´) has an alignment resulting in cancelation of dipole moment, hence the LUMO electron population here will be negligible due to very fast relaxation. The other alignment does, however, form a larger dipole moment, causing accumulation of the electron population which is detectable by UV/vis. This "allowed" face to face enhanced transition dipole moment will in most cases exhibit a higher degree of electrostatic repulsion, causing the higher energy blue shift.

J-aggregates

J-aggregates tend to cause a change in spectral band shift to peaks in a higher wavelength region, namely a bathochromic shift (lower energy). These aggregates can mostly be categorized as "edge to edge", or rather "head to tail" orientation of the dipole moments between monomers. Head-to-tail alignment of monomers tend to form aggregates which strengthens their dipole moment relative to the monomeric specie. This difference in molecular dipole moment between monomer and aggregate causes a larger transition dipole moment upon photon absorption, stabilizing the lower level of the exciton band (E´) leading to accumulation of electron population in this state, which is what causes the bathochromic shift. Figure 2 shows a typical absorption spectra containing both H- and J-aggregates, while Figure 3 presents a simplified schematic of exciton theory for absorption behaviour of J-aggregates

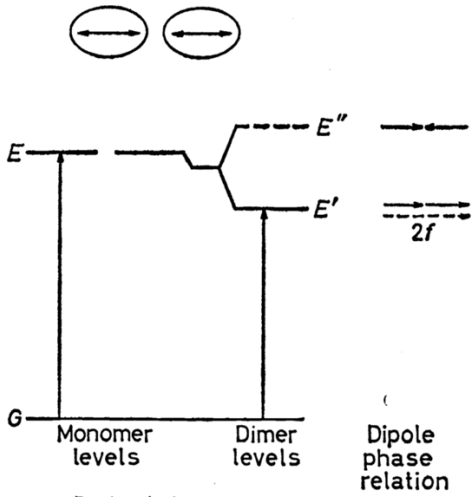

Figure 3 simplified schematic of exciton theory for absorption behaviour of J-aggregates

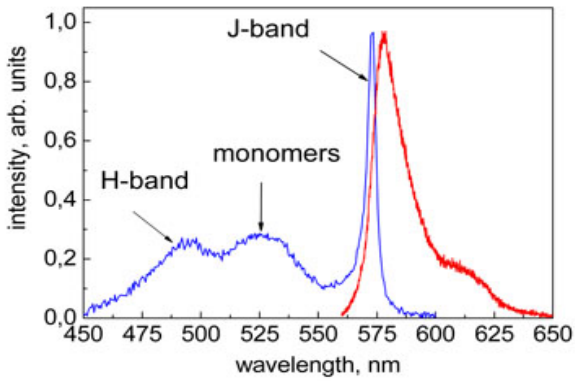

Figure 2 Typical absorption (blue curve) and luminescence (red curve) spectra of J-aggregates

H- and J-aggregates different Co-planar Angles.

In reality H- and J-aggregates will occur somewhere in between these extreme cases, whereas the magnitude of exciton band splitting would depend on the angle (**σ**) between the dipole moment vectors (Figure 4). The general rule is that an increase of repulsion (higher energy) between the monomers will increase the splitting magnitude of the exciton bands. The meeting point of E´ and E´´ at $54{,}7^0$ marks the point of difference of wether it is an H- (right side) or J-aggregate (left side). Note that this is the case of coplanar inclined transition states.

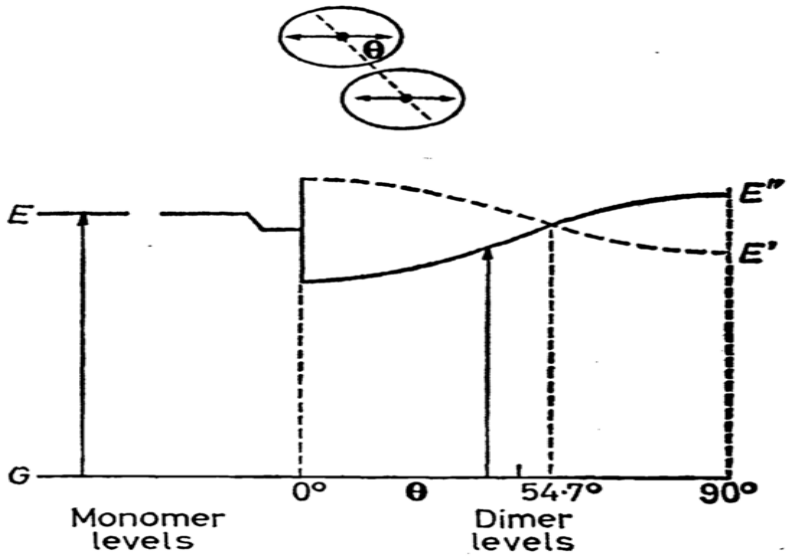

Figure 4 Exciton band energy diagram for a molecular dimer, or a double-molecule, with coplanar transition dipoles inclined to interconnected axis by angle.

1.2 Aggregation in Squaraine Based Dyes.

Aggregation, or self-association between dye molecules is a phenomenon that causes alterations in dye-molecule´s structural and optoelectronic abilities. Therefore aggregation plays an important role in how a selected dye will perform in a variety of applications such as in solar cells, in photodynamic therapy, optical pulse suppressor etc [8, 9]. There are to my knowledge not any, to date, effective ways to predict dye aggregation *a priori* and its effect in opto-electronic devices. However, extensive literature is available, regarding aggregation in a vast number of different dyes, in which one may obtain a certain intuition regarding the nature of this phenomena. This section will mainly focus on relatively simple squaraine based dyes and some studies relating to this thesis will be presented. At the section end there will be a small summary in which the most interesting notions are reiterated and an explanation is attempted

on the basis of Kasha´s exciton theory. During this section and beyond, technical terms like H-aggregation (face to face alignment) and J-aggregation (head to tail alignment) will be used.

1.2.1 Effect of Solvent.

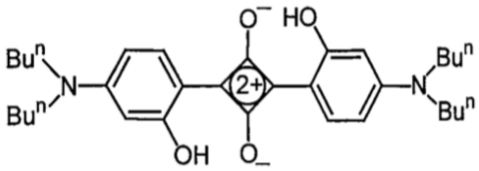

Figure 5 Structure of SQ-2 [10]

Naturally, solvent polarity and squaraine dye solubility in the specific solvent is of great importance with regards to aggregation. It was reported that SQ-2 (Figure 5) showed two different types of aggregation and that the preference for one over the other was strongly dependent on the H_2O/DMSO co-solvent composition. One specific composition revealed a dynamic conversion from J-aggregates to H-aggregates in 70% H_2O/DMSO for SQ-2. Hence, composition of a binary solvent system can surely be utilized to control squaraine dye aggregation [10].

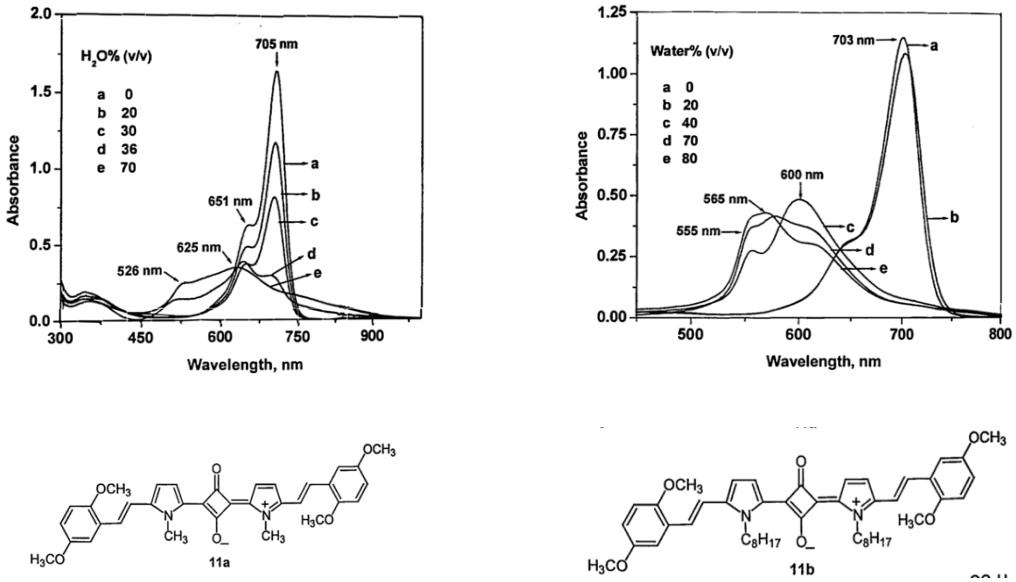

Figure 6 Molecule structure and absorption spectra of SQ-11a (left) and SQ-11b (right) in different H2O/DMSO compositions [11].

It should be stressed that aggregation in squaraine dyes could be highly dependent on the structure of the dye itself. In Figure 6 the absorption spectra of SQ-11a and SQ-11b can be viewed. These dyes are of equal character except for that SQ-11b contains longer alkyl side chains. Even though the change in dye structure is small, it had, according to the study a considerable effect on aggregation tendencies during the course of increasing water ratio from 0 – 70/80% in the H_2O/DMSO solvent. As can be seen, the longer chain SQ-11b shifts peak

maxima from its J-aggregate to its monomer and finally to its H-aggregate, whereas its short chain equivalent (SQ-11a) loses its J-aggregate maxima in favor of its monomer maxima over the same composition course [11]. An interesting observation here is that the absorbance of these squaraine dyes does not change from J-aggregation to monomer or H-aggregation peaks until the H_2O/DMSO composition surpasses 30%. Since DMSO is a solvent capable of only accepting hydrogen bonding, it will act antagonistically to water´s hydrogen bond ability towards the dye, hence this binary solvent is well suited for investigating gradual hydrogen bonding effects.

To look further into the concept of polar solvents and squaraine aggregation, there has been a study conducted concerning the two squaraines SQ 1 and SQ 2 presented in Figure 7.
It was observed that protic-solvents would cause a hypsochromic shift (blue shift) in absorption and emission spectra, as well as a decrease of fluorescence quantum yield in these two dyes. These effects were intensified by increasing hydrogen bonding ability of the solvent. It was postulated that the change of optical behavior corresponded to hydrogen bonding of solvent towards the oxygen atoms at the cyclobutene core [12].

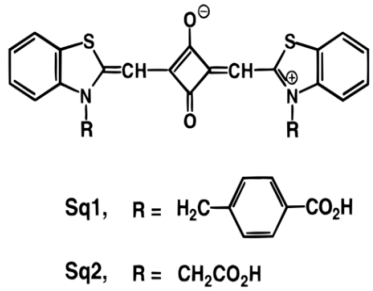

Figure 7 Molecular structure of SQ1 and SQ2 [12]

Aprotic nonpolar solvents however, have been shown to exhibit a preference for J-aggregation in the squaraine dyes depicted in Figure 8. The absorption spectra of the Sq-Br dye shown in Figure 9 revealed that addition of toluene shifted the spectra in favor of J-aggregation. H-bonding solvents, such as methanol and acetone were later introduced, which caused the absorption spectra to revert into being dominated by monomer maxima peak absorption. Similar observations was also made for SQ-I [13]. It should be noted that these squaraines are particularly prone to Ph changes due to their para-OH-groups in halogenated benzene structures.

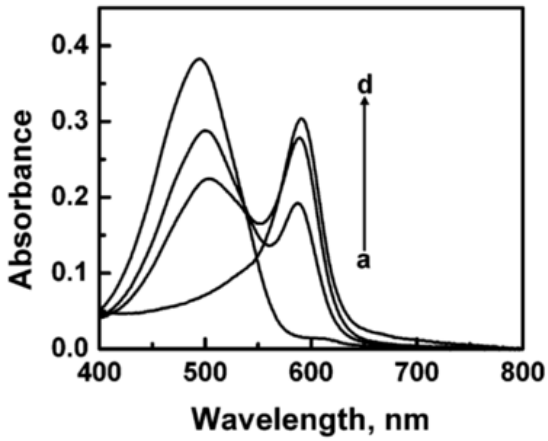

Figure 9 Absorption spectra of SqBr (13,6uM) in acetonitrile with different toluene proportions (a) 0, (b) 70, (c) 80 and (d) 90% [13].

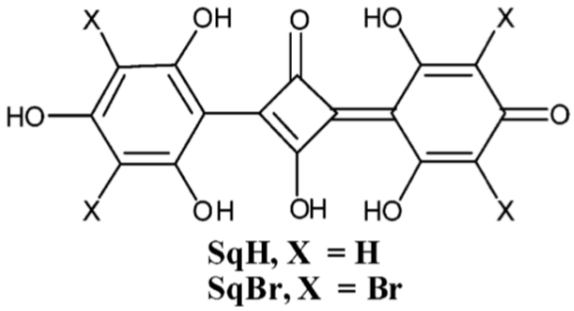

Figure 8 Molecular structure of Sq-Br [13].

1.2.2 Effect of Temperature.

Dye solutions have a tendency to exhibit a lesser concentration of aggregates in higher temperatures than it would in lower temperatures. The potency of the temperature effect will also be closely related to the solubility of the dye in given solute. Hence enhanced solubility due to temperature changes will be inversely proportional to aggregate concentration [9, 14]. Figure 10 shows the effect of temperature on the squaraine dye (SQ-5), whereas peak at 600 nm belongs to the monomer and 500 nm peak to its H-aggregate.

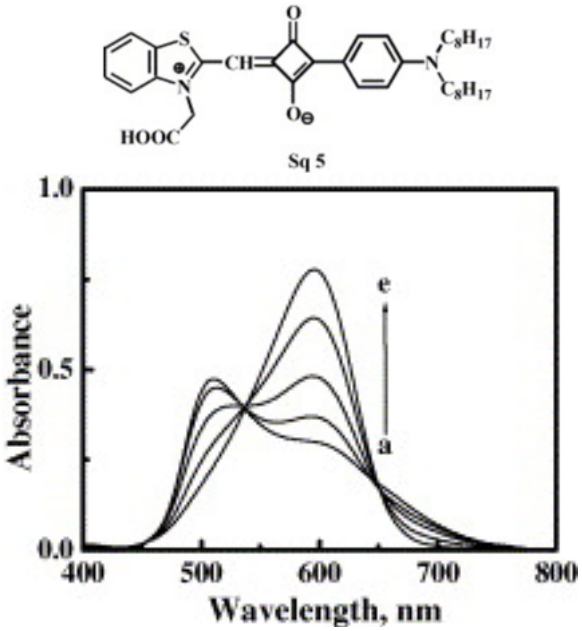

Figure 10 Effect of temperature on the absorption spectra of the dye Sq5 (10.3 × 10⁻⁶ mol dm⁻³) in 50% water–methanol solvent mixture, (a) 25°C, (b) 35°C, (c) 55°C, (d) 65°C, and (e) 70 °C [14].

1.2.3 Molecule Symmetry.

Most studies revolve around the synthesis of symmetrical squaraines, yet unsymmetrical molecular structures of these dyes are also predicted to have a large impact on aggregation behavior and optical properties. It is found that symmetrical squaraine dyes would obtain an increase of electron density towards the cyclobutene center after a HOMO→LUMO excitation. The unsymmetrical dyes, however, tend to form a unidirectional electron flow from one end to the other upon excitation, which may be considered favorable for organic solar cell injection properties [14, 15]. A study in which the unsymmetrical squaraine; USQ-1 (Figure 12) was tested and tuned for ion sensing properties found that this particular dye exhibited both H- and J-aggregates in near equal preference upon gradually changing solvent from AcOH to water (Figure 11). An observation supporting the simple postulation, that unsymmetrical molecule structures may cause irregular association arrangements in solvents [16].

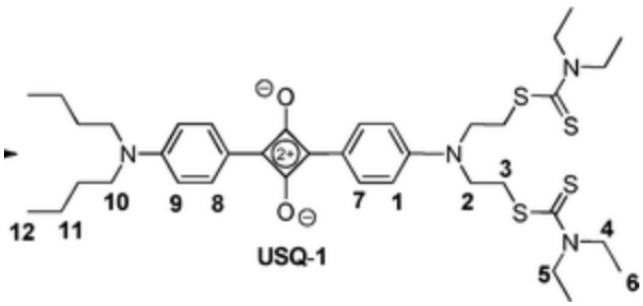

Figure 12 Molecular structure of USQ-1 [16].

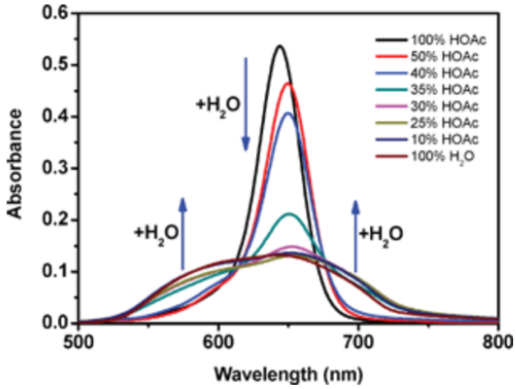

Figure 11 Absorbance of USQ-1 in solvents of different HOAc/H_2O ratios [16].

1.2.3 Section Summary.

Hydrogen bonding properties of the solvent tend to apprise the formation of H-aggregation in simple squaraine dyes, probably due to hydrogen bonding between solvent and the oxygen groups of the cyclobutene core [17-19]. Using hydrogen bonding to stabilize the squaraine core may cause head to head association between two squaraine monomers if they exhibit availability due to less electrostatic repulsion. Furthermore, an increase of hydrophobic side groups in squaraines have a tendency to increase the rate of aggregation in polar protic solvents. On the other side, nonpolar solvents like toluene and benzene etc. seem to have the opposite effect and promotes J-aggregation in squaraine dyes. Since J-aggregation is a head to tail

transition dipole enhancement, it would be reasonable to call this aggregation the “naturally preferred” one if outside influence is limited. Hence the solubility in nonpolar aprotic solvents could intuitively be the most influential factor on whether monomer or J-aggregate will have peak maxima absorption. The aggregation behavior of unsymmetrical squaraines in different solvents may be more complicated as their structure could cause irregular and less predictable intermolecular associations in response to external change.

1.3 Molecular Engineering and Opto-electro Attributes.

Perhaps of even greater importance is the knowledge of how the structure of squaraine dyes themselves impact the optoelectrical performance exhibited, and further how the dye can be tuned and molecularly engineered to behave in one´s own image. This section will present a couple of major intramolecular influences which can be utilized for this purpose, namely; incorporation of π-system altering groups, mobility restriction, redox properties, and lastly, polymerization. As in the previous section, this too will be presenting several studies from literature to exemplify and visualize the various consequences of direct intramolecular alteration of squaraine dyes.

1.3.1 Electron Donating and Withdrawing Groups (EDG and EWG).

The use of EWG/EDG in organic synthesis has been of great value in organic optoelectronic material synthesis during the last two decades. The careful selection and coupling of EDG with EWG groups has allowed a facile and dependable route for energy bandgap tuning and optimization. This synthetic route came to be commonly referred to as “the donor-acceptor synthetic approach”. Electron withdrawing groups (EWG) are those that are able to withdraw electron density from a π-system, while electron donating groups (EDG) will donate electron density to a π-system. For the purpose of visualization, the effects of EWG and EDG the HOMO/LUMO of a benzene ring will be explained in accordance with Figure 13.

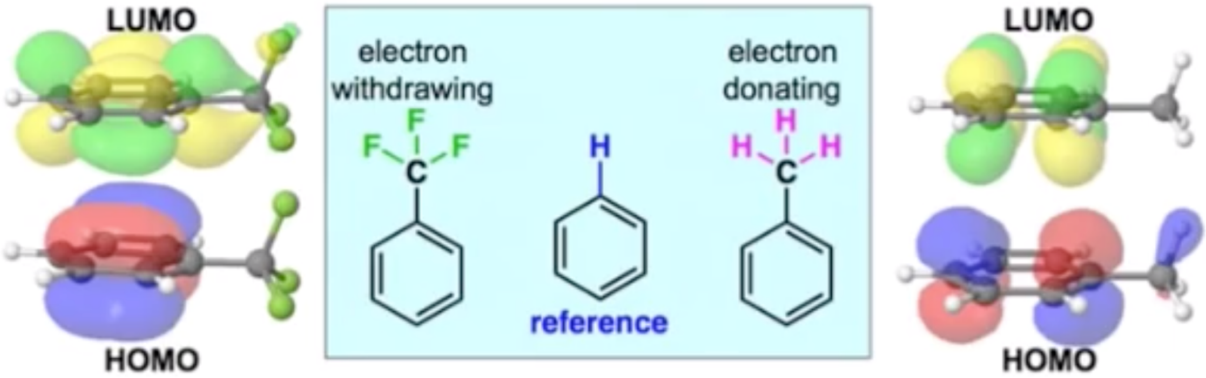

Figure 13 EWG and EDG substituted benzene rings [20].

EWG will have their greatest influence on the LUMO of the benzene and will in the case of the fluoroform group, affect it through inductive π to σ^*, π-type interaction which depletes the electron density of benzene. In contrast EDG will mostly affect the HOMO of benzene which in the case of methyl is a inductive σ to π^*, π-type - interaction, enhancing electron density [20]. The key information here is that EWGs tend to change the LUMO levels of a π-system while the HOMO levels remain fairly unchanged, EDGs, however, have the complete opposite effect.

The effects of EDGs and EWGs can indeed be utilized to alter the energy bandgap of squaraine dyes to cause a blue hypsochromic shift or a red bathochromic shift in absorption spectra. *Paterno et al*. conducted a study where they observed the optical changes following a direct EWG functionalization of the cyclobutene core. The three squaraine dyes VG-1, VG-2 and VG-4 were chosen for the study and two of these had EWG substituents (Figure 14). As can be viewed by the absorption spectra, there were two distinct differences between EWG substituted squaraines compared to that of VG-1. Firstly, the appearance of two new absorbance peaks at 380 and 460nm belonging to the EWG-substituted squaraines. This observation was linked to the disruption of molecular symmetry from all-trans to all-cis conformation in which could result in a higher energy $S_0 - S_2$ transition state for the squaraines. The second observation was the bathochromic shift of the peak maxima which would be the effect of the EWG lowering the LUMO energy level of the pi-system [21].

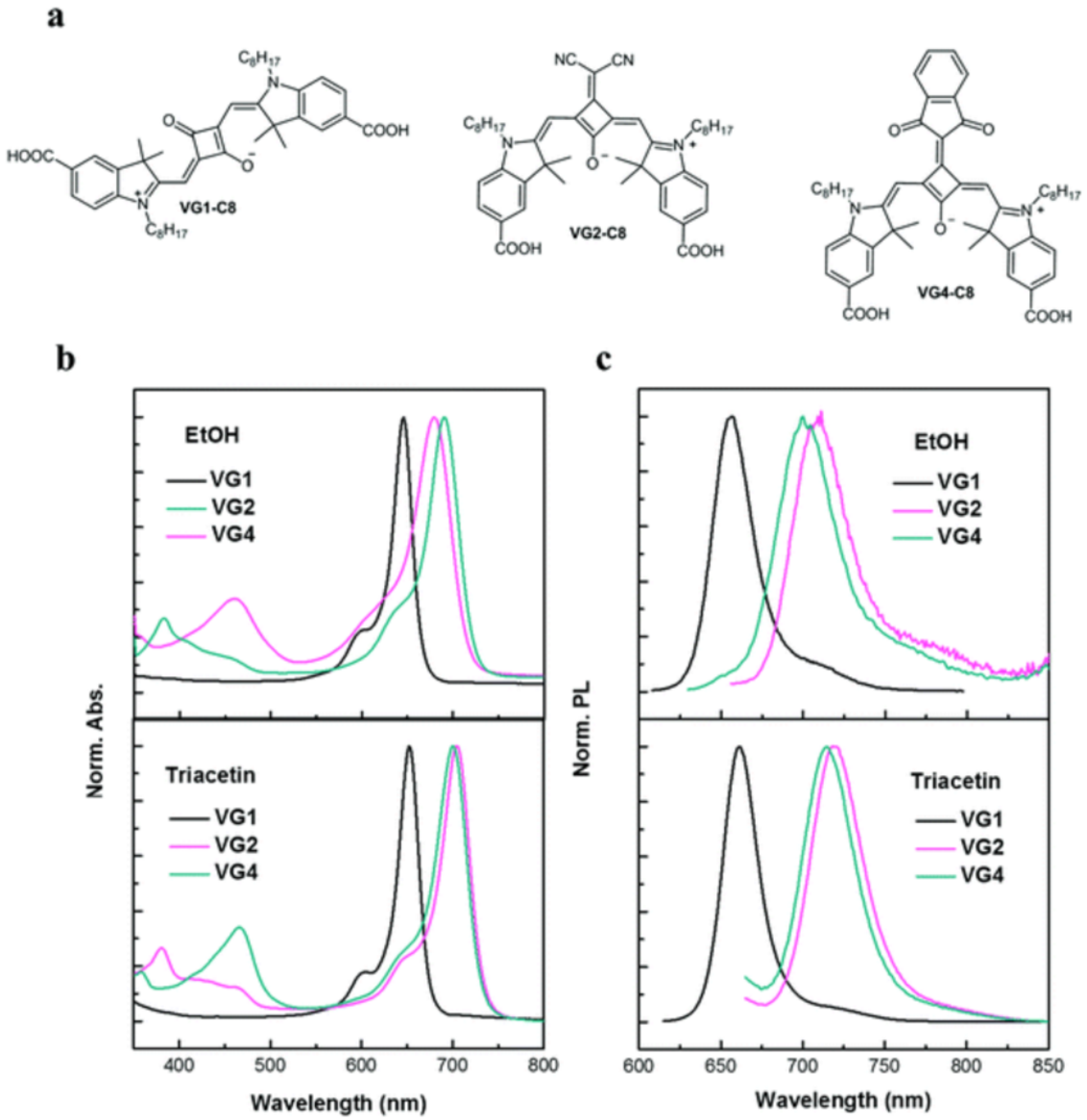

Figure 14 (a) molecular structures of VG-1, VG-2 and VG-4. (b) UV/vis absorption and (c) PL-spectra for the three dyes in ethanol (top) and Triacetin (bottom) [21].

1.3.2 Restricting Intra-molecular Mobility

As mentioned in the DSSC trap states section (Chapter 1.4.1); excitons which perform any configurational change will cause a loss of radiational (emission) energy in the form of vibrational energy. A study conducted on the photochemistry of squaraine dyes measured the lifetime of SQH and SQOH (Figure 15), it was found that the exciton lifetime of SQOH was twice as long as SQH. This was attributed to the hydrogen bonds generated between the hydroxy groups and the squaric oxygen groups and serve as an example of how restricting vibrational relaxation may lead to

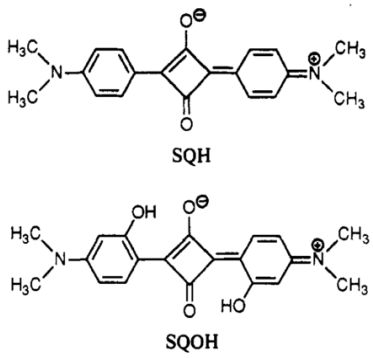

Figure 15 Squaraine dyes: SQH and SQOH [22].

longer exciton lifetime. It was also found that these two dyes inhibited similar lifetimes in the triplet excited state, hence, in this case, the triplet excited state decay was not impacted by intramolecular hydrogen bonding [22].

1.3.3 Redox Properties in Squaraine Dyes [23].

In order to investigate the redox properties of squaraines with extended conjugation, Busches et al. conducted cyclic voltammetry and spectroelectrochemical analysis (Figure 16) of the three squaraine dyes shown in scheme 1.

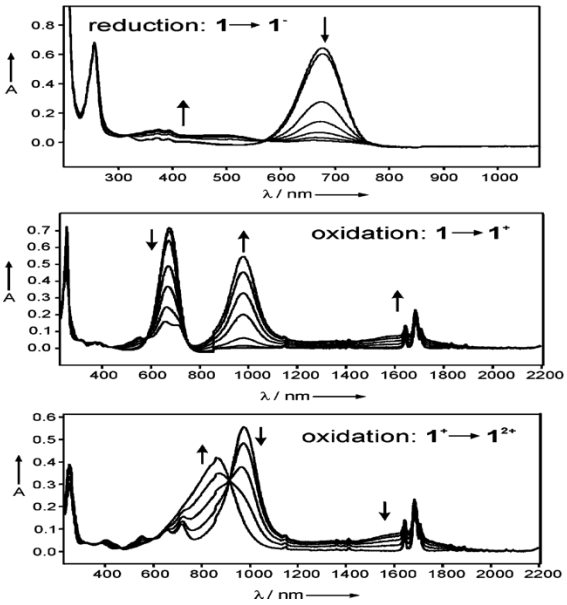

*Figure 16 UV/vis/NIR spectroelectrograms of **1** [23]*

*Scheme 1 Molecular structure of compound **1, 2** and **3** [23]*

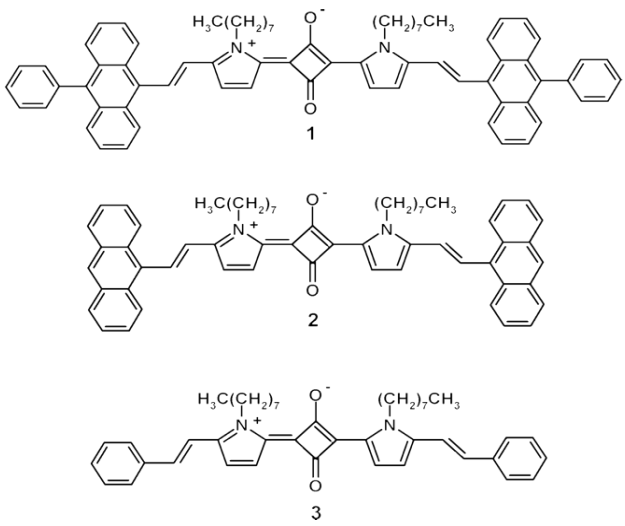

The study revealed that the phenylanthracenyl units of compound **1** had a remarkable ability to act as effective redox centers in an oxidative process of the squaraine based dye. By AM1 level calculations it was predicted that these peripheral groups further extended positive charge distribution among the anthracene sub-structures, hence stabilizing cation/dication formation considerably compared to compound **2** and **3**. A noteworthy observation was that the half-wave reduction potentials of the three compounds had little difference from one to the other, hence, negative charge is localized in the pyrrole-squaraine-pyrrole unit since this was a constant core of all the compounds. Figure 17 presents the AM1 calculations of the single electron oxidized compound **1**

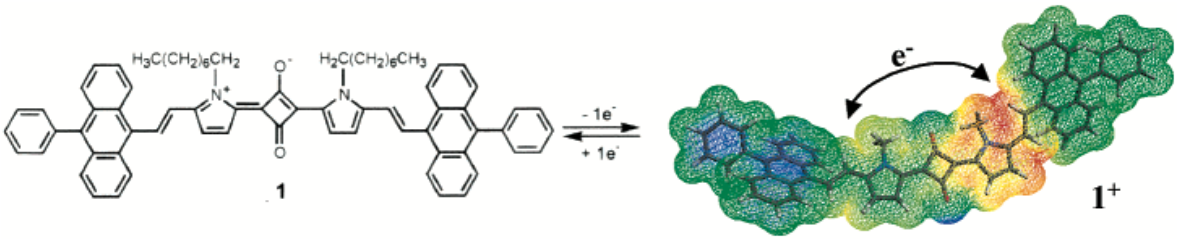

*Figure 17 Calculated charge distribution in **1**$^{+}$ [23].*

Figure 16 shows the UV/vis/NIR spectroelectrograms of compound **1**. One electron reduction resulted in a radical anion with limited stability and new absorption behavior which could be fully reverted by reoxidation, indicating electrochemical switching properties. As can be seen, one electron reduction also caused a complete loss of transition charge transfer, postulating that reduction of squaraine dyes cause severe changes to the acceptor (cyclobutene) moiety and/or that radical anion dimerization may have occurred.

1.3.4 Polymerization

Squaraine based dyes may have their optical absorption properties extended to the NIR region of the spectrum by incorporating strong EDGs to the cyclobutene moiety, extending the conjugated system or by improving molecular rigidity [24]. These factors may all be addressed by polymerizing donor-acceptor-donor squaraine monomers into larger pi-delocalized structures. It is, however, crucial that pi-delocalization works harmoniously, i.e. there must be a convenient bridging between these D-A-D monomers which restricts their ability to create "individual" electron density systems within the polymer should such be the case. To exemplify the consequences of simply adding D-A-D monomers to squaraine based oligomers or polymers, a study of the squaraine polymers (Scheme 2) was conducted.

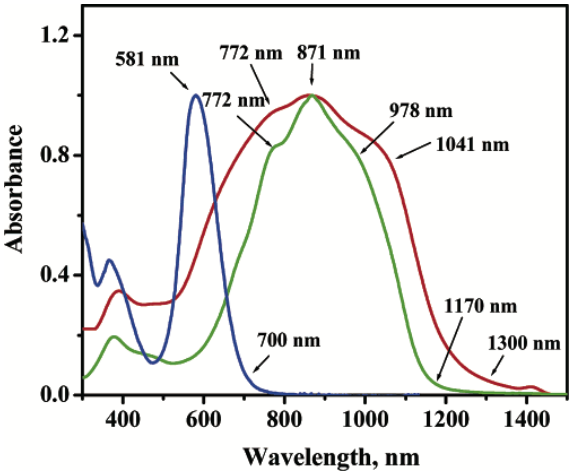

Scheme 2 Molecular structures of 15 and 29a-d [3]

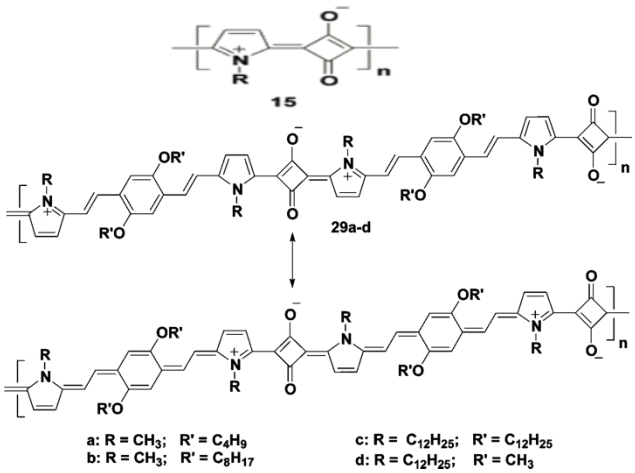

*Figure 18 Absorption spectra of polysquaraines **15**(blue, R= $C_{12}H_{25}$),**29a** (red), and **29d** (green), which show the remarkable shift in the absorption spectra of **29a** and **29d** [3].*

As exhibited by the absorption spectrum (*Figure 18*) of the polysquaraines **15** and **29a-29d** it can be concluded that bridging D-A-D monomers with an electron rich dialkoxydivinyl-phenyl moieties may enhance electron flow through the system, hence giving red shifted broad absorption capabilities. It should be noted that the squaraine polymer **15** did not differ much in optical properties to that of its monomer, further supporting that only extending these conjugated systems are not sufficient to markedly lower the energy band gap. It can also be an indication towards identifying the exciton diffusion length of the molecule, which is directly correlated to the energy bandgap. A peculiar observation is that **29a** with shorter alkyl chains exhibited broader absorption peaks containing more shoulders than its long alkyl chain version (**29d**). This difference in optical behavior, as well as measured high polydispersity values (Mw/Mn) for these polymers, indicate that likely aggregation phenomena are taking place and that longer side chains have an inhibiting effect on aggregation [3].

Another consequence of conjugate extension and π-delocalization change is that the number of cross-sections for two-photon absorption (2PA) may remarkably increase, and was in a study found to be 3-5 times higher (per repeat unit) for a polymer (P1) than its monomer counterpart (P2) (see Figure 19). It should be noted that 2PA measurements would be detected at roughly twice the wavelength in an absorbance spectrum as it results from the emission of two photons of approximately half the energy (Figure 19). The HOMO and LUMO levels for P1 was also higher and lower respectively compared to P2, hence making it more susceptible for oxidation and reduction, as would be expected when pi-electrons are more delocalized along the polymer backbone [25].

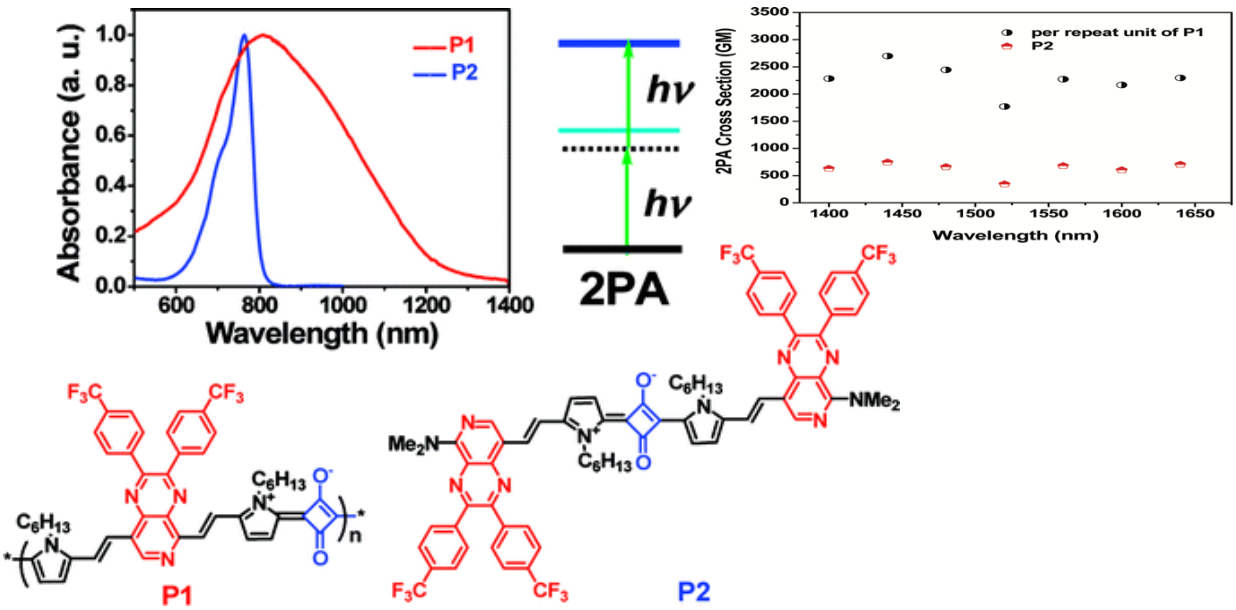

Figure 19 Molecular structures, absorbance spectrum and 2PA measurements for polymer P1 and monomer P2 [25].

1.4 Organic solar cells

1.4.1 Dye Sensitized Solar Cell (DSSC).

In 1991 Brian O´Regan and Michael Grätzel published a breakthrough in preparing an efficient dye-sensitized solar cell (DSSC) which could be prepared by low-cost materials and have a solar to energy efficiency up to 7,9% [26]. The construction of these photoelectro-chemical systems can simply be divided into three sub sequential parts: (1) a dye-coated metal oxide semiconductor (MOS) followed by (2) an electrolyte and (3) a counter electrode all which are sealed using transparent glass or polymer [27].

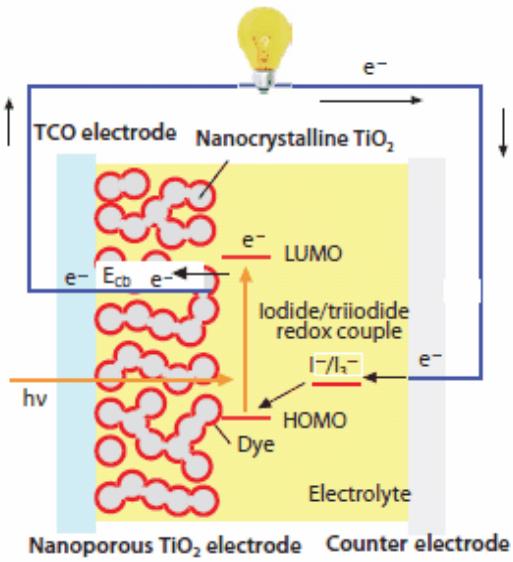

Figure 20 Schematic of a DSSC illustrating the mechanism of electric power generation. TiO_2 =MOS, Electrolyte = I^-/I_3^- [28].

As depicted in Figure 20. a DSSC will function when a dye has been excited from its ground state to its excited state via an electron going from the highest occupied molecular orbital (HOMO) to the lowest unoccupied molecular orbital (LUMO). After the excitation, this electron will be able to move via MOS to the working electrode and further to the counter

electrode. There the electron will reduce an electrolyte which in turn will be oxidized by the dye (replenishing the HOMO), completing the photoelectrochemical cycle [28].

The Dye

For the DSSC to work, it is essential that the electron contained within the excited dye´s molecule can be transferred to the MOS. For this to happen the LUMO energy state of the MOS must be lower than the LUMO energy state of the dye. Equally essential is the electrolytes oxidation potential which must be higher than the HOMO level of the dye and lower than its LUMO energy level. There are three main factors to consider when choosing an efficient dye to use for an DSSC. Namely, number of functional groups, distance from LUMO electron density area to functional group (anchoring area) and lastly the number of trap states the dye exhibits [29].

Number of Functional Groups.

In the study of DSSCs a functional group refers to the dye molecule groups which are able to form covalent bonds with the MOS. When an exciton is formed, it is via these groups it will travel to form an electrical current, hence the more functional groups attached to the MOS the more pathways will be available to the exciton. Table 1 shows that an increase from one functional group to four results in an almost quadruple increase of efficiency (n) in the case of the porphyrin based dye (Figure 21) sensitized on TiO_2 [30].

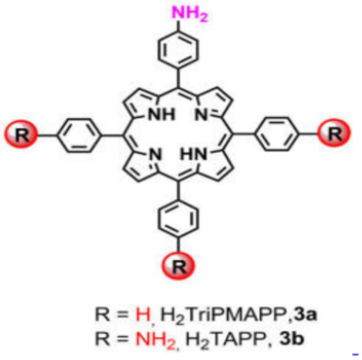

Figure 21 Porphyrin dyes [30].

Table 1 Photovoltaic parameters of free base porphyrins under 350 W/m² solar illumination with an active area of 0.15 cm² [30].

Porphyrin	V_{oc} (V)	J_{sc} (A/m²)	Fill factor	Efficiency (η)
H_2TAPP	0.547	31.67	0.595	2.94%
H_2TriPMAPP	0.502	23.44	0.545	0.7%

Distance between LUMO Electron Density Areas and Anchoring Groups.

In larger aromatic compounds the relevant electron occupying either the HOMO or LUMO orbitals will have a preference for being located in certain areas of the molecule. Literature has found that there is a significant correlation between the distance of LUMO electron density areas to anchoring groups and the short circuit current (I_{sc}) of DSSCs. Whereas higher currents are produced when the distance is smaller [31]. Figure 22 visualizes the correlation of distance from achoring group to LUMO electron density areas and photovoltaic efficiency.

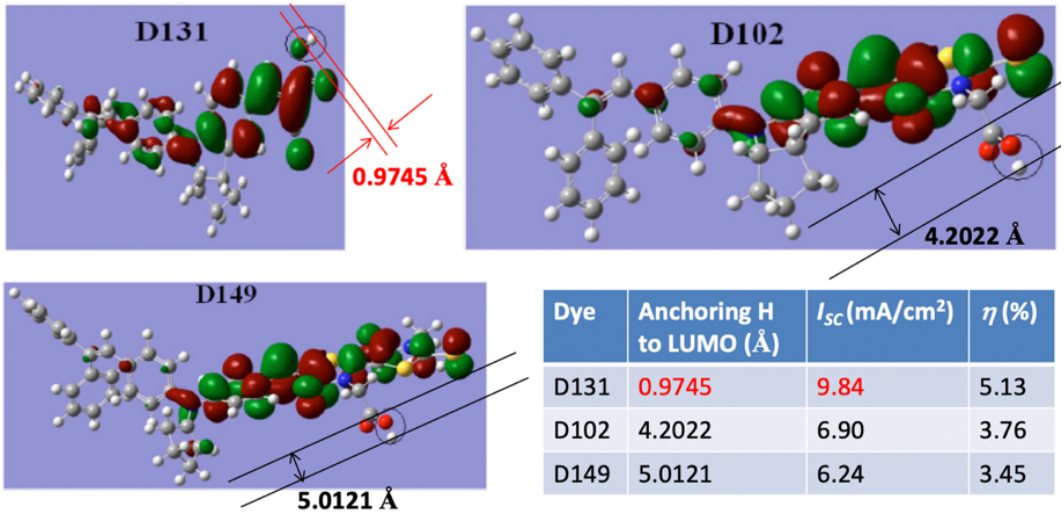

Dye	Anchoring H to LUMO (Å)	I_{SC} (mA/cm²)	η (%)
D131	0.9745	9.84	5.13
D102	4.2022	6.90	3.76
D149	5.0121	6.24	3.45

Figure 22 Correlation of anchoring H to LUMO distance and DSSC efficiency [31].

Trap States [29].

A practically unavoidable attribute of larger organic dye molecules are their ability to form trap states. These are small changes in molecule configuration which in turn alters their HOMO/LUMO energy levels, hence the mobility of the exciton will be stagnant due to lingering in possible trap states (see Figure 24). Since these trap states will have their LUMO in slightly lower energy levels, a loss of energy must have occurred as thermal energy due to configuration change. This non-radiative loss of energy is detectable by a PL-spectrometer and by combination with UV-vis adsorption measurements one can determine the extent of trap states in a dye. See Figure 23 for UV-vis & PL- graphs which depicts the absorption and emission values in the cases of: (1) No trap states and (2) trap states. The loss of energy due to trap states can be calculated using Equation 1 below.

$$Eq\ 1. \qquad Energy\ lost = \left(\frac{hc}{X1}\right) - \left(\frac{hc}{X2}\right)$$

Where X1 = absorption wavelength, X2 = Emission wavelength, h = planck´s constant, c = speed of light

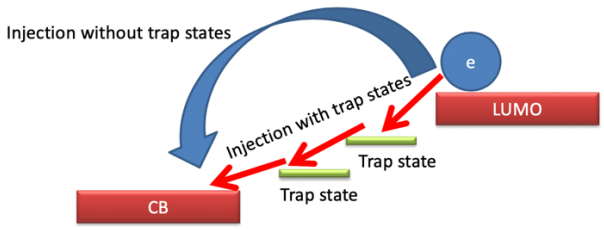

Figure 24 Electron injection path with and without trap states [29].

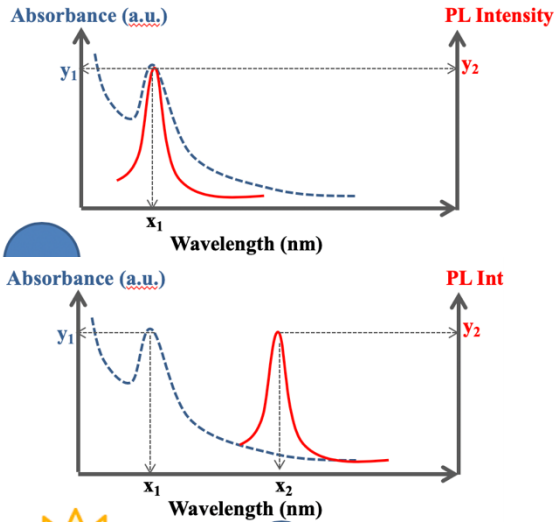

Figure 23 Photon absorption and emission. Upper spectrum shows no trap states in dye, lower spectrum shows dye with trap states [29] .

1.4.2 Bulk Heterojunction (BHJ) Organic Photovoltaic (OPV).

The principle for a BHJ OPV is mostly the same as for a DSSC; it consists of a working electrode coupled to a counter electrode, whereas a donor (dye) needs to be excited by light adsorption to form an excited electron which can be delivered to the acceptor (e.g. fullerene). However, in a BHJ OPV, the donor diffusion length plays a critical role as these cells do not use an electrolyte to complete the current and are instead dependent on charge (hole) hopping within the donor molecules from one electrode to the other. BHJ OPVs also consists solely of organic donor and acceptor compounds (DSSC is an organic/inorganic hybrid) which are mixed and annealed to a blend (as the name suggests) mixture. Figure 25 shows the working principle of an BJH OPV where an electrical current is result of four distinct steps. First, an exciton is generated as the result of the donor adsorbing a photon. The second step revolves around the exciton dissociation, causing an electron to be extracted to the acceptor material, leaving a positive charge (hole) to the donor. The separation of the charges in two different materials greatly reduces the possibility of charge recombination, one of the bottlenecks of initial OPVs. Lastly the electron travels through the electron acceptor bulk, is collected at the working electrode (cathode), travels throughout the external circuit providing the current and rejoins the hole which has been collected at the counter electrode. Also here there are several factors which

governs whether efficiency in these cells will rise or fall, such as insufficient energy for exciton splitting, charge recombination and charge trapping and of course charge mobility of the materials towards their respective charges [32]. This section will briefly introduce some key aspects of BHJ OPV´s like morphology and acceptor parameters, but will mainly focus on donor properties given at the section end.

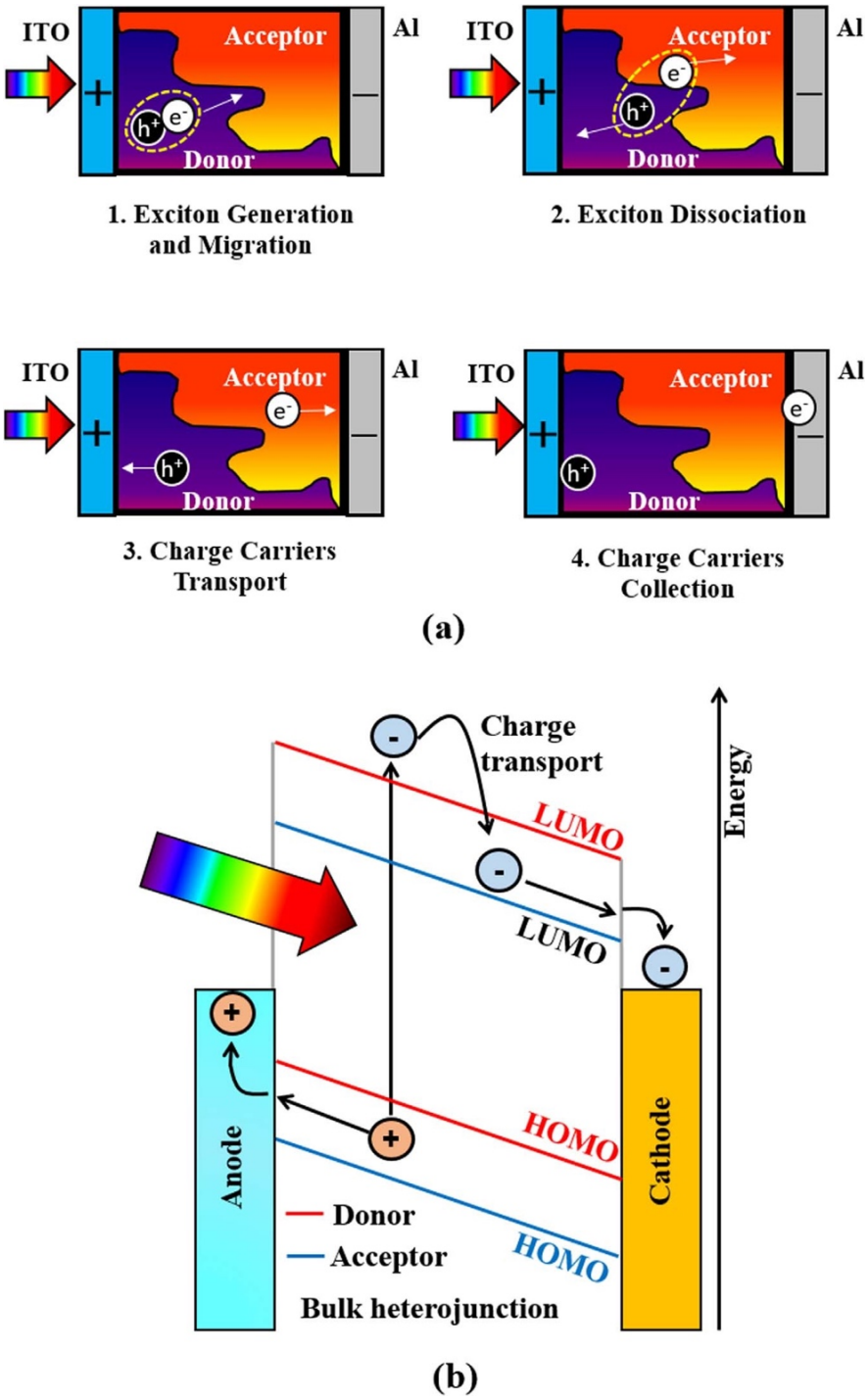

Figure 25 Working principle of a BHJ OPV device (a) shows the four distinct steps and (b) shows the electron and hole transportation for a current to occur [32].

Morphology of BHJ OPV [33].

A BHJ OPV is formed by mixing two components, namely the donor (D) and acceptor (A) via a solvent. When these components are mixed, a close to homologues mixture of A and D will initially be formed. Over time, however, A and D will start to respectively agglomerate to their own kind and phase separate. After casting of solution and the formation of a solid-state phase the separated mixture has occurred, there are two critical points which need to have been met for efficient BHJ performance. First, a maximum surface area must have formed between the two different materials, in which the length scale is appropriate in regards to the photoexcitation recombination length. Secondly the two interpenetrating component networks need to be fully connected to the electrodes.

While BHJ OPVs are governed by an, essentially, statistical distribution of the electron donor and the acceptor, there are many ways to control BHJ OPV morphology at the nanoscale, to some extent. The most important parameters are listed below:

- Choice of solvent.
- Donor and acceptor blend ratio.
- Molecular structure of materials.
- Chemical additives
- Phase separation control (i.e. thermal or solvent annealing parameters)
- Film deposition technique

Donor Molecule

A donor molecule is the equivalent of the dye in DSSCs. It is a molecule capable to absorb light to form an exciton, and in BHJ OPVs these are usually any conjugated polymer, oligomer or smaller molecule that exhibits large adsorption abilities and exciton diffusion lengths [32]. To better grasp what parameters are of importance to BHJ OPV efficiency in regards to donor capabilities, one should firstly be acquainted with the concept of exciton diffusion length (L_D), which is defined as the distance traveled by an exciton before recombination occurs [34]. In terms of BHJ cells, exciton diffusion length will be a parameter that may determine how big an area of the donor phase which efficiently takes part in the charge generation process. In short; larger diffusion length means that one may increase the donor fraction of the BHJ-cell, which in turn means more light absorption [35].

The donors investigated for BHJ OPVs have greatly focused on polymeric substances as these tend to have better film forming properties than non-polymeric substances. However, small molecule donors do offer some advantages in terms of charge transfer mobility and facile synthesis procedures [36]. As BHJ OPV efficiency is highly limited by exciton diffusion and charge carrier mobility, so is the thickness of the photoactive layer, which usually is limited to 100nm. To optimize efficiency in these cells the donor molecules should have a bandgap that overlap well with the solar spectrum i.e. low bandgap donors. To exemplify, a donor with an bandgap of 1,1 eV may cover 77% of the AM1,5 solar flux, while a bandgap of 1,9 covers 30% [37]. It is also critical that the exciton splitting at interphase layer takes place. This process is driven solely by the difference between the acceptor and donor LUMO – levels and this must be adequate to overcome the exciton binding force. Although, technically, the exciton dissociation energy is a material property, a rule of thumb is that the difference between the two materials' LUMO levels should be at least 0,3 eV [36].

While literature has had a larger focus on morphology and domain size optimization to compensate for short diffusion lengths in donors, some studies have shown that tuning the L_D itself is indeed possible. For example one study showed that diluting boron subphthalo-cyanine chloride (donor) in a host matrix with wide energy gap attributes could increase L_D by 50% [38]. While another revealed that exciton diffusion length could be almost doubled by using solvent vapor annealing instead of conventional annealing methods [39].

When testing a solar cell for efficiency, an J-V curve is what needs to be plotted. These curves give information of how well a solar cell performs with regards to what its theoretical maximum performance would be, and is in accordance with its name done by plotting the current density (J) in mA/cm^2 vs. voltage (V). Figure 26 shows a general J-V curve with abbreviated points of interest.

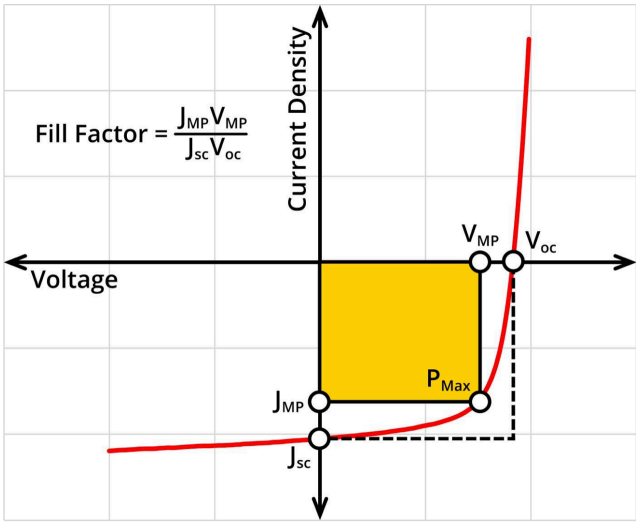

Figure 26 Genral J-V curve of a solar cell, highlighting the short-circuit current density (Jsc), open-circuit voltage (Voc), current and voltage at maximum power (J_{MP} and V_{MP}), maximum power point (P_{Max}) [40].

The Fill Factor (FF) is usually calculated to understand the overall performance of any solar cell, and it is calculated by dividing the product of the current and voltage at maximum power (J_{mp}, V_{mp}) with the product of short-circuit current density (J_{SC}) and open-circuit voltage (V_{oc}) according to Equation 2.

$$Equation\ 2. \qquad FF = \frac{Jmp * Vmp}{Jsc * Voc}$$

It is essentially, calculated by dividing the square area that governs how well the cell actually performs (at its best) by the square area which states the theoretical max of the solar cell performance. In BHJ OPVs, it has been shown that the open-circuit voltage is directly connected to the HOMO level of the donor component and the LUMO level of the electron acceptor. Meaning that tailoring the HOMO levels of dyes in BHJ OPVs also tailor the open-circuit voltage and consequently overall solar cell performance [41].

1.5 Instrument Principles

1.5.1 UV/vis Spectrophotometer

The first apparatus that is encountered when investigating how a molecule behaves in the presence of photons is the UV/vis spectrophotometer. While many different versions can be found, they all work according to one simple principle; hit a molecule with a photon and see if the photon is stopped by the molecule. In Figure 27, a simple schematic is presented to show how a basic double beam UV/vis spectrometer works.

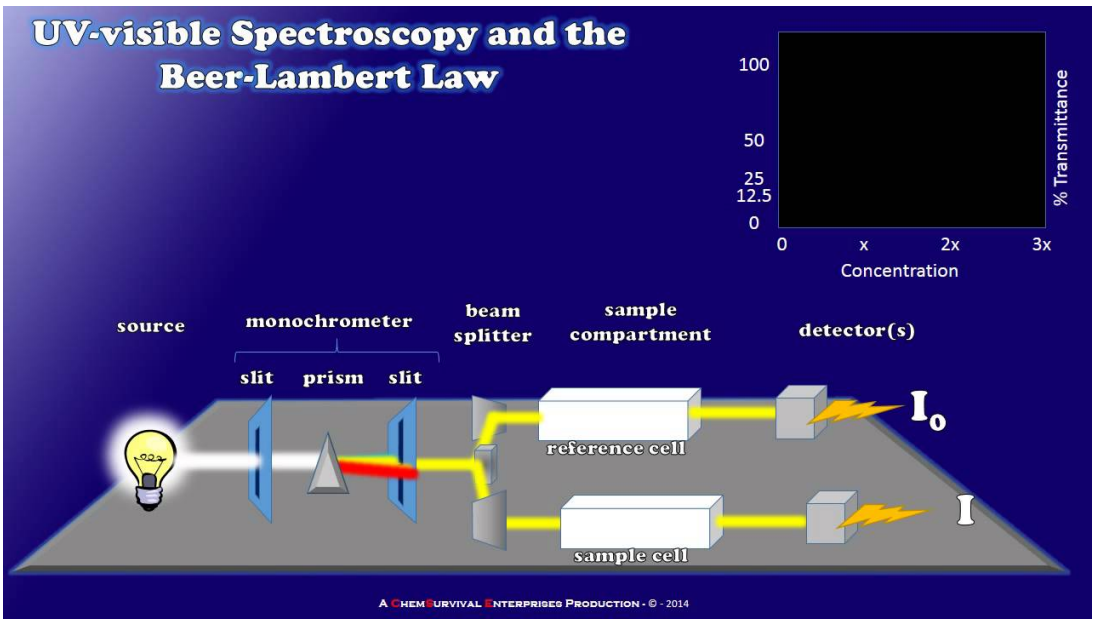

Figure 27 Schematic showing the basic principles of an UV/vis double beam instrument.

The first component to build any instrument for photophysical measurements is a source of photons. In a UV/vis apparatus this source can in principle be anything that is able to produce photons of all wavelengths in the ultraviolet and visible region of the spectrum, e.g. LED, Tungsten or a xenon arc lamp [42]. The light produced will travel through an entrance slit which leads it to a prism, whose purpose is to push each and every photon of different wavelength into their own unique direction. This way a photon beam of, say, 550 nm can be tuned towards the exit slit which leads to a device called “beam splitter”. Here the photon beam will be split into two beams of 550nm, one leading to a reference cell holding a cuvette with the designated solvent and the other to a cell containing the sample. When the two beams have passed their respective cell they will both hit their designated detector (PMT, CCD etc.), which are there to

convert photons into an electrical current that can be picked up by the computer and converted into plotting data [43].

In the upper right corner of the schematic presented is a %transmittance (%T) vs. concentration graph. When actually using a UV/vis spectrometer however, an absorption vs. wavelength graph would be obtained. Though to explain how the electrical current produced from the detectors actually gets interpreted into an absorption spectra, one first needs to know the definition of %T. Transmittance is in actuality a measurement of how many photons are received by the sample detector (***I***) as opposed to the reference detector (***I₀***). If the sample does not absorb any photons it will give a %T = 100% because the sample detector receives just as many photons as the reference detector receives. Likewise if the sample absorbs 20% of the photons, a %T = 80% is obtained because detector ***I*** receives 80% as many photons as detector ***I₀*** receives. The mathematic definition of %T is given by Equation 3.

$$Equation\ 3: \qquad \%T = \frac{I}{I_0}$$

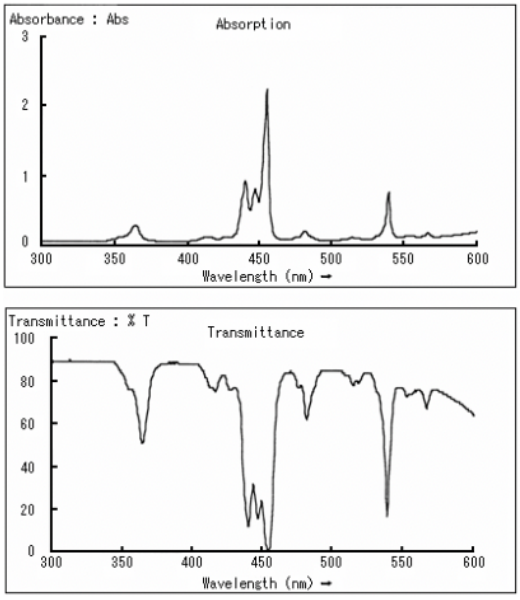

Figure 28 Absortion spectra with absorbance vs wavelength (upper) and %transmittance vs wavelength (lower)

In reality the lower spectrum shown in Figure 28 is what every UV/vis spectrometer would produce had it not been for the famous equation called the Beer Lambert law, which converts %transmittance into absorbance by taking the negative logarithm of %T. This produces both graphs that are more pleasurable to view and gives linear concentration dependent graphs which are easier to interpret (%T vs conc. gives exponential curves). It should be noted that many UV/vis spectrophotometers work via a one-beam principle (no beam splitter) in which the reference cuvette and sample have to be measured separately. The correlation between absorbance and %T is given by Equation 4 [44].

$$Equation\ 4. \qquad Abs = 2 - Log\ \%T$$

1.5.2 Time-Correlated Single Photon Counting (TCSPC) [45]

TCSPC-experiments are commonly used to perform lifetime and kinetic scan measurements as well as fluorescence imaging due to high sensitivity, data accuracy, precision and for being substantially cheaper than other ultrafast excitation systems. A TCSPC setup consists of four main components; a pulsed laser, beam splitter, time to voltage/amplitude converter (TAC) and a multichannel analyzer. Figure 29 shows a rough schematic of how these major components as well as "minor" components are synchronized to produce a lifetime histogram.

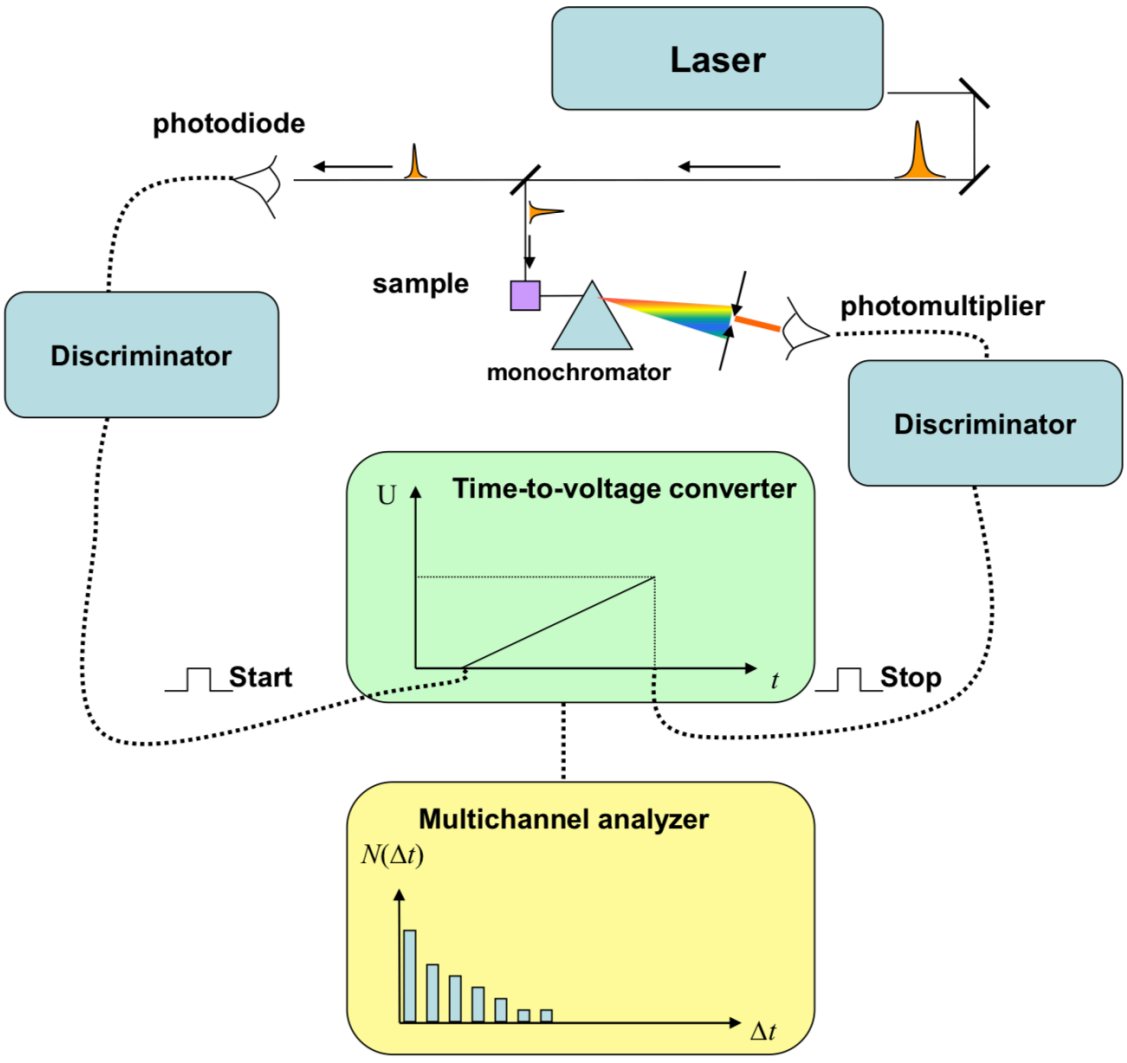

Figure 29 Simplified schematic of the working principles and components of TCSPC [45].

When the pulsed laser has been switched on, single monochromatic photons will be emitted at intervals specified by the laser pulse rate. These start by traveling to a beam splitter which splits the single photon into two components of equal character as that initially emitted, one photon

to excite the sample to be measured and the other to a photodiode. It is these two photons which set the precedence for a “start” and “stop” signal (equal in time from excitation to emission) used later by the multichannel analyzer to create a sample decay histogram.

The start signal is caused by the photon travelling towards the photodiode, essentially a “small solar cell” creating an electrical pulse when hit by a photon of sufficient energy. This current will then be transferred to what is called a discriminator, a device that is set to disregard all pulses that are not in a certain amplitude range, hence blocking unexpected pulse signals that could otherwise disturb the final measurement. The now selected pulse will then travel to a *time to voltage converter* (TAC), a capacitor which creates and stores an analogue voltage signal proportional to the time until it is hit by a “stop” pulse. In other words the TAC will simply hold on to an increasing voltage until it is released by the stop signal pulse. The voltage is stored in a multichannel analyzer which consists of several counters, each corresponding to a certain voltage interval, e.g. counter 1 is activated at voltages between 0-1V while counter 2 is activated at 1-2V etc. The counters corresponding to frequently observed delay times/voltage accumulation will thus be the ones attributing the most photon counts unto the histogram and an accurate representation of the sample decay will be plotted continuously. The stop signal travels the same journey as the start signal, the main difference being that the emission signal can be transcribed from a different photon to pulse converter component, e.g. a photomultiplier (PMT) as shown in the schematic.

1.5.3 Atomic Force Microscopy (AFM)

In short, the AFM instrument is used to produce images of a surface via an oscillating needle that is tracked by a laser, Figure 30 presents a simple schematic showing the major components of an AFM instrument.

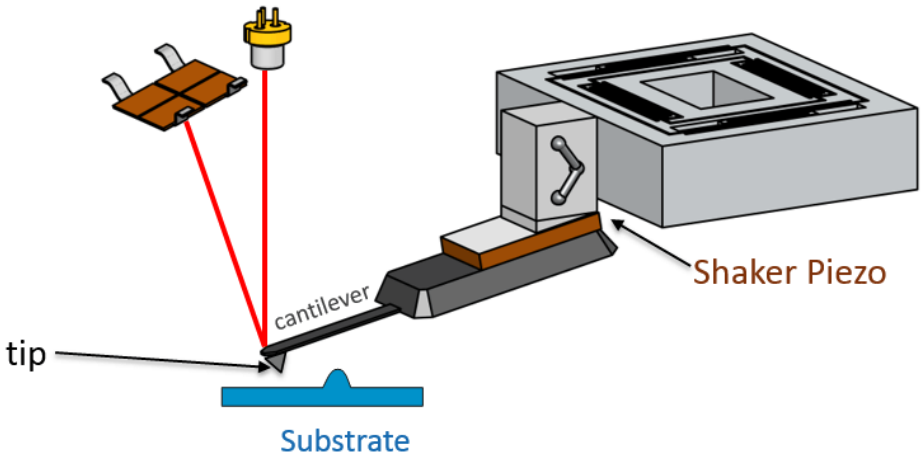

Figure 30 Simple schematic of an AFM setup [46].

The cantilever can simply be described as a bendable arm with an needle/tip attached at the end. This needle usually consists of a single silicon based crystal (typically 5-10 nm tip radius) and is used to hit the sample being investigated. When the cantilever oscillates up and down, a slight bending occurs when the tip makes contact with the sample. The bending of the cantilever causes the tracking laser to shift its deflected angle and this shift is what will get measured by a position sensitive photo-detector (PSPD). The information gathered from the different positions in which the deflected laser hits the PSPD will again be turned into image data via a computer. Imaging a surface via oscillation is called a tapping-mode measurement and for this type of experimentation a component called the shaker piezo is required to oscillate the needle at frequencies usually ranging from 100 Hz - 2 MHz [46].

To avoid both damaging the sample and provide reasonable measurements the cantilever must have a lower spring constant than that of two atoms in a solid (10 N/m order). If the cantilever spring constant were to be higher it will dent the sample and the resulting topographic measurement would be unrealistic. The tapping mode is in short based on a constant pressure between the needle tip and the sample being investigated while the cantilever bending provides the data [47].

2. Results and Discussion

2.1. Alkylation

The method of synthesizing the target compounds is a continuation of a previous master thesis. For more information regarding temperature, solvent, catalyst variables and their effects on the reactions discussed here please see reference [6]. General reactions for synthesizing IPQ and IDQ are given in Scheme 3.

Scheme 3 General reactions for synthetization of IPQ (above) and IDQ (below).

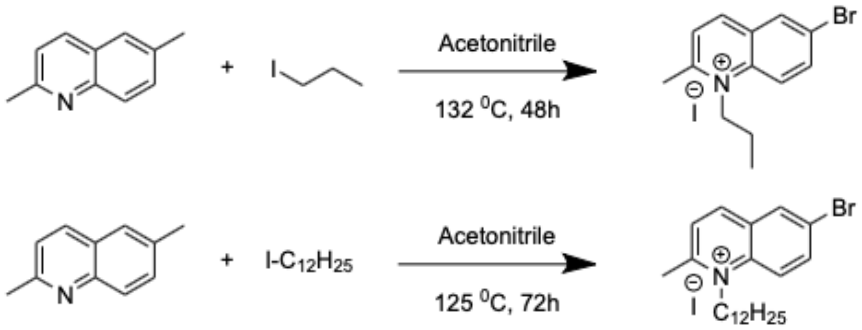

Alkylation of quinoline with iodododecane were tried with three different solvents, two polar aprotic and one non-polar. The solvents were chosen to see differences of reaction with regards to dielectric constant changes. Table 2 lists the reaction solvent and conditions used for the synthesis of IDQ.

Table 2 Reaction conditions for alkylation of quinoline with iodododecane.

Solvent:	Temperature	Reaction time	Dielectric constant	Yield (%)
$CHCl_3$	120 °C	72 h	4,8	No Reaction
EtOAc	120 °C	72 h	6,0	No reaction
Acetonitrile	120 °C	72 h	37,5	30,2

While a lower dielectric constant for the solvents would be expected to diminish the yield in an Sn2-reaction, it was still interesting to see the actual severity of the change in yield. Using EtOAc and chloroform, the first solvent which would have caused a precipitation of the product and the latter which exhibited the best solubility of the product, gave no signs of a successful reaction. These findings help to emphasize the importance of the zwitter-ionic intermediate that is formed in the rate determining step of an Sn2-reaction and can be viewed in Figure 31.

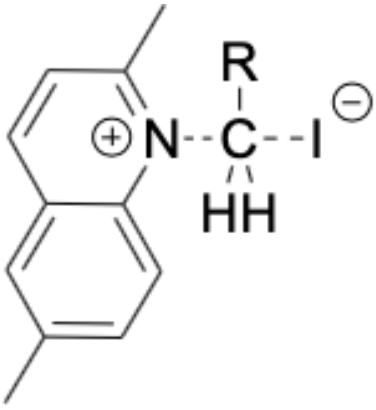

Figure 31 Zwitterionic quinoline intermediate in during alkylation.

One could argue that the increased stabilization of the amide due to conjugation might allow for less polar solvents to be used as its electrophilic character could be decreased, hence reducing the N^+ - I^- intermediate attraction. The results however show that, even for this quinoline alkylation, a polar aprotic solvent of high dielectric nature is necessary to stabilize the iodide leaving group for efficient departure. Though chloroform and EtOAc were inefficient in this study there have been reports of toluene giving good yields in similar compounds [48], conveying that ionic stabilization towards the nucleophile can be a successful approach with the help of aromatic pi-stacking solvents of low dielectric constant.

A lower yield of IDQ was acquired using acetonitrile and similar reaction conditions as were presented in reference [6]. The reason for this may be that the purification method was changed to filtrate washing with EtOAc instead of column chromatography which may point towards the compound being more soluble in this solvent in the presence of by-products in the reaction mixture. Though a more reasonable explanation could be that the reactions were done in a larger scale (1 gram) which gave lower yields for both this study and the referenced report. The same successful method could be used for alkylation of quinoline with iodopropane, which resulted in a higher final yield of 58% using acetonitrile as a solvent and a temperature of 120 ^{0}C. Due to larger solubility difficulties caused by the shorter alkyl chain, this reaction could easily be purified directly after the reaction via cooling of the mixture and filtration through a Büchner setup. Hence both alkylated versions could be acquired without using time consuming purification methods. A method to produce higher yields of IDQ in large scale reactions is something that could be further investigated.

Alkylation reactions of quinoline and 2-ethylhexyl bromide were also conducted to produce a compound which could provide additional information about branched alkyl length effects on aggregation behavior. The reactions were, however, unsuccessful due to heightened sterical hindrance of this alkyl chain and bromide being a poorer leaving group in an Sn2 reaction. Unfortunately, 2-ethylhexyl iodide was significantly more expensive as a reagent. The general

reaction and parameters can be visualized in Scheme 4, two reactions were tried with constant time and temperature but different solvents (acetonitrile and DMF).

Scheme 4 General reaction for alkylation of quinoline with 2-ethylhexyl bromide.

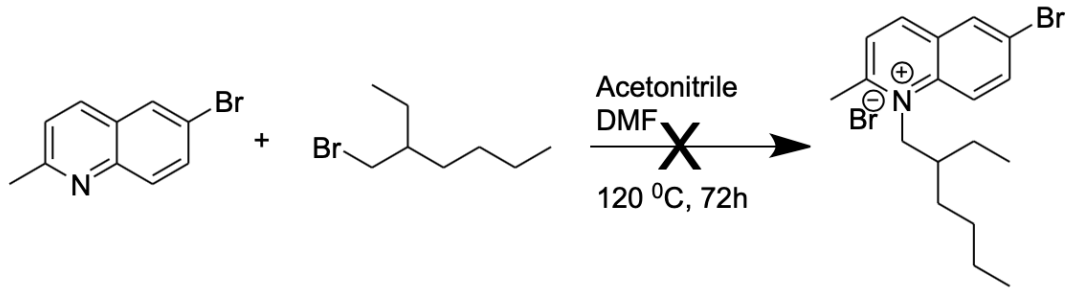

2.1.1. Assigned Proton shifts of IDQ and IPQ

As the dodecyl alkylated compounds had already been thoroughly characterized in the prior study [6], it was deemed unnecessary to repeat the full characterization once more for all dodecyl molecules, except for the target molecule IDQ-SQ-P, which have been fully characterized also here by HSQC, HMBC, COSY, H- and C-NMR.

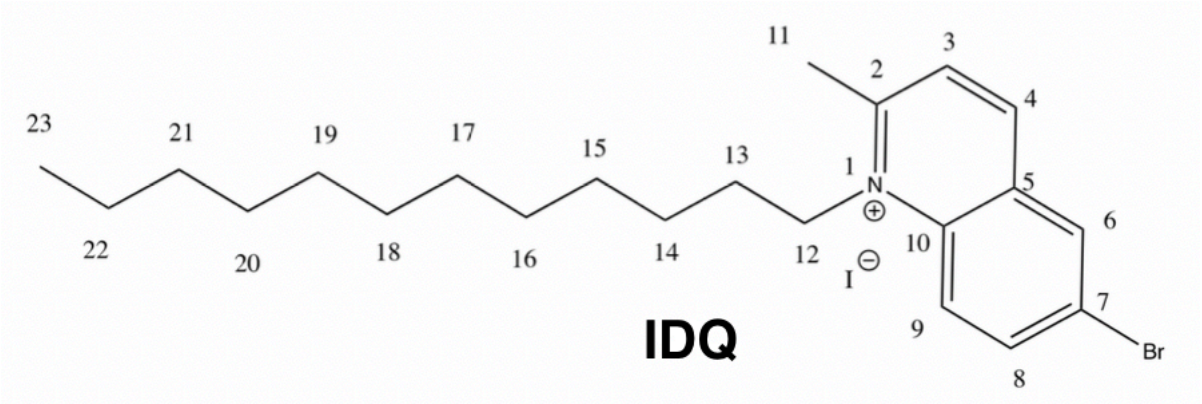

Shift H (ppm)	Position	Integral	Multiplicity
8,77	4	1	d
8,35	6	1	s
8,23	8+9	2	dd
8,05	3	1	d
5,06	12	2	t
3,32	11	3	s
1,98	13	2	p
1,62	14	2	p
1,42	15	2	p
1,26	16-22	14	m
0,88	23	3	t

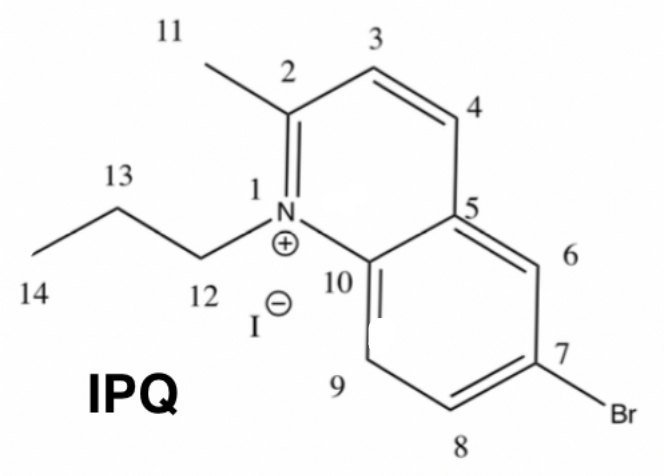

Shift H (ppm)	Position	Integral	Multiplicity
8,74	4	1	d
8,35	6	1	s
8,33	8	1	dd
8,23	9	1	dd
8,03	3	1	d
5,10	12	2	t
3,32	11	3	s
2,10	13	2	p
1,27	14	3	t

2.2. Disubstitution

Disubstitution of squaric acid with two equivalents of alkylated quinoline was performed using both toluene and benzene in an azeotropic distillation medium with 1-BuOH (50 V%) as the reactive co-solvent. Table 3 shows the reaction parameters for IDQ-SQ and IPQ-SQ in both solvent mixtures, while Scheme 5 presents the general reaction path for IPQ-SQ.

Scheme 5 General reaction for synthetization of IPQ-SQ

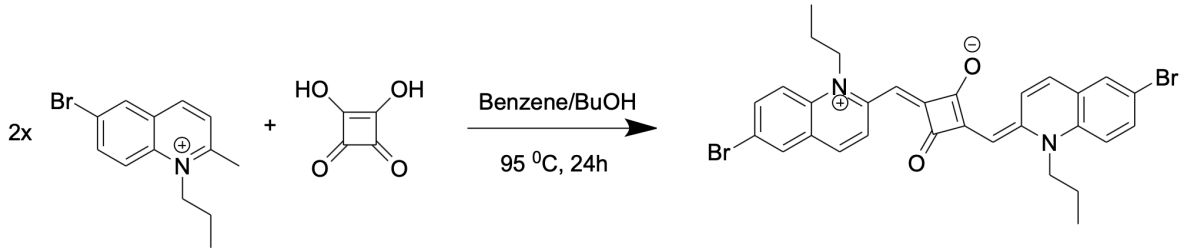

Table 3 Reaction conditions for disubstitution of IDQ and IPQ, azeotropic boiling points obtained from [49, 50].

Solvent Mixture	Temperature	Reaction Time	Solvent/H_2O azeotropic b.p	Yield: IDQ-SQ	Yield: IPQ-SQ
Toluene/BuOH	135 ^{0}C	24 h	84,1 ^{0}C	38%	58%
Benzene/BuOH	95 ^{0}C	20 h	69,3 ^{0}C	96%	77%

A considerable increase of reaction yield was acquired using benzene instead of toluene as the azeotropic distillation medium. While the electron donating methyl-group of toluene might cause some impairment towards quinoline stabilization compared to benzene, the increased yield is likely an effect stemming from the lower reaction temperature which the benzene-water azeotrope allowed while still retaining efficient water transfer through the dean-stark column. These results might be an effect from the reaction mixture being too sensitive at higher temperatures, thus making polymerization, unwanted intra-molecular reactions or degradation possible. Though investigating the byproducts formed in these reactions at 135 ^{0}C is considered beyond the scope of this study.

An overall lower yield was obtained when the same reaction conditions were used to produce the propane alkylated version of the compounds. This result is mainly attributed to the limited solubility of IPQ and IPQ-SQ in most solvents including these, hence the reaction rate could

have been lowered via insufficient concentration. It should be mentioned that a downside of using benzene lies in its highly toxic nature and that proper safety equipment must be used during handling [51].

When characterization of IPQ-SQ via ^{13}C-NMR was attempted, problems arose due to a limited solubility of the compound i.e. only dilute concentrations could be made which was insufficient to provide interpretable ^{13}C-NMR spectra. Interestingly the concentrated solutions made in NMR-tubes seemed well solubilized initially, however after a minute the whole solution was full of thick precipitate (see Figure 32). This may suggest that the higher degree of aggregation for the propane alkylated squaraine, discussed in the AFM section, may exhibit a critical role in the solubility issues of IPQ-SQ, which is a prominent discovery throughout this study.

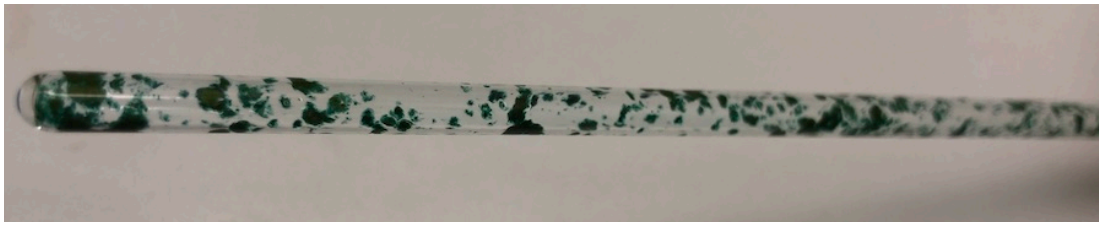

Figure 32 IPQ-SQ in $CDCl_3$ after one minute, A small amount of IPQ-SQ was used before the addition of the deuterated solvent

2.2.1 Assigned Proton shifts of IDQ-SQ and IPQ-SQ

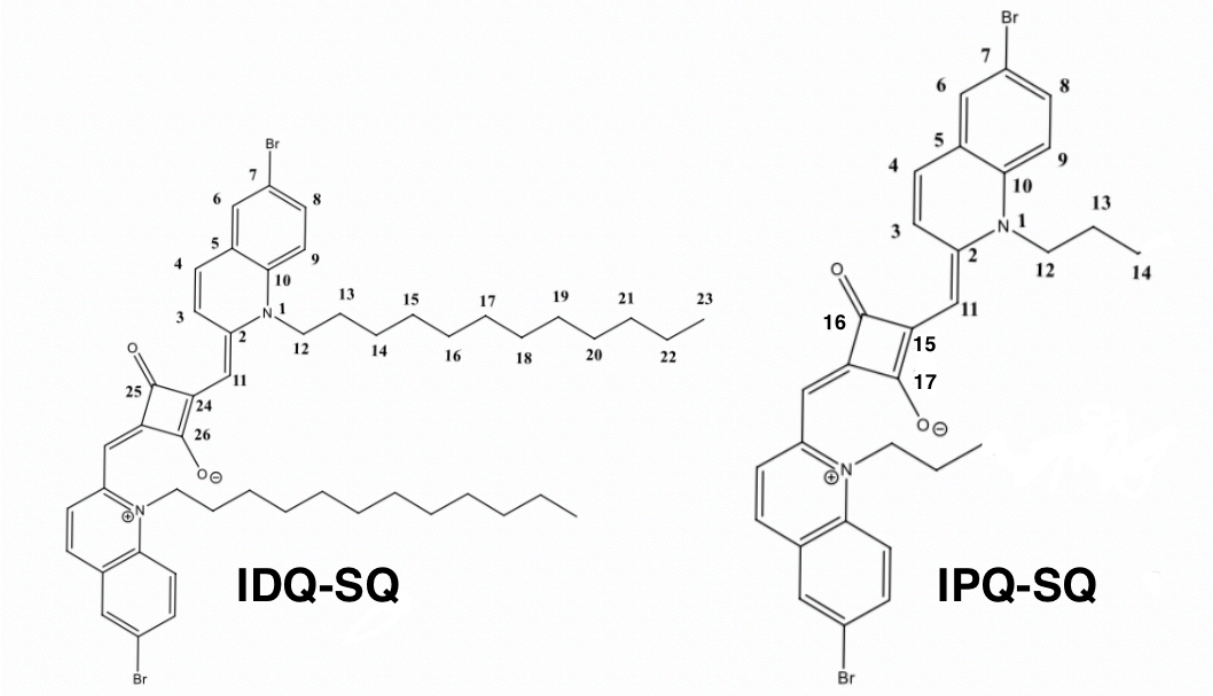

Shift H (ppm)	Position	Integral	Multiplicity
9,37	4	1	d
7,62	8	1	dd
7,59	9	1	dd
7,33	3	1	d
7,19	6	1	d
5,79	11	1	s
4,13	12	2	t
1,85	13	2	m
1,54	14	2	p
1,44	15	2	p
1,30	16-22	14	m
0,90	23	3	t

Shift H (ppm)	Position	Integral	Multiplicity
9,38	4	1	d
7,62	8	1	dd
7,59	9	1	dd
7,34	3	1	d
7,18	6	1	d
5,79	11	1	s
4,12	12	2	t
1,92	13	2	m
1,18	14	3	t

2.3 Cross-coupling with Pyrene.

Cross coupling of IDQ- and IPQ-SQ with pyrene was done using conditions similar to those used in reference [6] and provided yields in good accordance with respect to the dodecyl alkylated compound. The IPQ-SQ-P did however produce a significantly lower yield which could be attributed to solubility issues. Two reactions were performed with parameters given in Table 4. $Pd(OAc)_2$ combined with SPhos were used as catalysts for both reactions. Scheme 6 presents the general reaction path for synthetizing IDQ-SQ-P.

Scheme 6 General reaction path for synthetizing IDQ-SQ-P

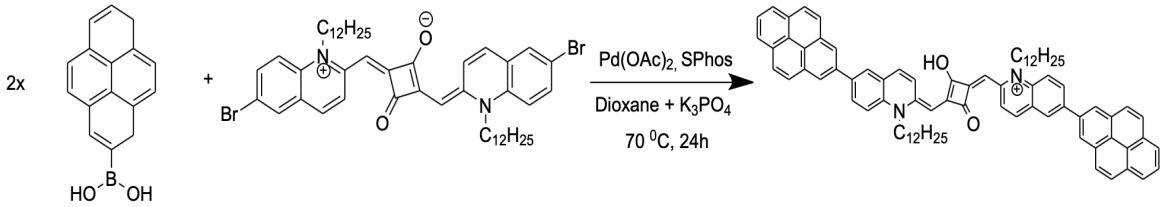

Table 4 Reaction temperature, time and yields of Suzuki cross-coupling of IDQ-SQ and IPQ-SQ with pyrene-1-boronic acid.

Synthesized comp.	Temperature	Reaction Time	Solvent	Base	Yield
IDQ-SQ-P	70 ^{0}C	24 h	Dioxane	K_3PO_4	56%
IPQ-SQ-P	80 ^{0}C	24 h	Dioxane	K_3PO_4	28%

The IPQ-SQ-P compound seemed to have an increased solubility in DMF which was discovered later during this study, therefore an increased yield might have been obtained if this solvent was used instead. Other parameters which could have caused a better yield would be changing the catalyst and/or base as well as temperature. As IPQ-SQ-P, to my knowledge, can be considered the novel compound synthesized in this study, it was rather unfortunate for it to exhibit similar solubility issues as with its precursor molecule. Yet again thick precipitate was formed after a small amount of time in the NMR-tubes and only diluted concentrations could be made without precipitation distorting the spectra. Even for the H-NMR results obtained for this compound, approximately 100 scans were necessary to provide interpretable data.

C-NMR spectra, which are necessary if the compound has yet to be characterized, were therefore impossible to obtain using the common deuterated solvents available. To counteract this, special coaxial tubes were ordered so that DMA or unprotonated solvents could be used while $CDCl_3$ could provide the locking signal without interfering with the compound.

Unfortunately the delivery was not made in time, meaning that H-NMR spectra and the vast photophysical similarities between IPQ- and IDQ-SQ-P shown throughout this section were considered sufficient to be certain that this is still the correct compound.

As with previously referenced study, neither the IPQ- or IDQ-SQ-P could be found via mass-spectroscopy using a synapt G2-S Q-TOF instrument. Due to their zwitterionic structure, fast atom bombardment (FAB) may be a more suited analytical approach [52].

2.3.1 Assigned Proton/carbon shifts of IDQ-SQ-P and IPQ-SQ-P

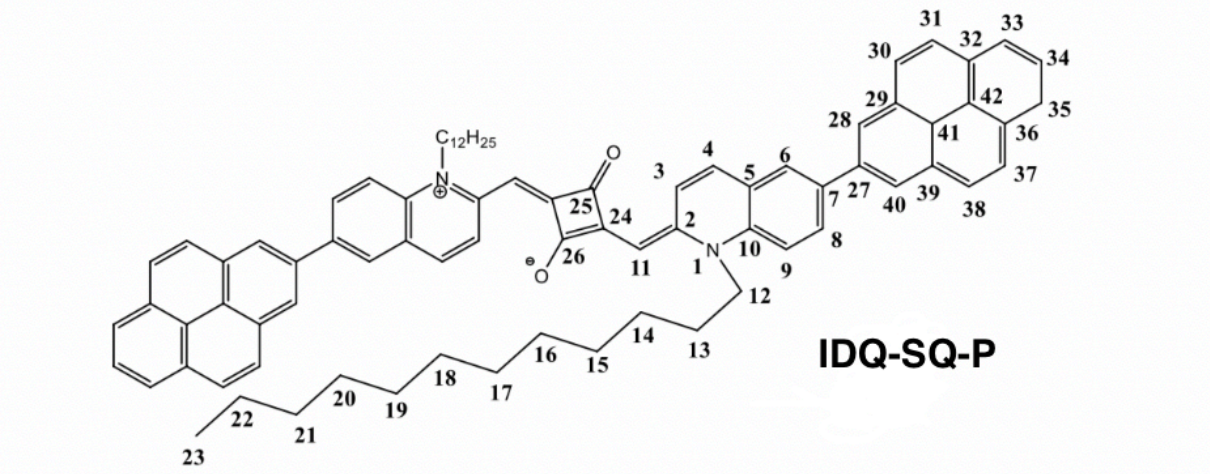

Shift C (ppm)	Position
14,15	23
22,72	17
26,77	13
26,98	14
29,38	19
29,44	15
29,62	21
29,67	20
29,70	22
29,98	16
31,94	18
48,20	12
93,01	11
114,33	9
124,51	30 + 38
124,85	33 + 35
125,03	41
125,40	5
126,20	37 + 31
127,28	34
127,38	4 + 24
127,56	40 + 28

Shift H (ppm)	Position	Integral	Multiplicity
9,47	4	1	d
8,26.	22, 28	2	t
8,21	21, 29	2	t
8,14	19, 31	2	s
8,06	24, 25, 26	3	m
7,82	8	1	d
7,78	6	1	s
7,56	3	1	dd
7,50	9	1	dd
5,88	11	1	s
4,27	12	2	t
1,98	13	2	m
1,62	14	2	m
1,49	15	2	m
1,31	16-22	14	m
0,89	23	3	t

128,50	39
130,09	6
130,20	42
131,49	29
131,67	32 + 36
132,64	3
133,48	8
135,71	27
136,72	10
138,88	7
150,05	2
150,09	25 + 26

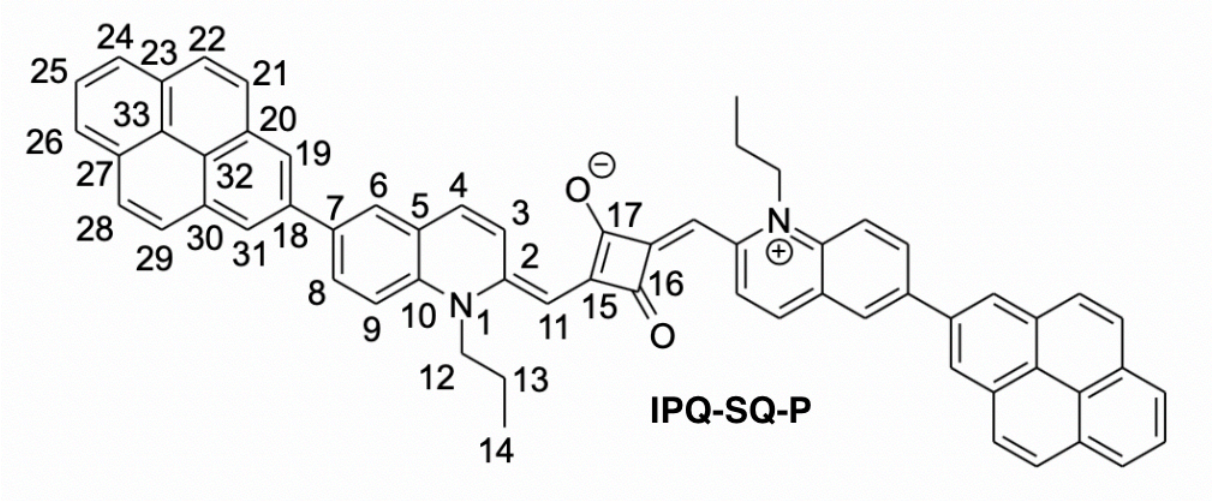

Shift H (ppm)	Position	Integral	Multiplicity
9,48	4	1	d
8,27	22, 28	2	t
8,21	21, 29	2	t
8,15	19, 31	2	s
8,07	24, 25, 26	3	m
7,84	8	1	d
7,79	6	1	s
7,58	3	1	dd
7,54	9	1	dd
5,90	11	1	s
4,29	12	2	t
2,05	13	2	m
1,26	14	3	m

As a consequence from the high number of scans required to produce the H-NMR spectra for IPQ-SQ-P, solvent and impurity peaks became quite prominent. This is well visualized due to the high grease peaks which are situated at 0,86 and 1,25 ppm as well as a high acetone peak at 2,19 ppm which probably stem from previous NMR-tube washings.

2.4 Absorption and Solvent-effects

When presenting the photophysical data of the synthesized compounds, the absorption peaks have been abbreviated H-Peak for the aggregate maxima blue-shifted from the monomer peak and J-Peak for the red shifted aggregate maxima. Any additional peaks are named after their respective wavelength. To save space in the following sections, emission, absorption and/or excitation scans are not always presented for both alkylated versions of the compound as they show next to identical photophysical properties. It is expected that changes in alkylation of the compound should not (and indeed did not) yield any differences in absorption maxima. However they are expected to play a major role in the aggregation phenomena taking place. The purpose of the varying alkyl chains is to evaluate these differences. Therefore, unless otherwise is stated or visualized, the spectroscopic graphs presented for one compound gives the same graph for the other alkylated version.

The brominated squaraines IDQ- and IPQ-SQ exhibited drastic differences in solubility properties, as the dodecyl alkylated version revealed good solubility in chloroform and other solvents while the shortened alkyl chain version had limited solubility in all the solvents investigated.

Table 5 presents the solubilities ranked from poor to good for both compounds where poor signifies that the compound was noticeably insoluble, but still able to provide spectroscopic data. Medium signifies that the compound solubilizes, but with a significant amount of precipitation, while good denotes complete solubility. Experiments were conducted using 10^{-3} M solutions.

Table 5 Solubilities of IDQ-SQ and IPQ-SQ

Solvent	IDQ-SQ	IPQ-SQ
CHCl3	Good	Medium
NMP	Good	Medium
MeOH	Insoluble	Medium
THF	Good	Poor
Acetonitril	Poor	Poor

Out of all the solvents investigated only chloroform was able to provide absorption spectra containing a monomer dominant peak when concentration did not exceed 10^{-5} M while other solvents revealed absorption spectra distinctive to their fully aggregated species regardless of dilution extent. The concentration of 10^{-5} M was chosen because it was the minimum concentration where all the optical measurements could be conducted uniformly. More dilute concentrations would cause weak signals both in absorption and emission measurements. Higher concentrations would yield dye aggregation. A concentration of 10^{-5} M provides confidence that phenomena observed would be attributed to the forces promoting the aggregation and not simply because of proximity of the dye molecules in the solution.

Despite the solubility differences, the absorption properties were not affected to any detectable degree by the length of the alkyl chain neither in chloroform or the aggregate inducing solvents, signifying that sterical hindrance from these moieties are not affecting the preferred aggregated structure. Figure 33 presents the absorption spectra of IDQ-SQ in chloroform with aggregation measured over time.

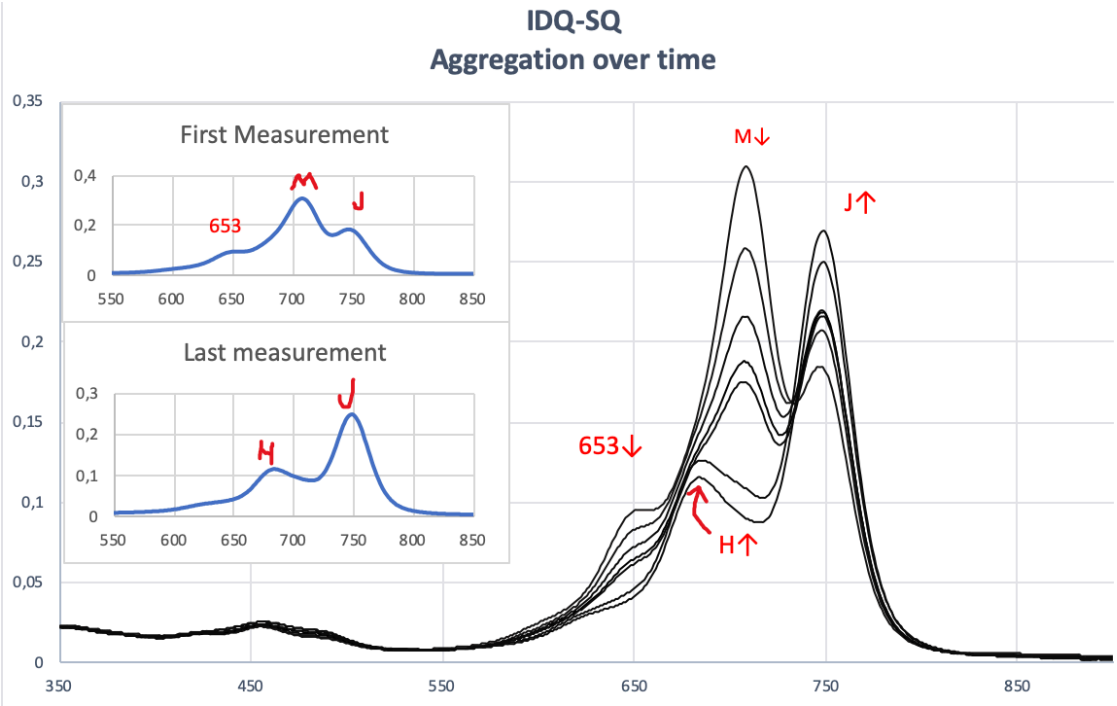

Figure 33 IDQ-SQ aggregation over time J = 749nm, M = 708nm, H = 689nm. All measurements were done in the same capped cuvette over the span of two hours, cuvette was also shaken vigorously between every measurement to ensure uniform distribution.

As shown in the absorption spectra, the IDQ-SQ dye, when not aggregated, exhibits 3 distinct peaks with maxima at 653 nm, the main absorption peak at 708 nm and a smaller signal at 748 nm. Due to extended conjugation and hybridization of the energy levels of the two components (quinoline and squaraine) the absorption characteristics provide additional evidence that the formation of the dye was successful since none of the two components are expected to show optical signals in this region of the visible spectrum [53, 54]. The 653 nm peak can be attributed to the interaction of the squaraine with either one of the quinoline moieties and the subsequent delocalization of the formed exciton, while the 708 nm peak ("monomer" peak) is attributed to the acceptor-donor-acceptor (quinoline-squaraine-quinoline) trimer. The 749 nm peak is attributed to the J-aggregate which is expected to be red-shifted. It is worth noting that the synthesized dye possesses optical characteristics in accordance with a similar series of quinoline-squaraine dyes reported in the literature [55], and significant better optical characteristics than a series of semi-squaraine dyes (mono-substituted squaraines) where the absorption maxima lies in the region of ~500-550 nm [56]. Once concentration is increased or after the solution is left to aggregate, the UV/Vis spectra change and becomes dominated by two components. A peak at 689 nm, attributed to the formation of H-aggregates and the J-aggregate peak at 749 nm which increases in intensity and becomes the main absorption peak. The propane alkylated squaraine exhibited the same spectra as IDQ-SQ with the exception of aggregating slightly quicker, which can be due to the shorter alkyl chain and poorer solubility.

An interesting observation was both molecules' ability to aggregate in a fixed volume, and even more so remain in the aggregated state after vigorous shaking. The aggregation must therefore be based on relatively strong intermolecular forces as it is irreversible unless the same solution is diluted by tenfold, after which the aggregation will again reinitiate. Additionally, should the same experiment be performed without the in-between cuvette shaking, the monomers would aggregate to such a degree that concentration gradients form outside the light path of the UV/vis spectrophotometer i.e. absorption intensity drops by up to 80%. This is hinting towards higher order aggregation or aggregate bulks consisting of weaker inter-aggregate coherence.

When performing absorption measurements of IDQ- and IPQ-SQ in toluene, NMP, acetonitrile and methanol significant absorption maxima shifts did occur and are listed in Table 6.

Table 6 Absorption peaks of IDQ-SQ and IPQ-SQ in different solvents, R: indicates a red shift, B: indicates a blue shift.

	IPQ-SQ		IDQ-SQ	
Solvent:	H-peak (nm)	J-peak (nm)	H-peak (nm)	J-peak (nm)
$CHCl_3$	681 Reference	747 Reference	681	747
Toluene	695 R: 14nm	765 R: 18nm	695	765
NMP	689 R: 8nm	757 R: 10nm	689	757
Acetonitrile	677 B: 4nm	741 B: 6nm	677	741
MeOH	661 B: 20nm	722 B: 25nm	INSOLUBLE	INSOLUBLE

Except for the equal absorption properties of both compounds mentioned earlier, there were found two interesting trends during the solvent study. The first being that toluene and NMP exhibited a red absorption shift of both H- and J-aggregate peaks while acetonitrile and MeOH revealed the opposite effect in the form of a blue shift. When investigating the optical properties of squaraine dyes in solvent studies, there is one moiety that has a particular interest, namely the electron deficient squaraine core [3, 57]. The carbonyl, carbonyl-anion groups of this moiety would be prone to H-bonding with the protic MeOH solvent and does in this experiment also exhibit the largest change of shift out of all solvents investigated. According to exciton theory a blue shifted absorption may be explained by a destabilization of the structure and is a reasonable assumption in this case as hydrogen-carbonyl interactions could inhibit resonance stabilization of the squaraine core. Though commonly referred to as an aprotic solvent, the methyl group of acetonitrile has been found to exhibit hydrogen donating properties in regards

to both self-association and in anionic environments [58, 59]. Therefore the small blue shift present in this solvent may be explained by the same assessment as MeOH, the difference being substantially weaker interactions.

The other extreme case where toluene induces a large red shift would also be best explained in accordance to the squaraine core, though by indirect interactions via the quinoline moieties. It can be hypothesized that the aromatic toluene, with its pi-stacking capabilities and high preference towards parallel association [60], is likely to interact with the electron rich quinoline moiety. And by this association an increase of electron donating capabilities from the quinoline moieties to the squaraine core could be a plausible explanation, with the assumption that a red shift is due to stabilization. NMP, however, showing a lower red shift is more difficult to explain in the context of exciton theory and may be due to carbonyl - carbonyl repulsion in regard to the squaraine core and/or NMP´s zwitterionic resonance structure interacting with the ammonium ion of the quinoline moiety.

The second trend which can be seen is that the H-aggregate peak does not shift at the same magnitude as the J-peak and is more prone to show a difference with the two extreme cases of toluene and MeOH. From Table 6 it can be seen that the J- and H-absorption maxima are 4 nm further away from to each other in toluene and 5 nm closer in methanol in respect to the chloroform absorption peaks. If parallel and linear stacking are assumed for the H- and J-moiety respectively it would make sense that the more unstable parallel aggregation would be less prone to external changes due to packing induced sterical hindrance around the squaraine core. In the same sense it could be argued that a linear aggregation exposes the core to a higher degree, making it more susceptible to solvent changes.

After cross-coupling the two compounds with pyrene, an immediate red absorption shift (10nm) can be noticed, a phenomenon attributed to increased conjugation of the system. Also, the appearance of peaks at 345 nm indicates that the pyrene moieties are present in the molecule [61]. Both the dodecyl and propane alkylated compounds with pyrene revealed no photophysical differences in chloroform, and similar to their precursors, they exhibited the same tendency to aggregate over time. Figure 34 shows the absorption spectra of IPQ-SQ-P in chloroform before and after aggregation, while Table 7 presents the absorption data in aggregate inducing solvents. It is worth noting that the pyrene moiety, that has a profound

ability for pi-pi stacking, does not noticeably show any signs of promoting the aggregation of chromophores.

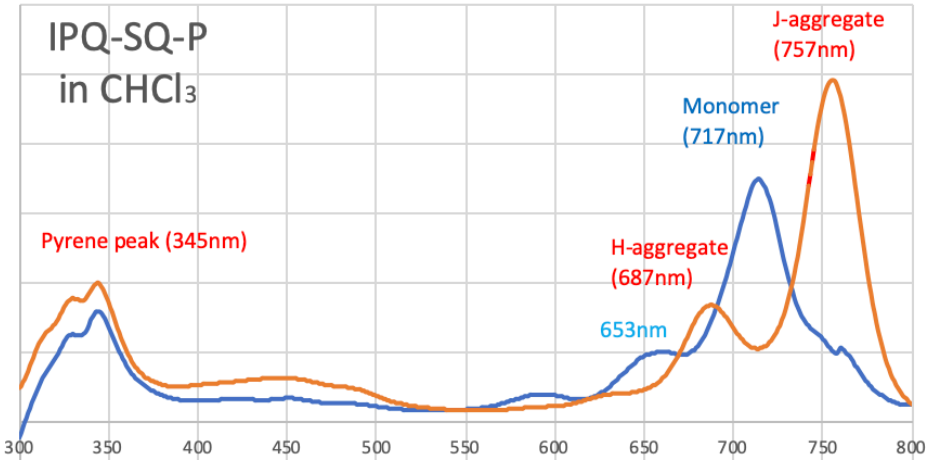

Figure 34 Absorption spectra of IPQ-SQ-P in chloroform before and after aggregation

Table 7 Absorption data of IPQ- and IDQ-SQ-P in aggregate inducing solvents.

	IPQ-SQ-P		IDQ-SQ-P	
Solvent:	H-Peak (nm)	J-Peak (nm)	H-Peak (nm)	J-Peak (nm)
$CHCl_3$	687 (reference)	755 (reference)	687 (reference)	755 (reference)
Toluene	703 R: 16nm	774 R: 19nm	703 R: 16nm	774 R: 19nm
NMP	695 R: 8nm	764 R: 9nm	697 R: 10nm	767 R: 12nm
Acetonitrile	679 B: 8nm	743 B: 12nm	682 B: 5nm	745 B: 10nm
MeOH	661 B: 26nm	722 B: 33nm	INSOLUBLE	INSOLUBLE

Though the precursor compounds were equal in photophysical absorption character, the pyrene coupled versions exhibited small differences (2-3 nm) when solvents were changed. These differences are however, too small and inconsistent to extract any good indication of the alkyl chain role. It should also be noted that the monomer moiety could only be studied when the compounds were solved in chloroform, just like the precursor molecules.

The most interesting observation lies within the extreme shifts induced by MeOH and toluene. In a comparison of IPQ-SQ with and without pyrene in methanol, (Figure 35), there are no clear absorption differences except for the pyrene peak located at 345nm. This effectively means that hydrogen bonding interacts with the compound to such a degree that the additional pyrene

conjugation becomes negligible in a photophysical point of view. It should also be mentioned that the dodecyl alkylated compound can be blue-shifted to 727nm (J-peak) with a MeOH/$CHCl_3$ composition of 60% indicating that this too could reach equal spectroscopic properties with its precursor in pure methanol.

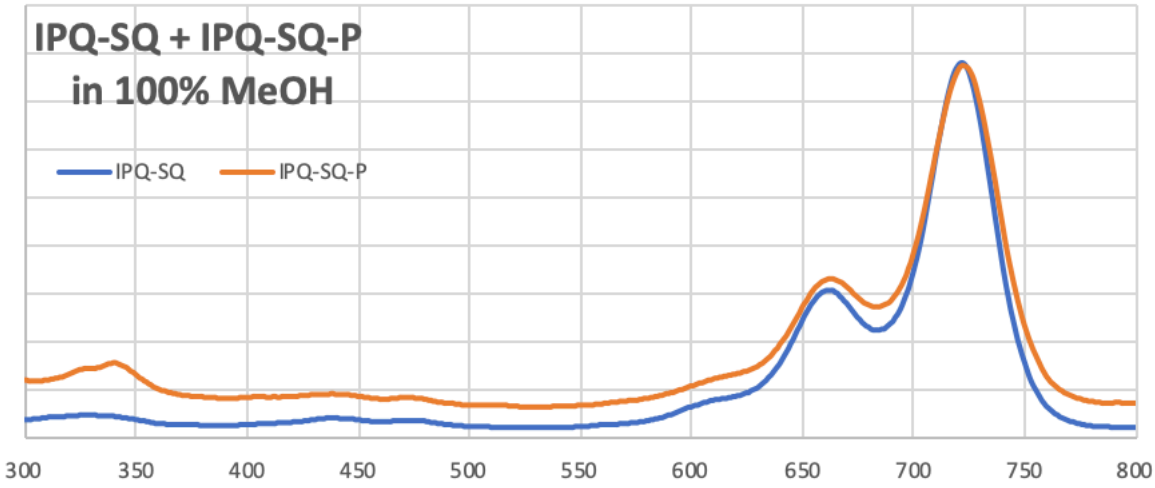

Figure 35 Absorption spectra of both IPQ-SQ and IPQ-SQ-P in methanol.

2.5 Emission Studies

Emission studies were performed on the synthesized compounds to attribute emission maximas to each absorption peak found in chloroform. The measurements were performed sequentially to the absorption measurements using the same sample parameters. The figures presented in this section tend to show the emission spectra from excitation at 635nm to enhance correspondence with the time-resolved measurements (done with a 635nm pulsed laser) presented later. Excitation at 635 nm was also preferred to observe possible emissions of the other components on the absorption spectrum of the dye. Excitation at the absorption maxima of the dyes, which is usually the protocol for emission measurements, yielded no differences in emission wavelength. Figure 36 shows the emission properties of IPQ-SQ and IDQ-SQ solved in chloroform before and after aggregation.

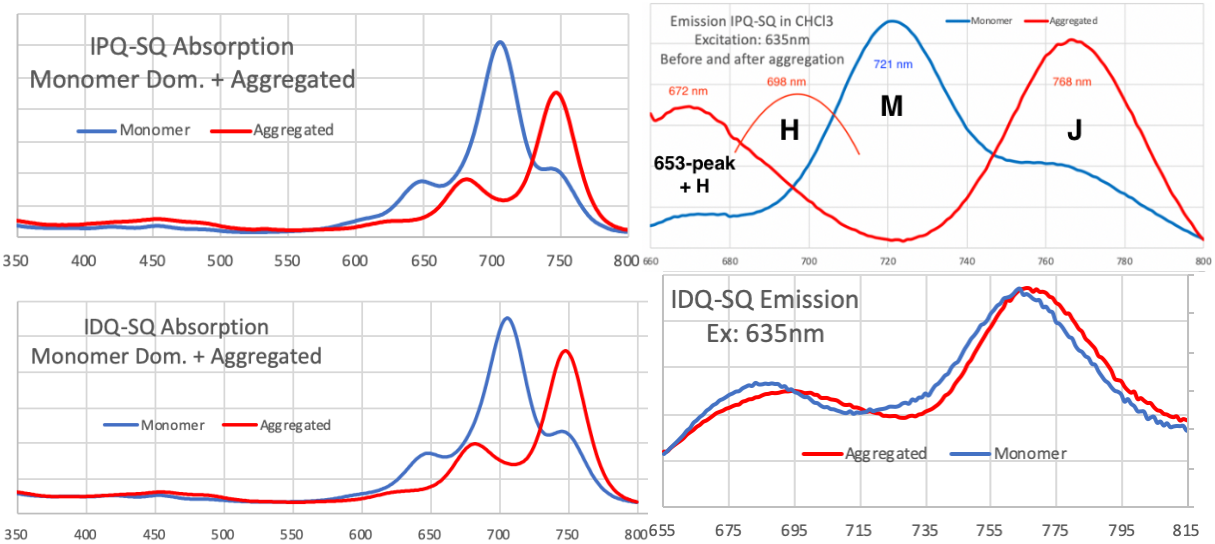

Figure 36 Adsorption and emission spectra of IDQ- and IPQ-SQ before and after aggregation in chloroform.

H- and J-aggregate emission peak maxima for both compounds in chloroform were found at 698nm and 768nm respectively. When using an excitation wavelength of 635nm the smaller peak at 653nm is also showing emissions from 672 – 694nm, shifting bathochromically with increasing aggregation. Excitation beyond the 653nm absorption peak gives the 698nm emission maxima attributed to the H-aggregate, hence the higher energy emission peaks shown the figure can be regarded as shared maxima between the H- and 652nm moieties.

An unexpected observation was that the IDQ-SQ monomer exhibited no fluorescence attributed to the monomer emission, but only emissions attributed to the aggregates. The propane alkylated monomer, on the other hand revealed a clear emission maxima (721nm). It is likely that the longer alkyl chain enables a higher quantity of vibrational energy states within the molecule, causing it to become non-fluorescent, or at least quenching its emission properties to an unattributable degree. Though the monomer does not seem to exhibit fluorescence the aggregates still emit strongly, a phenomenon commonly named aggregate induced emission (AIE). This emphasizes that the aggregate structure significantly restricts intramolecular rotation of the alkyl chain [62].

During the emission tests in chloroform the J-aggregate moiety continuously exhibited large emissions regardless of excitation points used, hinting that this is a moiety which is particularly susceptible to charge-/energy-transfer from higher energy moieties. Therefore emission tests were performed in the aggregate inducing solvents, which can be assumed to fully aggregate the compounds due to the fact that monomers cannot be isolated in them. It should be noted however, that there were no signs of charge/energy-transfer from the monomer moieties

towards the J-aggregate were observed during the sequential excitation tests. Figure 37 shows the emission from various excitation points of IDQ-SQ solvated in NMP while Figure 38 shows an excitation scan of IPQ-SQ in acetonitrile.

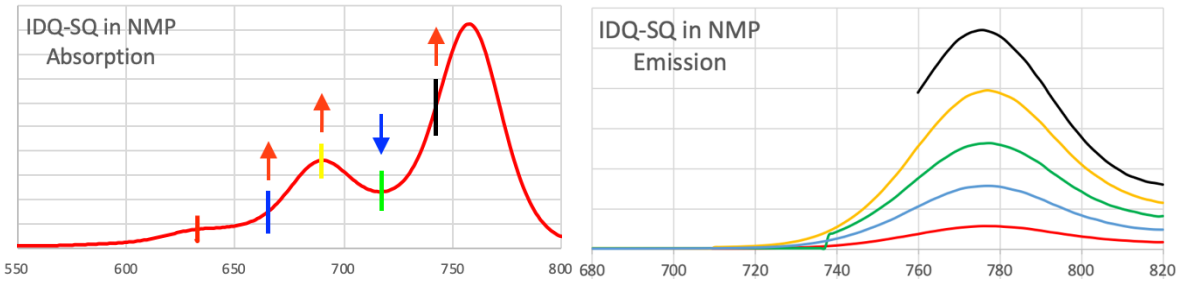

Figure 37 Excitation wavelengths and corresponding emissions, arrows indicate either an increase (up) or a decrease of emission intensity in respect to the prior excitation point (left).

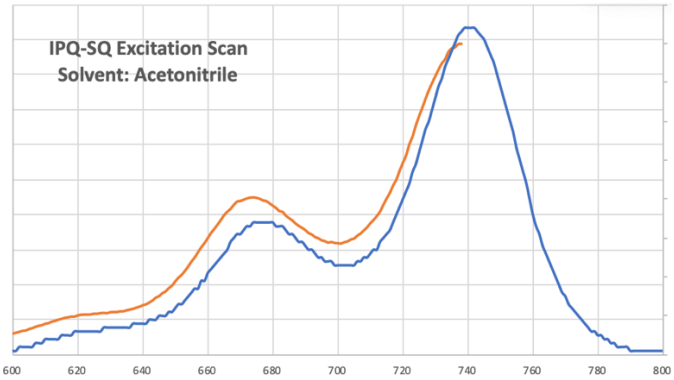

Figure 38 Excitation scan (orange) and corresponding absorption spectrum (blue) emission measured at J-emission maxima (763nm)

The fully aggregated molecule conformations revealed that all moieties tried excited gave a single J-emission peak, meaning that dominant charge transfer unto the J-moiety had been achieved. This behavior was consistent with all the emission tests done in aggregate inducing solvents, emphasizing that the aggregation investigated in chloroform was of incomplete character. Therefore chloroform can be used as a indicative method to study the separate aggregated building blocks prior to the complete aggregate structure. The excitation scans were also in agreement with complete energy/charge transfer as the resulting excitation spectra mimicked the absorption spectra. Since the compounds in chloroform (after aggregation) exhibited emission maxima for at least two moieties, an assumption that the complete aggregate structure is at, or more likely, above the tetramer order could be justified.

When the pyrene-coupled compounds IDQ-SQ-P and IPQ-SQ-P were studied in chloroform, all compounds exhibited clear monomer emission peaks. This shows that the attached pyrene groups have caused vibrational relaxation energy levels to be less accessible in the dodecyl

alkylated compound. The effect is likely caused by the increased conjugation of the system, but might also be partly due to sterical constraints in the alkyl chain mobility. Figure 39 presents the absorption and corresponding monomer emission of IDQ-SQ-P while Figure 41 shows the absorption and an excitation scan of IPQ-SQ-P containing both monomer and aggregate moieties. Both alkylated versions had a monomer emission maxima at 729 nm while H- and J-emission were found at 709 and 774 nm respectively.

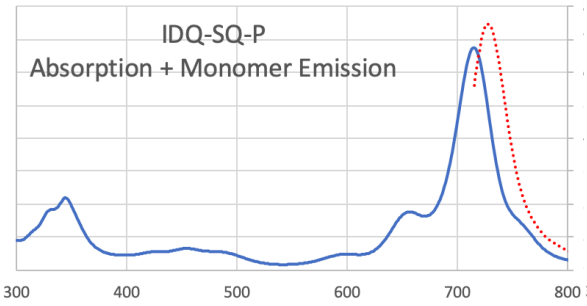

Figure 39 Absorption and monomer emission (red) IDQ-SQ-P in chloroform

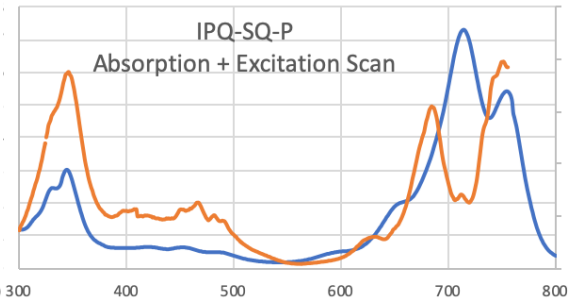

Figure 40 Absorption (blue) and Excitation scan of Aggregate of emission (orange) in IPQ-SQ-P chloroform solution.

An excitation scan measured at the J-emission maxima shows, that the monomer moiety exhibits no signs of charge/energy – transfer towards the aggregate just like the precursor molecules. It also reveals that the H-moiety is very much present, even though it is masked by the monomer absorption in diluted chloroform solutions. From an excitation scan measured at the monomer emission, an "exact" replica of the absorption spectra in Figure 39 is obtained, hence the 657nm peak is an absorption phenomena belonging solely to the monomer moiety as was also indicated by its disappearance after aggregation. Interestingly the absorption areas from 345-550 nm became more pronounced after the pyrene addition, hinting that these areas can be a result of excimer formation. To further expand upon this an emission scan was performed by exciting the pyrene moiety at 340 nm, which is presented in Figure 41.

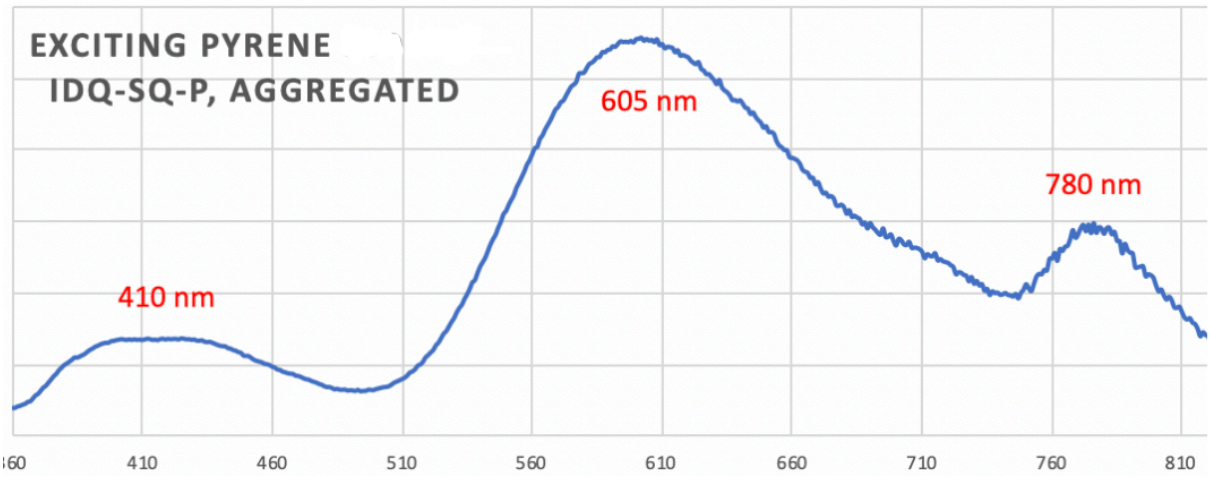

Figure 41 Emission scan of IDQ-SQ-P obtained by exciting the pyrene absorption maxima at 345 nm.

This experiment revealed that broad emission intensities with high stoke shifts are prominent over the whole emission range from 360-810 nm, indicating that pyrene-pyrene excimers have formed [63, 64]. Literature states that pyrene pi-stacked lattices exhibits a high exciton-phonon coupling constant [65], effectively meaning that these types of interactions may work as small “electron trapping” sites. Should this be the case, then highly irregular emissions like those presented here would be expected. However, to confirm the nature of these results, TCSPC measurements and kinetic scans would need to be performed at the various emissions and would require a pulsed laser capable of exciting the 300 - 350 nm range, which was not available.

Table 8 presents the emission maxima and Stokes shifts obtained from PL- measurements in aggregate inducing solvents for both pyrene coupled compounds and precursors.

From these data it can be seen that the highest Stokes shifts are present in NMP and acetonitrile, hence intramolecular mobility would be less restricted in these solvents as opposed to toluene and MeOH. An expected observation since these solvents were chosen because they should interact less with the compounds than MeOH and toluene. Interestingly enough, the only case where the pyrene-coupled compounds show a significantly different Stokes shifts with regards to its precursor was by using NMP as the solvent. It was expected to see an overall change (decrease or increase) in Stokes shifts after the addition of pyrene due to aggregation changes, this doesn´t seem to be the case however. Why NMP would show large differences when the pyrene moieties are present is unknown, but may indicate that pyrene-NMP interactions do occur to a higher degree than expected or that it facilitates a different aggregate structure.

Table 8 Emission peaks for IDQ-, IPQ-SQ and IDQ-, IPQ-SQ-P with corresponding Stokes shifts calculated for the J- absorption maxima.

Solvent	IDQ-SQ	IPQ-SQ	IDQ-SQ-P	IPQ-SQ-P
Toluene	780 (15nm)	780 (15nm)	790 (16nm)	790 (16nm)
NMP	776 (19nm)	776 (19nm)	793 (26nm)	793 (29nm)
Acetonitrile	762 (21nm)	760 (19nm)	765 (19nm)	763 (21nm)
MeOH	INSOLUBLE	739 (17nm)	INSOLUBLE	738 (16nm)

2.6 Time-Resolved Measurements

The time-resolved measurements were done using the TCSPC method with a 635nm nanosecond pulsed laser. All data have been provided using the same experimental conditions with the exception of measuring the instrument respond function (IRF) which required adjustments of the laser slit to reach acceptable photon count rates. The parameters set for the experiments are listed as followed.

- Emission detector slit width: 25 nm
- Laser slit width: widest setting for samples and adjusted for IRF.
- Measuring range: 50 nm.
- Number of channels: 2048
- Measurements stopped at 10,000 photon peak count
- Laser intensity: 2 MHz

TCSPC was performed on IDQ- and IPQ-SQ solved in chloroform. One series of measurements was performed while the solution contained some monomer and some aggregates while the other was performed post “full” aggregation. The acquired data from IPQ-SQ can be viewed in Table 9 and the decay histograms obtained for J- and H- emissions from IPQ-SQ in chloroform are presented in Figure 42. While performing the time resolved spectroscopy very low stop rates or emission photon counts were observed for all the molecules investigated, stop rates could not be adjusted above 0,2% of the start rate.

Table 9 IPQ-SQ lifetimes found from H- and J-moieties in chloroform with and without visible monomer absorption. Relative abundance of the measured lifetime is given in percentages, and X^2 gives the decay fitting.

H-Decay: λ= 698 nm IPQ-SQ Without Monomer	H-Decay: λ= 698 nm IPQ-SQ With Monomer	J-Decay: λ= 768 nm IPQ-SQ Without Monomer	J-Decay: λ= 768 nm IPQ-SQ With Monomer
τ_1 : 0,29ns (26%)	τ_1 : 0,27ns (38%)	τ_1 : 0,04ns (87%)	τ_1 : 0,04ns (88%)
τ_2 : 1,44ns (60%)	τ_2 : 1,76ns (59%)	τ_2 : 2,20ns (8%)	τ_2 : 2,17ns (7%)
τ_3 : 3,36ns (13%)	τ_3 : 4,71ns (4%)	τ_3 : 7,87ns (5%)	τ_3 : 7,87ns (5%)
X^2 : 1,11	X^2 : 1,46	X^2 : 1,46	X^2 : 1,24

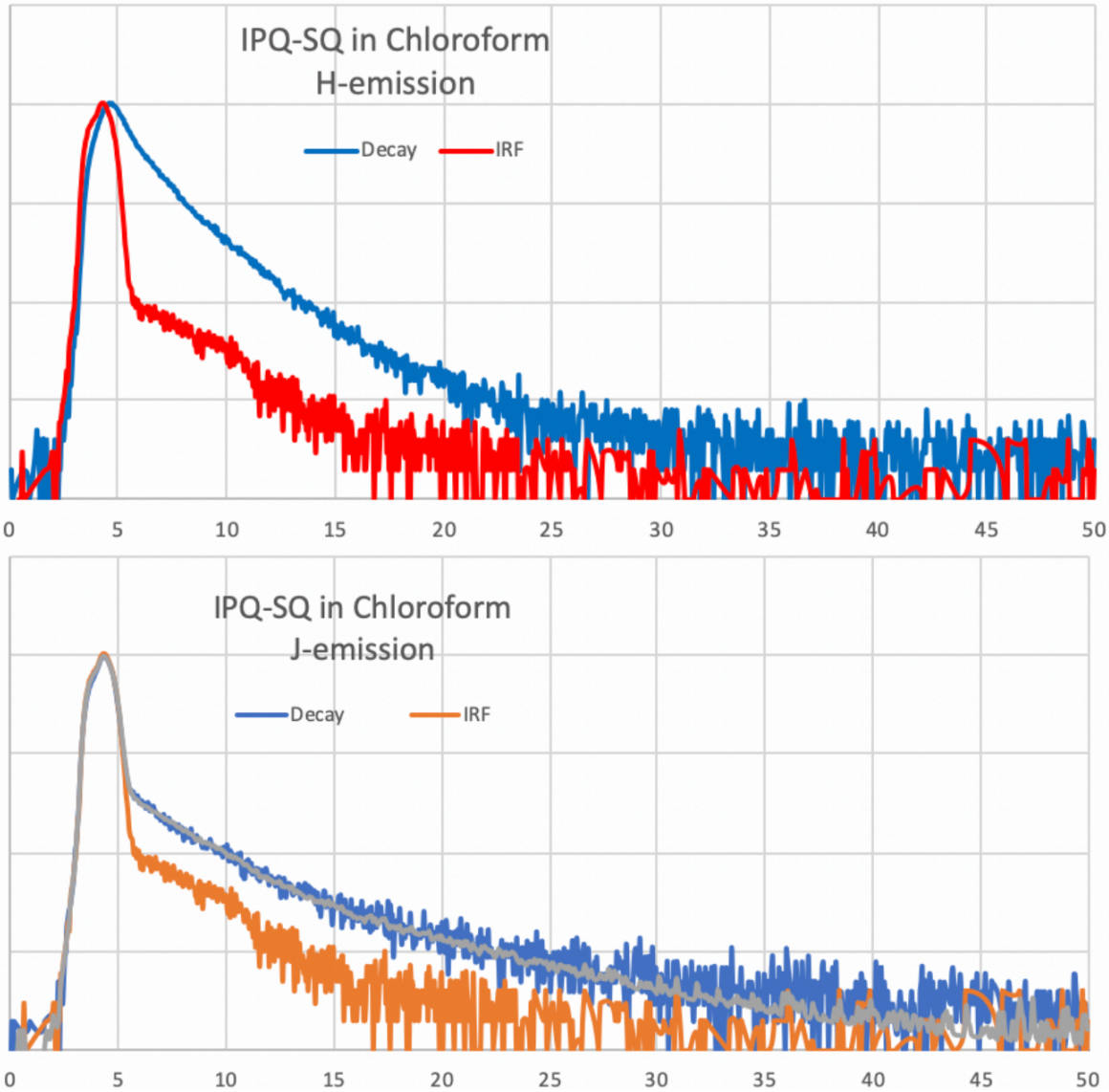

Figure 42 Decay curve, IRF and fitting line obtained for IPQ-SQ when count probing H-emission peak (Upper) and J-emission peak (lower).

Probing with a 635 pulsed laser the H-aggregate lifetimes revealed a good fit of 1,11 with a three exponential decay curve without any monomer present in solution. Fitting became less ideal when monomer moieties were in solution and an overall increase of the second and third lifetime could be observed as well as an increase of fast lifetime abundance. The "H-decay" results are presented to emphasize that the presence of monomer does have an impact on lifetimes and abundance. Regarding the H-decay, there is an ultra-fast component, in a 26% relative abundance, with a lifetime of 290 ps. The main component with a relative population of ~60% had a lifetime of 1.44 ns while a third component with a lifetime of 3.3 ns (relative population 13%) was also observed. When comparing these components to the aggregated state (without monomer absorption 708 nm) of the chromophore an increase of the relative population of the third component and a decrease in the relative population of the ultrafast 300 ps component was observed. This hints at the fact that the lifetime of ~4 ns is attributed to the monomer of the chromophore. The short lifetimes of the decay curves somewhat limits the algebraic calculation capabilities of the software, making it difficult to extract clear conclusions as to the precise assignment of the lifetimes to specific emitting species. The ultrafast process of ~300 ps as well as the main component in abundance with a shorter lifetime at 1.4-1.7 ns can be attributed to phenomena of emission quenching (charge or energy transfer) due to aggregation.

More interestingly, severe changes were present in lifetimes when the J-attributed emission was measured by the 635-laser. In both aggregated and non-aggregated state, there are 3 distinct components contributing to the emission decay curve. The main component with a lifetime of ~40 ps is found in an ~88% relative abundance with the other lifetimes being ~2 (8%) and ~8 ns (5%). It should be noted here that this value is below the theoretical measuring limit of the instrument (50 ps) and can be considered inaccurate. Additionally, when approaching the measuring limit of the instrument, combined with low count rates, scattering and dark counting could have had a considerable effect on the achieved decay curves [45, 66]. In the case of the propyl-functionalized dye it is clear that the decay curve is dominated by the ultrafast component that is approaching the instrument response. Due to the fact that the IPQ-SQ dye is more prone to aggregation, it strengthens the notion that the ultrafast process can be the result of the energy/charge transfer between aggregated dye molecules. Whether energy or charge transfer takes place requires the use of transient absorption measurements which were not available in the lab.

The indications suggesting that the instrument did not provide accurate information from J-emission maxima posed a problem as this emission range effectively governs all moieties from fully aggregated structures found in other solvents. Table 10 gives the data obtained from a TCSPC experiment performed on a IPQ-SQ 10^{-5} M monomer solution.

Table 10 Lifetimes and relative abundance of IPQ-SQ monomer

IPQ-SQ Monomer Lifetimes, λ= 721 nm			
τ_1 : 0,05ns, (94%)	τ_2 : 2,42ns, (3%)	τ_3 : 6,54ns, (3%)	X^2 : 1,41

As the data suggests, the decay curve of the IPQ-SQ diluted monomer provides similar results as from the aggregated J-emission decay curves yielding a dominant (94% relative abundance) component with a lifetime at the instrument limit (50 ps). Meaning a femto second laser as well as an instrument with corresponding detection capabilities is required to extract clear differences between these two moieties. The decay curve is not shown, as it resembles the signal obtained for the J-emission, (Figure 42) with a curve very similar to the instrument response function.

The same experiments were done with IDQ-SQ for H- and J-emission, as the monomer moiety was non-fluorescent and therefore not measurable. The resulting data can be viewed in Table 11. Generally the data presents similar trends to the IPQ-SQ dye decay curves with some notable differences which cannot be discussed in a confident manner as they fall within the analysis limit of the software. For the compounds without pyrene moieties the clear information that can be gathered is that they exhibit multiexponential lifetimes which are in good agreement with the assumption that the final aggregate structure would be similar to those found for IDQ-SQ-P as well as the emission results which state that the J- and H-emission are shared by more than one moiety when excited at 635 nm.

Table 11 TCSPC measurments of IDQ-SQ in regards to H- and J-moieties.

H-Decay: λ= 695nm IDQ-SQ Without Monomer	H-Decay: λ= 695 nm IDQ-SQ With Monomer	J-Decay: λ= 768 nm IDQ-SQ Without Monomer	J-Decay: λ= 768 nm IDQ-SQ With Monomer
τ_1 : 0,29ns (27%)	τ_1 :0,32ns (28%)	τ_1 : 0,04ns (86%)	τ_1 : 0,06ns (86%)
τ_2 : 1,48ns (57%)	τ_2 : 1,01ns (63%)	τ_2 : 1,82ns (8%)	τ_2 : 1,80ns (9%)
τ_3 : 3,23ns (16%)	τ_3 : 3,08ns (9%)	τ_3 : 6,53ns. (6%)	τ_3 : 7,38ns (5%)
X^2 : 1,19	X^2 : 1,20	X^2 : 1,30	X^2 : 1,25

When lifetime experiments were performed on the pyrene-coupled compounds IDQ- and IPQ-SQ-P, the same tendencies of ultra-fast lifetimes of high abundance were observed. Chloroform semi aggregated decay studies gave next to identical lifetimes as those done with the precursor molecules despite having an extra chromophore attached, and serve mostly as an extra confirmation of the points discussed earlier this section. As the fully aggregated structure of these compounds reveal the most important attributes concerning photovoltaic properties, some decay experiments were also conducted in aggregate inducing solvents shown in Table 12. The obtained decay histograms from IDQ-SQ-P and IPQ-SQ-P in NMP measured at 793 nm can be viewed in Figure 43.

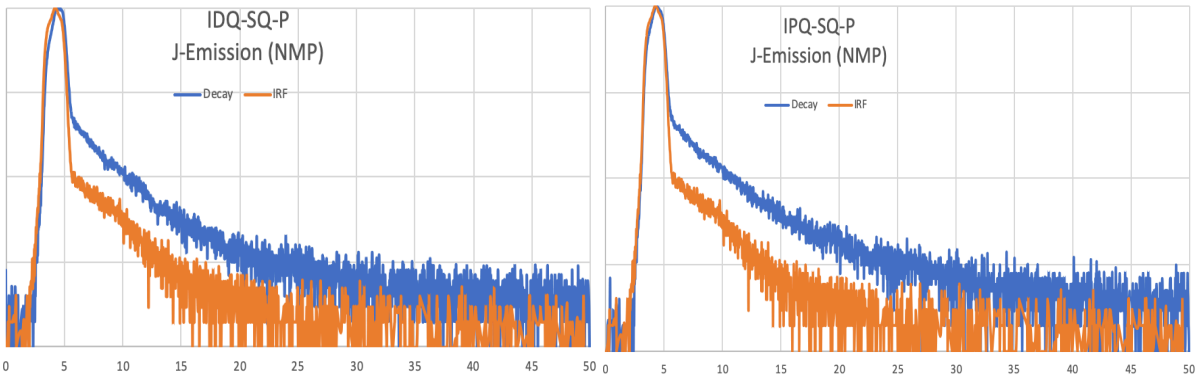

Figure 43 TCSPC measurements of IDQ-SQ-P (left) and IPQ-SQ-P (right) solved in NMP.

Table 12 Lifetimes achieved via TCSPC experiments on IPQ-, IDQ-SQ-P and IPQ-, IDQ-SQ solvated in NMP.

J-Decay: λ= 793 nm IDQ-SQ-P (NMP)	J-Decay: λ= 793 nm IPQ-SQ-P (NMP)	J-Decay: λ= 776 nm IDQ-SQ (NMP)	J-Decay: λ= 775 nm IPQ-SQ (NMP)
τ_1 : 0,04ns (90%)	τ_1 : 0,03ns (86%)	τ_1 : 0,03ns (89%)	τ_1 : 0,05ns (86%)
τ_2 : 1,85ns (6%)	τ_2 : 2,58ns (7,5%)	τ_2 : 1,91ns (6%)	τ_2 : 2,47ns (6%)
τ_3 : 5,92ns (5%)	τ_3 : 6,88ns (6,5%)	τ_3 : 7,03ns. (5%)	τ_3 : 7,12ns (5%)
X^2 : 1,75	X^2 : 1,48	X^2 : 1,29	X^2 : 1,14

The reason why J-emission decay measurements show consistent results regardless of extra molecule groups and solvents may stem from the 635 nm pulsed laser not being adequate for reliable measurements in the compounds investigated. The pulse of the laser is around 300 ps and, as mentioned, with the aid of the software provided, resolution can be as low as 50 ps. This means that lifetimes lower than that cannot be measured and differences in that region are not discernible. Additionally, as can be seen in Figure 44 the laser excites a low absorbing portion of the samples, consequently producing lower intensity emissions. Decay studies regarding the H-aggregate which produces more normal curves does, however, suggest that the small absorption area being hit is closely connected to the formation of H-aggregates.

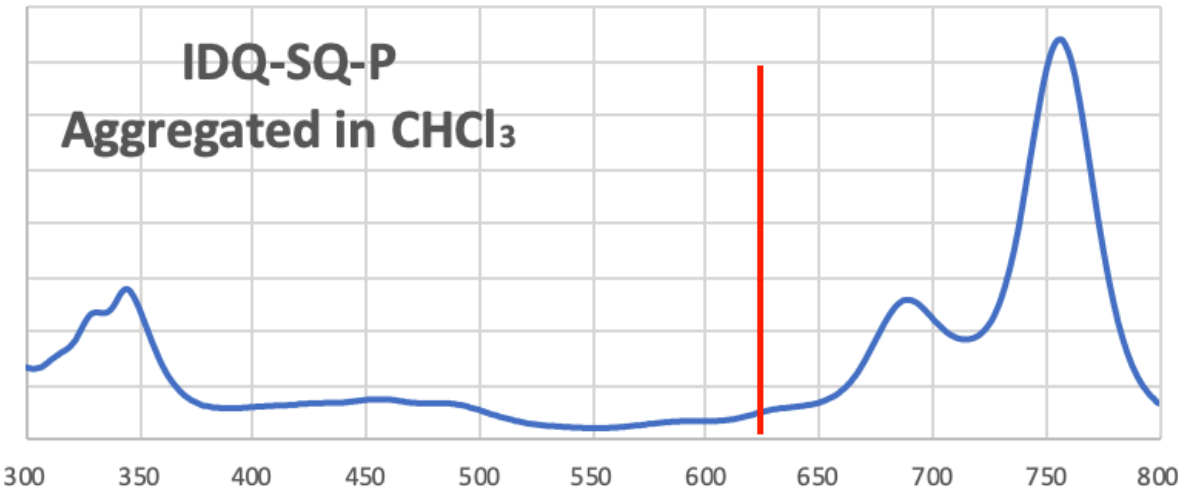

Figure 44 Absorption spectrum of IDQ-SQ-P semi aggregated in chloroform, red line marks the pulsed laser excitation area.

Summarizing the decay data there are some clear assumptions that can be drawn. When probing the H-aggregate peak in either molecule (tables 9 and 11), the bulk population of the material, ~57-63%, has a lifetime in the area of 1-2 ns. It is therefore logical to assume that this is the emission lifetime of these aggregates, since the main contribution of that emission comes from these. Conversely, when looking at the emission of the "J-peak" at 768 nm the overwhelming bulk of the material (>86%) has an emission lifetime of less than 50 ps. This can be attributed to components emitting as part of the J-aggregates. These can also be observed when probing the H-aggregates, where we can see "contributions" (~26-38%) to the decay curve from an ultrafast component (~300 ps) which is logical to assign to the J-aggregate peak and should have some kind of emission in that region. Again, better analysis of the decay curves would stem from a faster pulsed laser. That leaves the third component which has a lifetime of ~4 and 8 ns in the two materials. This cannot be attributed with any confidence, but it can be assumed

to come from the monomer emission of the actual quinoline-squaraine-quinoline trimer. The reasoning for the differences between the 4 and 8 ns lifetimes can come from two different explanations. Either the fact that simply the analysis software is not providing accurate measurements or there are two intermolecular chromophores responsible for this emission. The quinoline-squaraine dimer, or the quinoline-squaraine-quinoline trimer. In order to clarify the latter assumption, a series of experiments involving the synthesis and the study of the monosubstituted quinoline-squaraine would shed some light. However, due to time constraints this was not possible. Additionally, the study of a very dilute component capable of resisting aggregation would also provide information on the lifetime of the "monomer" emission. Any attempt to probe the monomer emission at 721 nm (table 10) simply gave the same results as the aggregated molecules. Measurements with less than 10-6 M solutions were not feasible since the experiments would require days to reach the desired statistical number of photon counts for reliable analysis.

2.7 Morphological Characterization

In order to better understand and visualize the aggregation phenomena taking place, atomic force microscopy (AFM) was employed and conducted at NTNU Nanolab. Four different solutions were prepared on atomically flat MICA substrates via drop casting to retrieve AFM images of IDQ-SQ-P in its monomer and aggregated state from chloroform solutions. One sample was also prepared of the compound in an aggregate inducing solvent (THF) as well as a IPQ-SQ-P sample from chloroform solution in its half-aggregated state. The images produced for IDQ-SQ-P in chloroform and THF are presented in Figure 45.

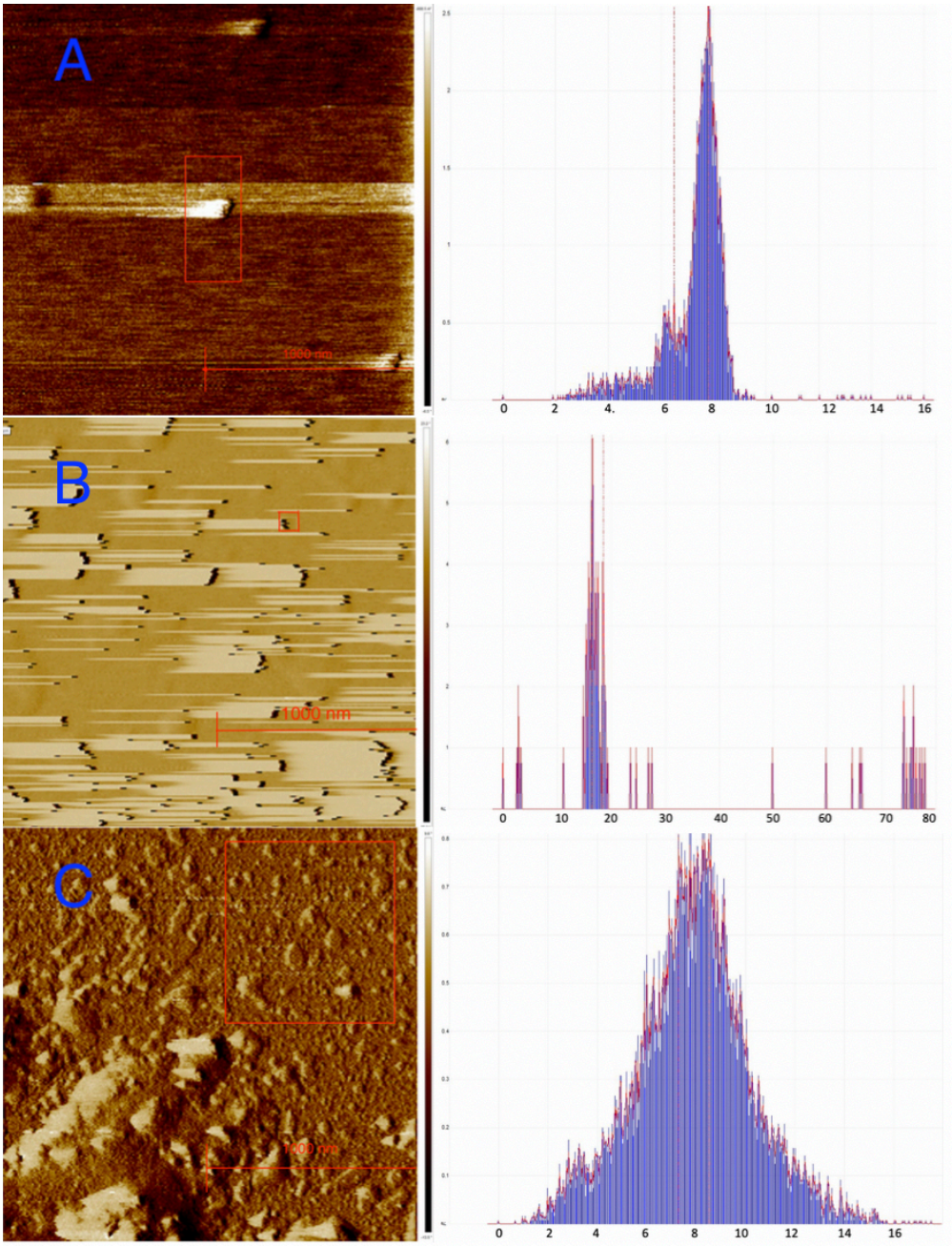

Figure 45 AFM images obtained from A) IDQ-SQ-P monomer diluted in $CHCl_3$, B) IDQ-SQ-P post aggregated in $CHCl_3$ and C) IDQ-SQ-P in THF.

From the images taken it can be seen that significant morphological differences exist between IDQ-SQ-P aggregated in chloroform and THF. Figure 45 B solution exhibits a morphology with a surface roughness of ~ 15-20 nm with some aggregates reaching height profiles of ~60-80 nm. The latter (Figure 45 C) however, shows that aggregation heights tend to stop between 6 – 10 nm. The bulk heights of THF induced aggregation are similar to the $CHCl_3$ monomer imaged sample, conveying that some aggregation has occurred, probably due to concentration gradients forming during evaporation combined with a heightened temperature of 50 ^{0}C. The

observation that THF induces overall low aggregate heights with more uniformity compared to aggregation in $CHCl_3$, indicates that using THF and possibly other aggregate inducing solvents tested in this study, might be a better option to improve uniformity of dye coverage for applications.

As previously stated in the UV/vis and reactions discussion parts the propane alkylated compounds showed tendencies of aggregating faster and in a higher order. Figure 46 shows the AFM image, height profile and absorption spectrum prior to drop casting of IPQ-SQ-P. From these data it can be confirmed that IPQ-SQ-P does indeed aggregate to higher orders than its dodecane alkylated version, revealing the bulk height to be centered around 70 – 80 nm. These images were produced from a chloroform solution where the compound was only semi-aggregated, explaining firstly the height profile containing structures ranging all from 5 – 80 nm, but more interestingly conveying that the aggregated structures could reach taller heights than those shown here. This further emphasizes the solubility struggles in chloroform which were prominent when concentrated NMR-samples of IPQ-SQ and IPQ-SQ-P were attempted to be characterized. The phenomena observed is, of course, attributed to less sterical hindrance from a propyl group than a dodecyl group, allowing for higher order structures to be made.

While not performed due to limited time on the instrument, a AFM sample of IPQ-SQ-P in an aggregate inducing solvent would be interesting to obtain in order to investigate if lower aggregation orders also would occur with this molecule.

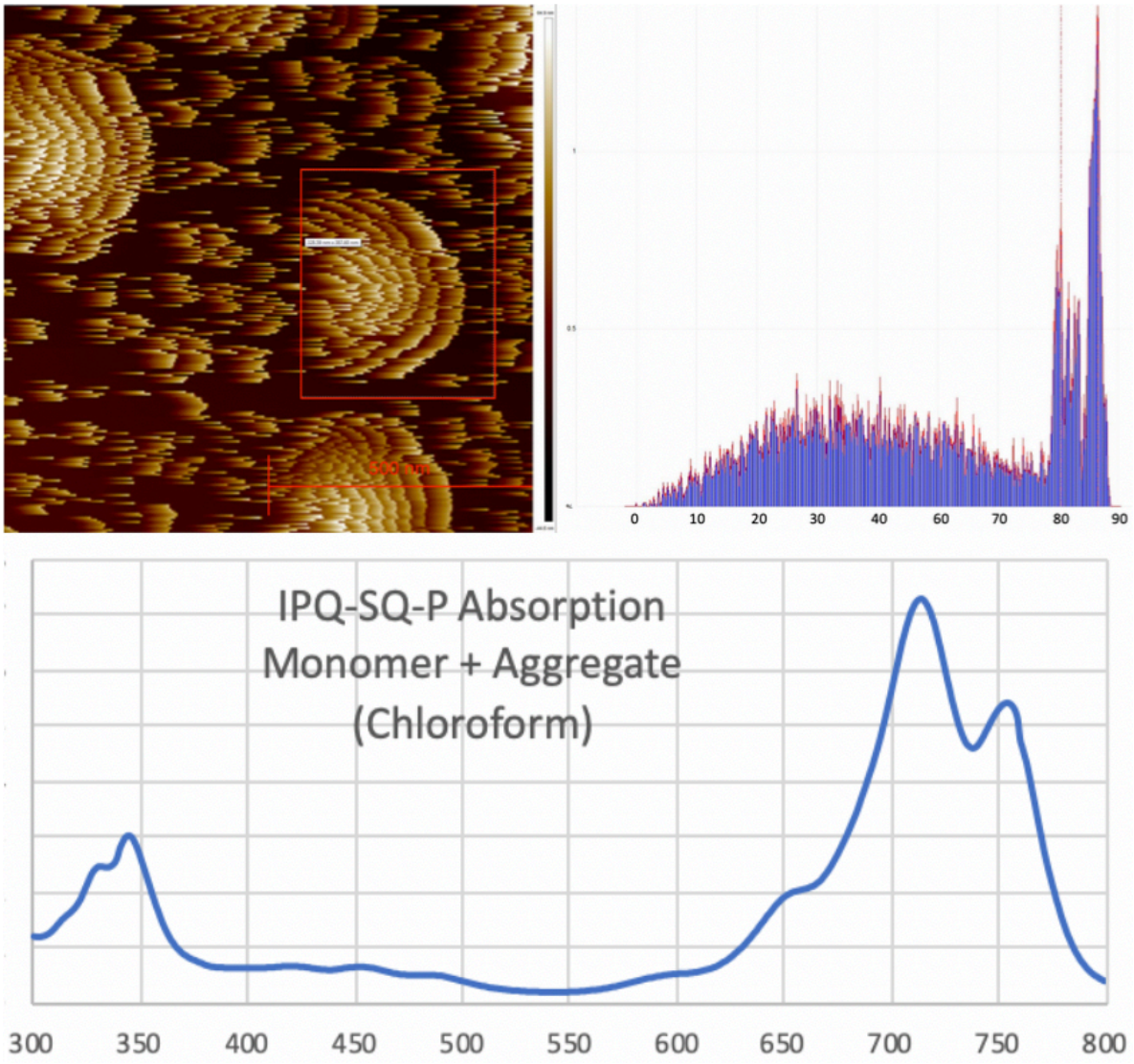

Figure 46 AFM image obtained from semi-aggregated IPQ-SQ-P chloroform solution with corresponding height profile and absorption spectra prior to drop-cast.

2.8 BHJ-Test Results and AFM Annealing Results.

IDQ-SQ-P was chosen as the representative compound to be sent for further investigation to see if these compounds were promising BHJ-cell photovoltaics. Although both compounds showed a tendency to aggregate the dodecyl chain-functionalized dye was definitely the obvious choice between the two, due to better solubility. Samples were sent to our collaborators at King Abdullah University of Science and Technology (KAUST) in Saudi Arabia.

The bulk heterojunction synthetic protocol requires 3-10 mg /ml concentrations of electron donor and acceptor and as such extensive aggregation phenomena are expected to take place. Using existing knowledge, Atomic Force Microscopy imaging of the IDQ-SQ-P dye with the

acceptor phenyl-C61-butyric acid methyl ester (PCBM) were conducted and the resulting images are shown in Figure 49.

BHJ solar cells typically undergo an annealing of the thin film after casting the blend to allow for better rearrangement of molecules, improved phase separation and favorable formation of crystalline pathways for charge extraction. Images show the morphology of the blend in "as cast" conditions and after 50 and 150 ^{0}C annealing. There are clear crystalline structures forming as the annealing temperature increases which demonstrates how the compound tends to aggregate. The high order aggregation of this compound poses a "threat" for BHJ application especially in viscous 3 mg/ml solutions. The observed crystalline nature of the aggregates suggests that the number of contact points between a selected aggregate and the fullerene (heterojunction) is expected to be limited, hence preventing efficient exciton dissociation and inhibiting the flow and collection of holes and electrons to their respective electrodes, resulting in reduced photovoltaic efficiency.

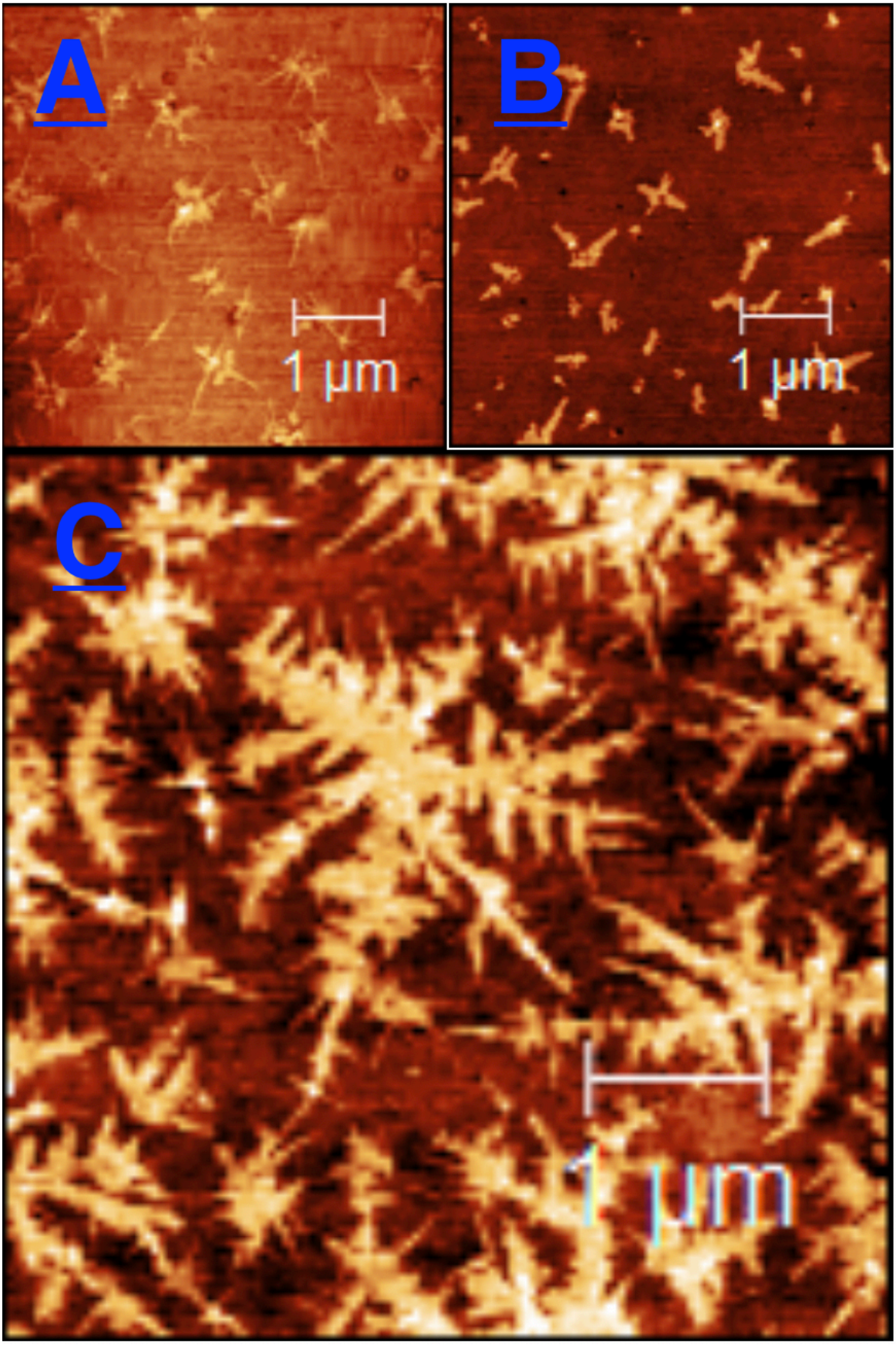

Figure 47 AFM of IDQ-SQ-P at different annealing temperatures 25 ^{0}C (A), 50 ^{0}C (B) and 150 ^{0}C (C).

The results of the solar cells fabricated are shown in Figure 48. They revealed a very poor fill factor (~28%) which is an indication of a poor diode performance, something that was expected after witnessing the extensive crystalline structures unfavorable to solar cell morphology. Short circuit current (J_{sc}) was also poor reaching 0,8 mA /cm^2. Surprisingly, open circuit voltage was also disappointing at 0.28 V. V_{oc} which a direct result of the HOMO energy level of the dye, had already been calculated through electrochemistry to be around 5.3 [6], and should not yield such low Voc. This was rather curious so PhotoElectron Spectroscopy (PESA) was performed to verify results obtained through electrochemistry. From PESA an ionization potential (HOMO) of 4.8 eV was calculated which, although is not matching the electrochemical data, provides a reasonable explanation for the low V_{oc} obtained [41].

External quantum efficiency (EQE) test of the compound also confirmed the low performance of the dye with the maximum conversion of approximately 3,5% found at the pyrene moiety absorption, see Figure 48.

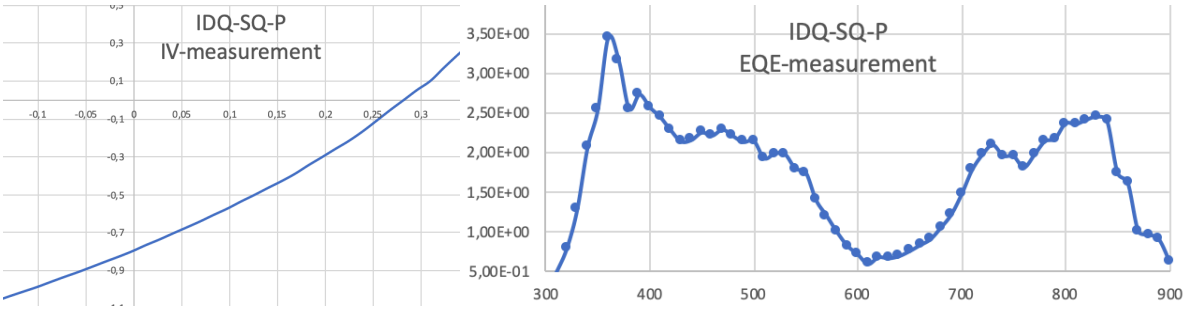

Figure 48 BHJ solar cell test results using IDQ-SQ-P, (right) I-V curve and (left) EQE spectra

Additional explanation for these findings can possibly include the structure of the dye itself. From literature mentioned in the theory section it can be assumed that electron mobility upon excitation has an affinity towards the squaraine core [14]. Pyrene is the moiety which works as a bridge towards the electron acceptor (fullerene) via pi-pi stacking and for efficient transfer, the excited electron needs to have a larger affinity towards the pyrene – fullerene bridge than other moieties. As this is a symmetrical squaraine dye it is unlikely to inhibit any strong transition dipole moments that wouldn´t be vectored towards the molecule core. Figure 13 from the "Redox Properties in Squaraine Dyes [23]" theory sub-section has been presented below to visualize electron affinity.

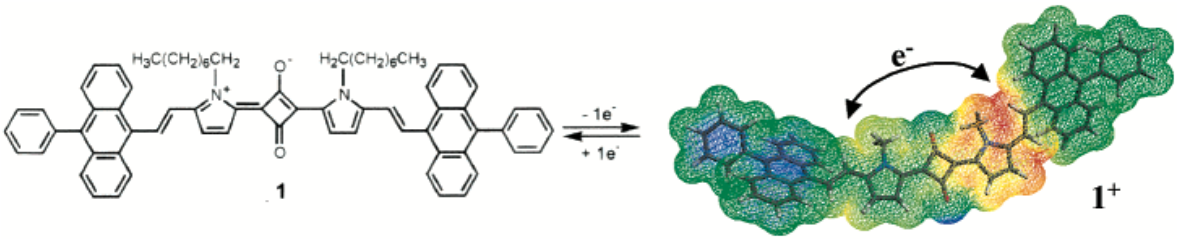

*Figure 17 Calculated charge distribution of **1**⁺ [23].*

The EQE further elaborates this by showing higher photon to current conversion for the absorption areas which are governed by pyrene, revealing both the largest conversion at 360 nm and the largest bulk conversion between 300 - 600 nm compared to the quinoline-squaraine-quinoline (Q-S-Q) attributed absorption areas. This is despite the Q-S-Q moieties having overall much larger absorption intensities found in the corresponding thin film UV/vis presented in Figure 49.

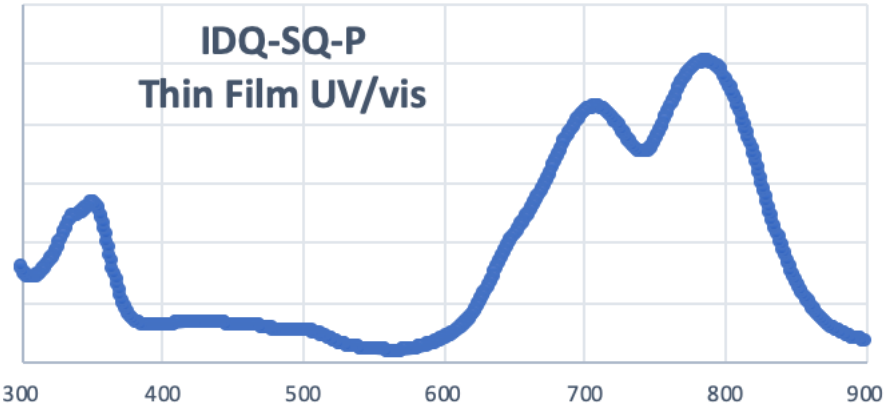

Figure 49 IDQ-SQ-P in thin film UV/vis measurement.

Interestingly the moieties between 400-600 nm which are attributed to pyrene-excimer formations “greatly” increase the overall photon to electron conversion of IDQ-SQ-P. Even simple UV/vis experiments reveal them to exhibit the lowest absorption intensities. As previously stated the excimers show an irregular emission pattern which may be due to their large exciton phonon coupling constant causing electron trapping, therefore being “more free”, or rather restricted, from the dipole moments which governs the charge carrier paths of IDQ-SQ-P. From these assumptions it can be justified that pyrene excimers would be more prone to inject the excited electron to fullerene not because of convenient dipole factors, but rather due to restrictions from them. While these assumptions can be made from comparing the relative absorption intensities of each moiety towards the differences shown by EQE, it is easier to visualize via an internal quantum efficiency (IQE) calculation shown in Figure 50. This

calculation was done using Equation 5 where reflectance was assumed non-existent as their values were not available. Keep in mind that reflectance plays a larger role in UV/vis measurements of thin films, hence the IQE should be treated as an estimate for the purpose of comparing relative differences [67].

Equation 5. $IQE = \frac{EQE}{Absorptance}$, Where Absorptance = 1 – (Transmittance + Reflectance)

As can be seen from the calculation, only the excimer attributed moieties exhibits "decent" charge transfer relative to the number of photons absorbed, while the H-aggregate attributed region has the least contribution of all moieties.

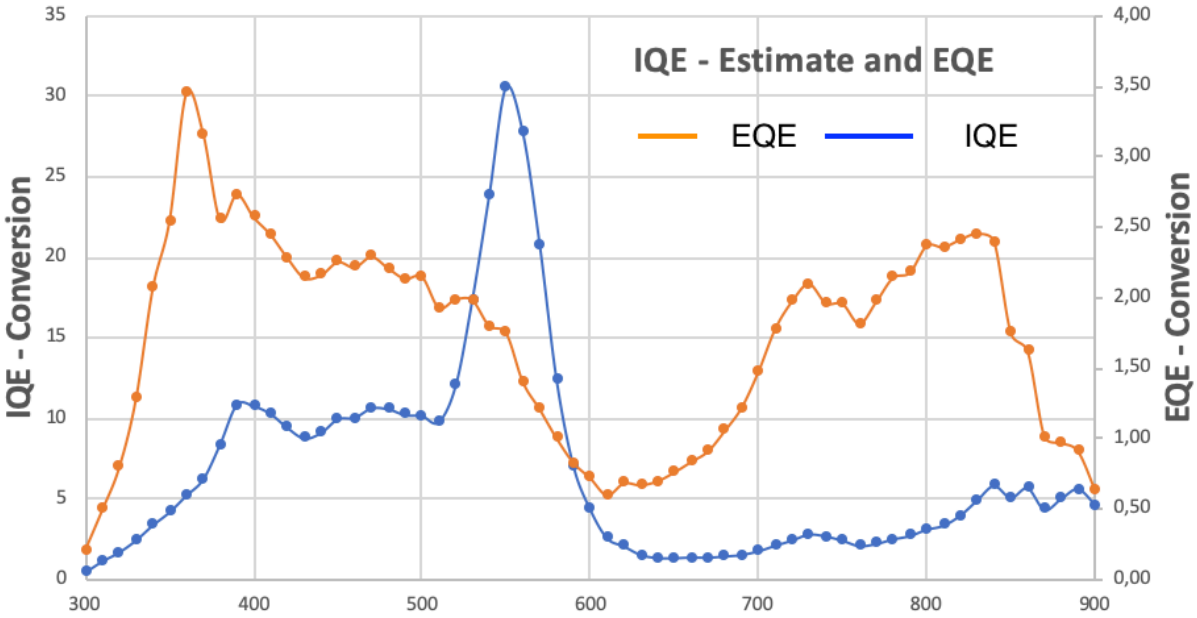

Figure 50 Estimated IQE (Blue) and EQE measurement (orange).

Though the molecular structure of the dye may contribute to the low solar cell efficiencies found, the observed aggregation phenomena and overall non-ideal thin film morphology still persists as the most severe hindrance towards BHJ application.

3. Conclusion

IDQ-, IPQ-SQ and IDQ-,IPQ-SQ-P were synthesized in acceptable yields and investigated towards their photophysical, electrochemical and morphological properties. All compounds exhibited a high tendency to aggregate in every solvent tested. Similar absorption and emission properties both in monomer and aggregated conditions were also attributed to every compound, showing 4 emission moieties when semi-aggregated in $CHCl_3$, the exception being IDQ-SQ whose monomer structure was found to be non-fluorescent. When solvated in an aggregate inducing solvent (e.g. NMP, Toluene), all moieties were found to exhibit only 1 emission maxima, attributed to charge/energy transfer towards the J-moiety of the fully aggregated structures. Significant photophysical changes were found as a result of solvent effects, which have been attributed to the cyclobutene core.

Significant morphological changes were found for the pyrene-coupled compounds IDQ-SQ-P and IPQ-SQ-P via AFM imaging. The most interesting being higher order aggregation of both molecules in chloroform, IPQ-SQ-P showing the highest, while lower order aggregation where found in the aggregate inducing solvent THF for IDQ-SQ-P. Severe solubility changes were also attributed to alkyl chain length in the synthesized squaraine dyes while.

IDQ-SQ-P was chosen for further BHJ OPV testing due to convenient solubility and was found to exhibit power conversion efficiencies of n= 0,02%, which has been attributed to crystalline aggregation structures at high concentrations disrupting efficient BHJ OPV morphology.

4. Experimental

The chemicals used during this project were of analytical quality and ordered from Sigma Aldrich and from Activate Scientific GmBH, without any further purification.

TLC analysis were performed on "Merck Millipore TLC Silica gel 60 F254 plates. Results were detected using UV-light.

The NMR spectra were achieved using a Bruker 400 MHz Avance III HD system, equipped with a 5 mm Smart-Probe Z-gradient probe.

UV/vis analysis were conducted using "HitachiU-1900" spectrometer with a light path of 10 mm.

PL spectroscopy measurements were done using a "Spectrofluorometer FS3" from Edinburgh Instruments connected to a PC running Fluoracle software.

TCSPC were conducted with a 635 nm pulsed-laser from Edinburgh Instruments attached to the Spectrofluorometer FS3. Results were obtained through the use of Fluoracle software.

Melting points were determined using a "Gallenkamp" melting point apparatus.

AFM images were obtained by Nanosurf Flex from Nanosurf (NTNU nanolab)

KAUST solar cell device fabrication:

J/V device characterization of the solar cells was performed using a solar simulator with Xenon lamp (Oriel Instruments) calibrated to 100mW/cm^2, AM1.5G, with KG-5 silicon reference cell in a N^2 enviroment with computerized Keithley 2400 SourceMeter. External quantum efficiency (EQE) was performed by illumination of the device with Xenon arc lamp; providing monochromatic light when in combination with a dual-grating monochromator. The incident photon number was calibrated using silicon photodiode by NIST across each wavelength.

UV/vis absorption spectra were obtained using a Varian Cary 5000. PhotoElectron Spectroscopy in Air (PESA) measurments were carried out at room temperature using a Riken Instruments AC-2 model to determine the ionization potential of the dye.

4.1 Alkylation of quinoline with Iodopropane

6-bromo-2-methylquinoline (0,72 g, 3,24 mmol) and iodopropane (2,16 g, 12,7 mmol) were added to a microwave tube and solved in acetonitrile. The tube was then hermetically sealed and constantly stirred in an oil bath (132 ^{0}C, 45 h). The mixture was then placed in a refrigerator before the clear yellow precipitate was filtered and washed with cold acetonitrile through a büchner-setup.

A final yield of 52% (0,665 g) with purity > 99% was obtained, m.p: 152 – 155 ^{0}C, .^{1}H-NMR (400 MHz, $CDCl_3$) δ: 1,27 (t, 3H), 2,10 (q, 2H), 3,35 (s, 3H), 5,09 (t, 2H), 8,03 (d, 1H), 8,25 (d, 1H), 8,33 (d, 1H), 8,36 (s, 1H), 8,75 (d, 1H).

4.2 Alkylation of quinoline with iodododecane.

6-bromo-2-methylquinoline (1,00 g, 4,50 mmol) and iodododecane (1,788 g, 6,0 mmol) were added to a microwave tube and solved in acetonitrile (3 ml). The tube was then hermetically sealed and constantly stirred in an oil bath at 125 ^{0}C for 72 hours. The mixture was then transferred to a round bottomed flask and the solvents removed by condensation in a rotary evaporator. Crude product was then washed with EtOAc using a büchner setup and the final yellow solid was then dried and weighed.

A final yield of 30,2% (0,705 g, 1,36 mmol) was obtained with a purity > 98%, m.p: 156 - 158 ^{0}C ^{1}H-NMR (400 MHz, CDCl3) δ: 0.90 (t, 3H), 1,27 (s, 14H), 1,41 (p, 2H), 1,65 (p, 2H), 2,00 (p, 2H), 3,35 (s, 3H), 5,09 (t, 2H), 8,06 (d, 1H), 8,21 (d, 1H), 8,28 (d, 1H), 8,37 (m, 1H), 8,78 (d, 1H).

4.3 Disubstitution of Propane Alkylated Quinoline at Squaric acid (IPQ-SQ).

IPQ (0,237 g, 0,629 mmol) and squaric acid (0,035 g, 0,306 mmol) were transferred to a round bottomed flask connected to a dean-stark azeotropic distillation setup. A mixture of benzene/1-butanol (50/50 V%) and pyridine (1 ml) was then added to the round bottomed flask before the mixture was heated by oil bath under stirring (95 ^{0}C, 24 h). Solvents were then removed by condensation in a rotary evaporator and the crude product washed with acetonitrile via filtration in a büchner-setup. The final product consisting of a green solid was then dried overnight and weighed.

A final yield of 77% (0,173 g, 0,235 mmol) was acquired with a purity > 97%, Rf : 0,47 ($CHCl_3$/MeOH 9:1), m.p : 324 - 327 ^{0}C 1H-NMR (400MHz, $CDCl_3$) δ: 1,17 (t, 6H), 1,91 (q, 4H), 4,11 (t, 4H), 5,80 (s, 2H), 7,18 (d, 2H), 7,34 (d, 2H), 7,59 (d, 2H), 7,62 (s, 2H), 9,38 (d, 2H).

4.4 Disubstitution of Iodododecane Alkylated Quinoline at Squaric Acid. (IDQ-SQ)

6-bromo-1-dodecyl-2-methylquinolin-1-ium (0,411 g, 0,79 mmol) and squaric acid (0,041g, 0,36 mmol) was added to a round bottomed flask and solved in 1-butanol/ benzene (1:1) with the addition of pyridine (1 ml). The round bottomed flask was then attached to a dean-stark azeotropic distillation setup and heated via oil bath (95 ^{0}C, 20h). Solvents were evaporated in vacuo and crude product was then flushed with EtOAc through a silica packed colon before EtOAc was removed in a rotary evaporator. Remaining pyridine residues in the solid were removed by phase separation using dichloromethane and distilled water of which the organic phases were collected and solvent removed by condensation in a rotary evaporator. The final red metallic solid was then dried overnight and weighed.

A final yield of 96% (0,351 g, 0,349 mmol) with a purity > 95% was acquired, Rf : 0,74 (CHCl3/MeOH 9:1) m.p: 234 - 237 ^{0}C . 1HNMR (400 MHz, CDCl3) δ: 0,88 (t, 6H), 1,28 (m, 28H), 1,42 (p, 4H), 1,53 (p, 4H), 1,86 (m, 4H), 4,14 (t, 4H), 5,79 (s, 2H), 7,18 (d, 2H), 7,34 (d, 2H), 7,57 (dd, 2H), 7,60 (d, 2H), 9,35 (d, 2H).

4.5 Pyrene IPQ-SQ Suzuki Cross-coupling (IPQ-SQ-P).

IPQ-SQ (0,100 g, 0,136 mmol), pyrene-1-boronic acid (0,69 g, 0,28 mmol) were solved in dioxane and degassed for 30 min using nitrogen gas. The mixture was then transferred to a round bottomed flask in a reflux setup containing $Pd(OAc)_2$ (0,002 g, 0,009 mmol) and SPhos (0,012 g, 0,029 mmol). Mixture was then heated to 80 ^{0}C before a degassed solution of K_3PO_4 (4 ml 0,23 mM) was added sequentially throughout the course of the reaction (24h). The mixture was then transferred to a separatory funnel with the addition of chloroform to induce phase separation, aqueous phase was washed three times with chloroform before all organic phases were collected and dried over $MgSO_4$. Solvents were then removed by condensation in

a rotary evaporator and the crude product was washed with EtOAc through silica gel leaving the final product which was flushed using chloroform/MeOH (8:2).

A final yield of 28% (0,037g, 0,0378 mmol) was obtained, Rf : 0,13 (CHCl3/MeOH 9:1), m.p : 312 – 317 ^{0}C, ^{1}H-NMR (400 MHz, CDCl3) δ: 1,26 (t, 6H), 2,05 (sxt, 4H), 4,30 (t, 4H), 5,91 (s, 2H), 7,54 (d, 2H), 7,58 (d, 2H), 7,79 (s, 2H), 7,83 (d, 2H), 8,00 – 8,30 (m, 18H), 9,48 (d, 2H).

4.6 Pyrene IDQ-SQ Suzuki Cross-coupling (IDQ-SQ-P).

IDQ-SQ (0,100 g, 0,101 mmol), pyrene-1-boronic acid (0,86 g, 0,35 mmol) were solved in dioxane and degassed for 30 min using nitrogen gas. The mixture was then transferred to a round bottomed flask in a reflux setup containing $Pd(OAc)_2$ (0,003 g, 0,013 mmol) and SPhos (0,016 g, 0,039 mmol). Mixture was then heated to 70 ^{0}C before a degassed solution of K_3PO_4 (3 ml, 0,23 mM) was added sequentially throughout the course of the reaction (24h). The mixture was then transferred to a separatory funnel with the addition of chloroform to induce phase separation, aqueous phase was washed two times with chloroform before all organic phases were collected and dried over $MgSO_4$. Solvents were then removed by condensation in a rotary evaporator and the crude product was washed with EtOAc (9:1) through silica gel leaving the final product which was flushed using chloroform.

A final yield of 56% (0,07g, 0,56 mmol) was obtained with a purity > 99%, Rf : 0,53 (CHCl3/MeOH 9:1) , m.p : 217 – 221 ^{0}C ^{1}H-NMR (400 MHz, $CDCl_3$) δ: 0,87 (t, 6H), 1,27 (s, 26H), 1,92 (m, 4H), 4,18 (t, 4H), 5,82 (s, 2H), 7,44 (d, 2H), 7,52 (d, 2H), 7,74 (s, 2H), 7,77 (d, 2H), 7,97 – 8,25 (m, 18H), 9,42 (d, 2H). ^{13}C-NMR (400 MHz, $CDCl_3$) δ: 14,15 22,72 26,77 26,98 29,38 29,44 29,62 29,67 29,70 29,98 31,94 48,20 93,01 114,33 124,51 124,85 125,03 125,40 126,20 127,28 127,38127,56 128,50 130,09 130,20 131,49 131,67 132,64 133,48 135,71 136,72 138,88 150,05 150,09.

References

1. Chen, G., Si, C., Zhang, P., Wei, B., Zhang, J., Hong, Z., ... & Kido, J. (2017). The effect of processing solvent dependent film aggregation on the photovoltaic performance of squaraine: PC71BM bulk heterojunction solar cells. Organic Electronics, 51, 62-69.
2. *Beverina, L., & Salice, P. (2010). Squaraine compounds: tailored design and synthesis towards a variety of material science applications. European journal of organic chemistry, 2010(7), 1207-1225.*
3. *Ajayaghosh, A. (2005). Chemistry of squaraine-derived materials: near-IR dyes, low band gap systems, and cation sensors. Accounts of Chemical Research, 38(6), 449-459.*
4. *Law, K. Y. (1993). Organic photoconductive materials: recent trends and developments. Chemical Reviews, 93(1), 449-486.*
5. Merritt, V.Y., & Hovel, H. J. (1976). Organic solar cells of hydroxy squarylium. Applied Physics Letters, 29(7), 414-415.
6. *Ehlert, P. (2018). Synthesis of Light Harvesting Molecules Based on Squaraine Chromophores to Maximize Solar Absorption in Organic Photovoltaics (Master's thesis, NTNU).*
7. Kasha, M., Rawls, H. R., & El-Bayoumi, M. A. (1965). The exciton model in molecular spectroscopy. Pure and applied Chemistry, 11(3-4), 371-392.
8. Goftar, M.K., Moradi, K., & Kor, N. M. (2014). Spectroscopic studies on aggregation phenomena of dyes. European Journal of Experimental Biology, 4(2), 72-81.
9. Zhang, L., & Cole, J. M. (2017). Dye aggregation in dye-sensitized solar cells. Journal of Materials Chemistry A, 5(37), 19541-19559.
10. *Buncel, E., McKerrow, A. J., & Kazmaier, P. M. (1992). Solvent-controlled aggregation of a photoconductive dye. Journal of the Chemical Society, Chemical Communications, (17), 1242-1243.*
11. *CHAPTER4 SOLUTION AND SOLID-STATE AGGREGATION PROPERTIES OF SQUARAINE DYES DERIVED FROM STYRYLPYRROLES. Retrieved from http://shodhganga.inflibnet.ac.in/bitstream/10603/152437/9/09_chapter%204.pdf 14/12/18.*
12. *Das, S., Thomas, K. G., Thomas, K. J., Madhavan, V., Liu, D., Kamat, P. V., & George, M. V. (1996). Aggregation behavior of water soluble bis (benzothiazolylidene) squaraine derivatives in aqueous media. The Journal of Physical Chemistry, 100(43), 17310-17315.*
13. *Basheer, Alex, S.,M. C., Arun, K. T., Ramaiah, D., & Das, S. (2007). Aggregation properties of heavy atom substituted squaraine dyes: Evidence for the formation of J-type dimer aggregates in aprotic solvents. The Journal of Physical Chemistry A, 111(17), 3226-3230.*
14. Alex, S., Santhosh, U., & Das, S. (2005). Dye sensitization of nanocrystalline TiO2: enhanced efficiency of unsymmetrical versus symmetrical squaraine dyes. Journal of Photochemistry and Photobiology A: Chemistry, 172(1), 63-71.
15. *Sreejith, S., Carol, P., Chithra, P., & Ajayaghosh, A. (2008). Squaraine dyes: a mine of molecular materials. Journal of Materials Chemistry, 18(3), 264-274.*

16. *Chen, C., Dong, H., Chen, Y., Guo, L., Wang, Z., Sun, J. J., & Fu, N. (2011). Dual-mode unsymmetrical squaraine-based sensor for selective detection of Hg 2+ in aqueous media. Organic & biomolecular chemistry, 9(23), 8195-8201.*
17. Gordillo, R., Dudding, T., Anderson, C. D., & Houk, K. N. (2007). Hydrogen Bonding Catalysis Operates by Charge Stabilization in Highly Polar Diels− Alder Reactions. Organic letters, 9(3), 501-503.
18. Wells, J.A., Cunningham, B. C., Graycar, T. P., & Estell, D. A. (1986). Importance of hydrogen-bond formation in stabilizing the transition state of subtilisin. Phil. Trans. R. Soc. Lond. A, 317(1540), 415-423.
19. Thomas, K.G., Das, S., Ramanathan, R., George, M. V., & Kamat, P. V. (1993). Photochemistry of squaraine dyes. 6. Solvent hydrogen bonding effects on the photophysical properties of bis (benzothiazolylidene) squaraines. The Journal of Physical Chemistry, 97(51), 13625-13628.
20. *Electron Donating and Electron Withdrawing Groups*. 2011 Sep 29. 2011 [cited 2019 09/06/2019]; Available from: http://c-book.info/watch/E9vc9Zmgd1g.
21. *Paternò, G. M., Barbero, N., Galliano, S., Barolo, C., Lanzani, G., Scotognella, F., & Borrelli, R. (2018). Excited state photophysics of squaraine dyes for photovoltaic applications: an alternative deactivation scenario. Journal of Materials Chemistry C, 6(11), 2778-2785.*
22. *Kamat, P. V., Das, S., Thomas, K. G., & George, M. V. (1992). Photochemistry of squaraine dyes. 1. Excited singlet, triplet, and redox states of bis [4-(dimethylamino) phenyl] squaraine and bis [4-(dimethylamino)-2-hydroxyphenyl] squaraine. The Journal of Physical Chemistry, 96(1), 195-199.*
23. *Büschel, M., Ajayaghosh, A., Arunkumar, E., & Daub, J. (2003). Redox-switchable squaraines with extended conjugation. Organic letters, 5(17), 2975-2978.*
24. *Ajayaghosh, A. (2003). Donor–acceptor type low band gap polymers: polysquaraines and related systems. Chemical Society Reviews, 32(4), 181-191.*
25. *Shi, Q., Chen, W. Q., Xiang, J., Duan, X. M., & Zhan, X. (2011). A low-bandgap conjugated polymer based on squaraine with strong two-photon absorption. Macromolecules, 44(10), 3759-3765.*
26. O'regan, B., & Grätzel, M. (1991). A low-cost, high-efficiency solar cell based on dye-sensitized colloidal TiO2 films. nature, 353(6346), 737.
27. *"Dye Solar Cell Assembly Instructions". Solaronix. Archived from the original on 28 September 2007. Retrieved 22 May 2007.*
28. Hara, K., & Koumura, N. (2009). Organic dyes for efficient and stable dye-sensitized solar cells. Alternative Energy Photovoltaics, Ionic Liquids, and MOFs, 91.
29. *Chapter 5. DSSC´s Reatrieved from https://www.openlearning.com/courses/solar-cell-technology/1489456597732/lecture_notes/58c74e02044f8557e85820f6/6_CHAPTER_5_DSSC.pptx 01/12/18.*
30. *Chaudhri, N., Sawhney, N., Madhusudhan, B., Raghav, A., Sankar, M., & Satapathi, S. (2017). Effect of functional groups on sensitization of dye-sensitized solar cells (DSSCs) using free base porphyrins. Journal of Porphyrins and Phthalocyanines, 21(03), 222-230.*
31. Jose, R., Kumar, A., Thavasi, V., Fujihara, K., Uchida, S., & Ramakrishna, S. (2008). Relationship between the molecular orbital structure of the dyes and photocurrent density in the dye-sensitized solar cells. Applied Physics Letters, 93(2), 023125.

32. *Rafique, S., Abdullah, S. M., Sulaiman, K., & Iwamoto, M. (2018). Fundamentals of bulk heterojunction organic solar cells: An overview of stability/degradation issues and strategies for improvement. Renewable and Sustainable Energy Reviews, 84, 43-53.*
33. *Heeger, A. J. (2014). 25th anniversary article: bulk heterojunction solar cells: understanding the mechanism of operation. Advanced Materials, 26(1), 10-28.*
34. *Mikhnenko, O. V., Blom, P. W., & Nguyen, T. Q. (2015). Exciton diffusion in organic semiconductors. Energy & Environmental Science, 8(7), 1867-1888.*
35. *Markov, D. E., Amsterdam, E., Blom, P. W., Sieval, A. B., & Hummelen, J. C. (2005). Accurate measurement of the exciton diffusion length in a conjugated polymer using a heterostructure with a side-chain cross-linked fullerene layer. The Journal of Physical Chemistry A, 109(24), 5266-5274.*
36. *Walker, B., Tamayo, A. B., Dang, X. D., Zalar, P., Seo, J. H., Garcia, A., ... & Nguyen, T. Q. (2009). Nanoscale phase separation and high photovoltaic efficiency in solution-processed, small-molecule bulk heterojunction solar cells. Advanced Functional Materials, 19(19), 3063-3069.*
37. Yeh, N., & Yeh, P. (2013). Organic solar cells: Their developments and potentials. Renewable and Sustainable Energy Reviews, 21, 421-431.
38. *Menke, S. M., Luhman, W. A., & Holmes, R. J. (2013). Tailored exciton diffusion in organic photovoltaic cells for enhanced power conversion efficiency. Nature materials, 12(2), 152.*
39. *Sajjad, M. T., Blaszczyk, O., Jagadamma, L. K., Roland, T. J., Chowdhury, M., Ruseckas, A., & Samuel, I. D. (2018). Engineered exciton diffusion length enhances device efficiency in small molecule photovoltaics. Journal of Materials Chemistry A, 6(20), 9445-9450.*
40. *Solar Cells: A Guide to Theory and Measurement*. [cited 2019 10/06]; Available from: https://www.ossila.com/pages/solar-cells-theory.
41. *Brabec, C. J., Cravino, A., Meissner, D., Sariciftci, N. S., Fromherz, T., Rispens, M. T., ... & Hummelen, J. C. (2001). Origin of the open circuit voltage of plastic solar cells. Advanced Functional Materials, 11(5), 374-380.*
42. *Skoog, Douglas A.; Holler, F. James; Crouch, Stanley R. (2007). Principles of Instrumental Analysis (6th ed.). Belmont, CA: Thomson Brooks/Cole. pp. 169–173.*
43. *Epperson, P. M., Sweedler, J. V., Bilhorn, R. B., Sims, G. R., & Denton, M. B. (1988). Applications of charge transfer devices in spectroscopy. Analytical Chemistry, 60(5), 327A-335A.*
44. *Swinehart, D. F. (1962). The beer-lambert law. Journal of chemical education, 39(7), 333.*
45. *Introduction to time-resolved spectroscopy With applications in biophysics and physical chemistry.* p. 29-44.
46. *How Does AFM Work?* 20/05/19; Available from: https://www.nanosurf.com/en/how-afm-works/afm-operating-principle.
47. *De Oliveira, R. R. L., Albuquerque, D. A. C., Cruz, T. G. S., Yamaji, F. M., & Leite, F. L. (2012). Measurement of the nanoscale roughness by atomic force microscopy: basic principles and applications. In Atomic force microscopy-imaging, measuring and manipulating surfaces at the atomic scale. IntechOpen.*
48. *Iqbal, N., Hashim, J., Ali, S. A., al-Rashida, M., Alharthy, R. D., Ahmad, S., ... & Hameed, A. (2015). Solvent-free 1 H-tetrazole, 1, 2, 5, 6-tetrahydronicotinonitrile and*

pyrazole synthesis using quinoline based ionic fluoride salts (QuFs): thermal and theoretical studies. RSC Advances, 5(115), 95061-95072.

49. *Lange's Handbook of Chemistry, 10th ed. pp1496-1505.*
50. *CRC Handbook of Chemistry and Physics, 44th ed. pp 2143-2184.*
51. *Yardley-Jones, A.; Anderson, D.; Parke, D. V. (1991). "The toxicity of benzene and its metabolism and molecular pathology in human risk assessment". British Journal of Industrial Medicine. 48 (7): 437–44. PMC 1035396. PMID 1854646.*
52. *Tomer, K. B., Crow, F. W., Gross, M. L., & Kopple, K. D. (1984). Fast-atom bombardment combined with tandem mass spectrometry for the determination of cyclic peptides. Analytical chemistry, 56(6), 880-886.*
53. *Ewing, G. W., & Steck, E. A. (1946). Absorption Spectra of Heterocyclic Compounds. I. Quinolinols and Isoquinolinols1. Journal of the American Chemical Society, 68(11), 2181-2187.*
54. *Horii, Hideo & Abe, Yasuo & Taniguchi, Setsuo. (1986). ABSORPTION SPECTRUM OF THE SQUARIC ACID RADICAL.. 1. 83-86. .*
55. *Jyothish, K., Arun, K. T., & Ramaiah, D. (2004). Synthesis of novel quinaldine-based squaraine dyes: effect of substituents and role of electronic factors. Organic letters, 6(22), 3965-3968.*
56. *Avirah, R. R., Jyothish, K., Suresh, C. H., Suresh, E., & Ramaiah, D. (2011). Novel semisquaraine regioisomers: isolation, divergent chemical reactivity and photophysical properties. Chemical Communications, 47(48), 12822-12824.*
57. *Liu, T., Yang, L., Zhang, J., Liu, K., Ding, L., Peng, H., ... & Fang, Y. (2019). Squaraine-hydrazine adducts for fast and colorimetric detection of aldehydes in aqueous media. Sensors and Actuators B: Chemical.*
58. *Stolov, A. A., Kamalova, D. I., Borisover, M. D., Solomonov, B. N., & Remizov, A. B. (1994). Hydrogen bonds formed by methyl groups of acetonitrile: infrared and calorimetric study. Spectrochimica Acta Part A: Molecular Spectroscopy, 50(1), 145-150.*
59. *I. S. Pominov, Dissertation. Kazan (1969).*
60. *Headen, T. F., Howard, C. A., Skipper, N. T., Wilkinson, M. A., Bowron, D. T., & Soper, A. K. (2010). Structure of π− π Interactions in Aromatic Liquids. Journal of the American Chemical Society, 132(16), 5735-5742.*
61. *Ray, G. B., Chakraborty, I., & Moulik, S. P. (2006). Pyrene absorption can be a convenient method for probing critical micellar concentration (cmc) and indexing micellar polarity. Journal of colloid and interface science, 294(1), 248-254.*
62. *Hong, Y., Lam, J. W., & Tang, B. Z. (2011). Aggregation-induced emission. Chemical Society Reviews, 40(11), 5361-5388.*
63. *Dimitriev, O. P., Piryatinski, Y. P., & Slominskii, Y. L. (2018). Excimer emission in J-aggregates. The journal of physical chemistry letters, 9(9), 2138-2143.*
64. *Huang, Y. F., Shiu, Y. J., Hsu, J. H., Lin, S. H., Su, A. C., Peng, K. Y., ... & Fann, W. S. (2007). Aggregate versus excimer emissions from poly (2, 5-di-n-octyloxy-1, 4-phenylenevinylene). The Journal of Physical Chemistry C, 111(14), 5533-5540.*
65. *Matsui, A. H. (1995). Excitonic processes in aromatic molecular crystals of strong exciton-phonon coupling. Pure and applied chemistry, 67(3), 429-436.*
66. HORIBA Jobin Yvon IBH Ltd, G., Scotland, UK., *A practical guide to time-resolved luminescence lifetime determination using dedicated Time-Correlated Single-Photon Counting systems.*: p. 24-27.

67. *Zhao, H. (2013). Light Trapping for Silicon Solar Cells: Theory and Experiment.*

Analytical Data

IDQ-SQ-P NMR Data

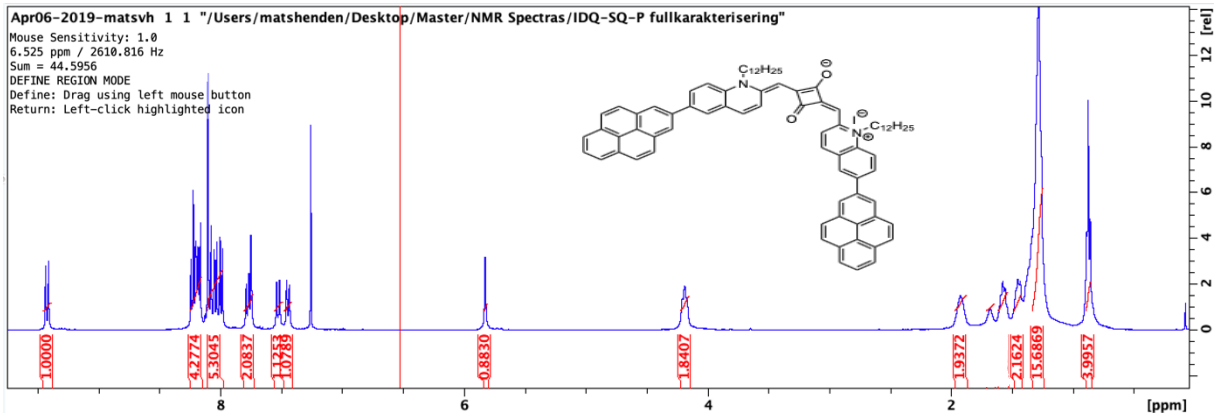

H-NMR Full Spectrum : IDQ-SQ-P

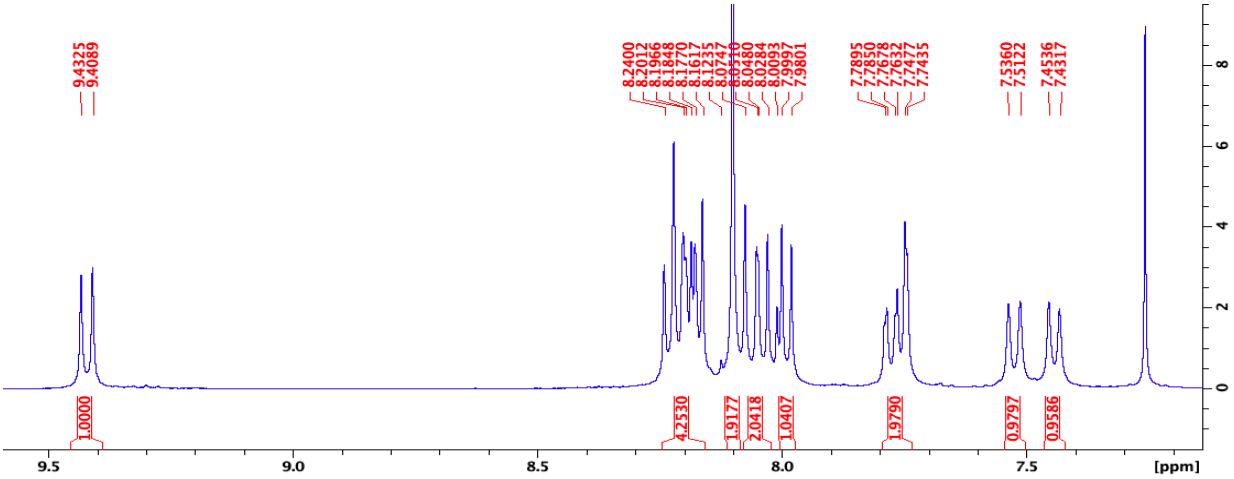

H-NMR Zoomed : IDQ-SQ-P

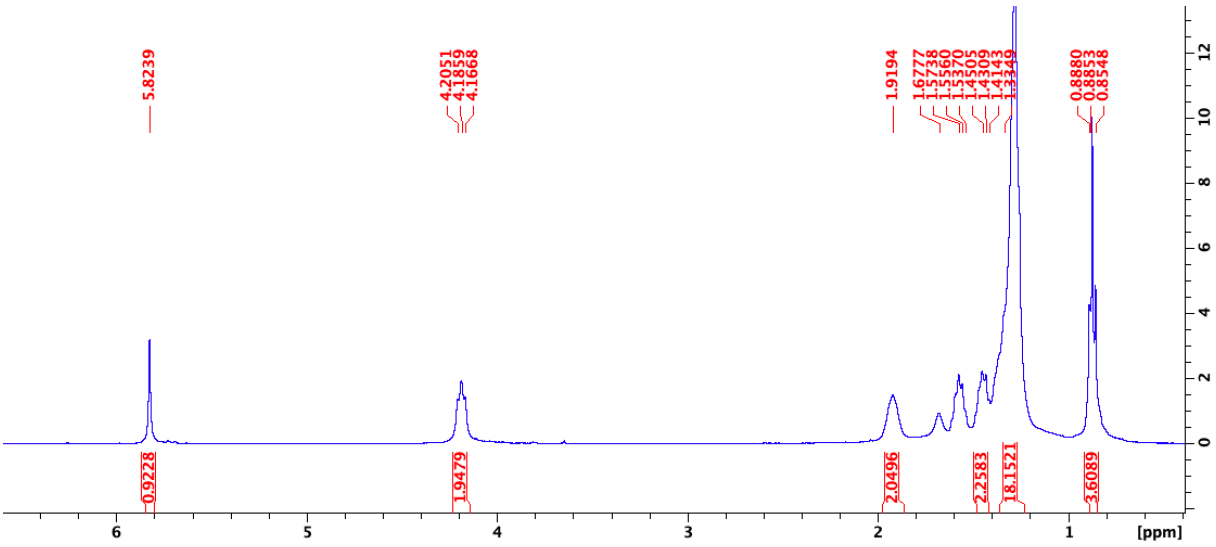

H-NMR Zoomed : IDQ-SQ-P

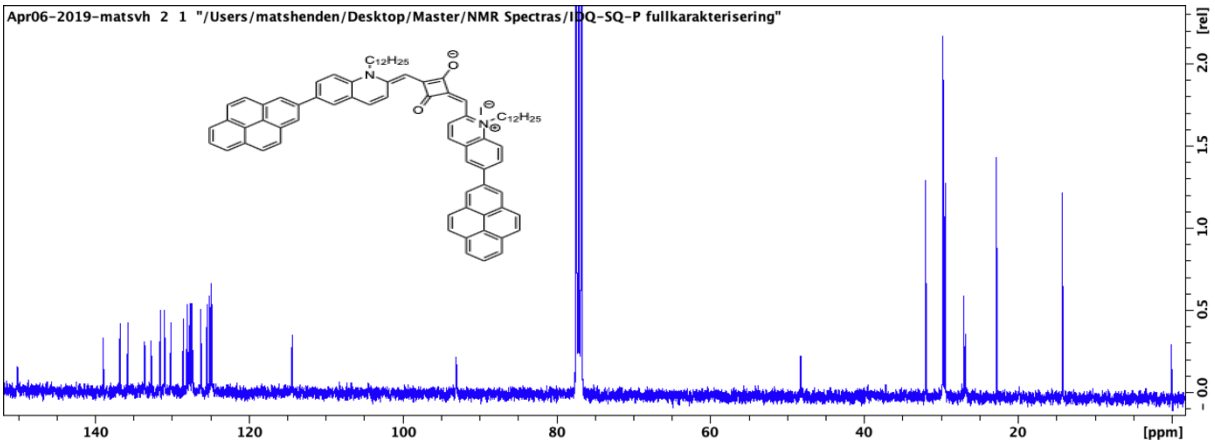

C-NMR Full Spectrum : IDQ-SQ-P

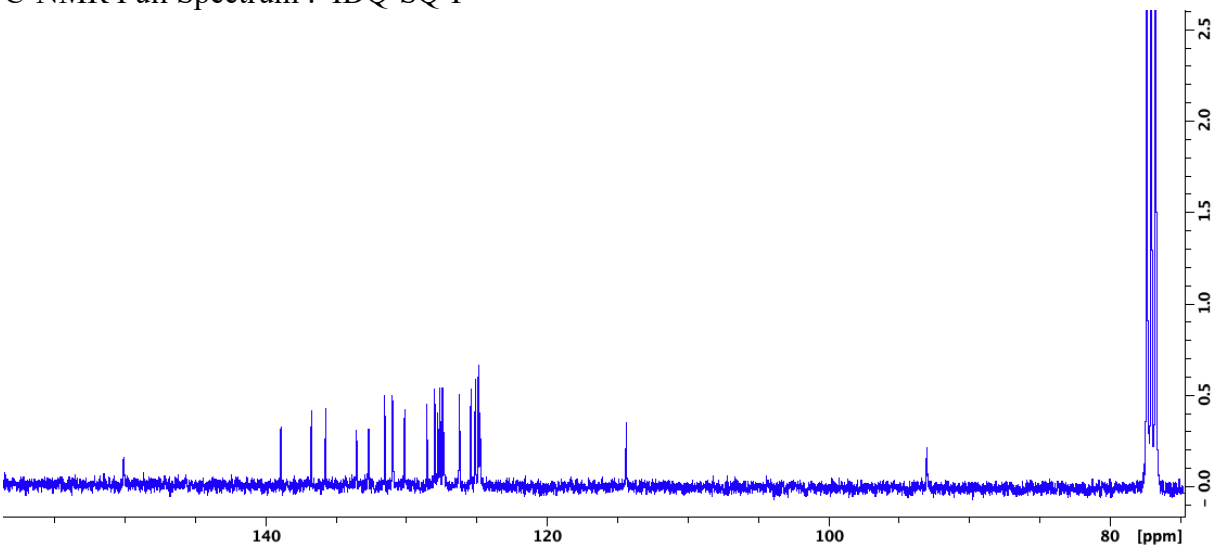

C-NMR Zoomed : IDQ-SQ-P

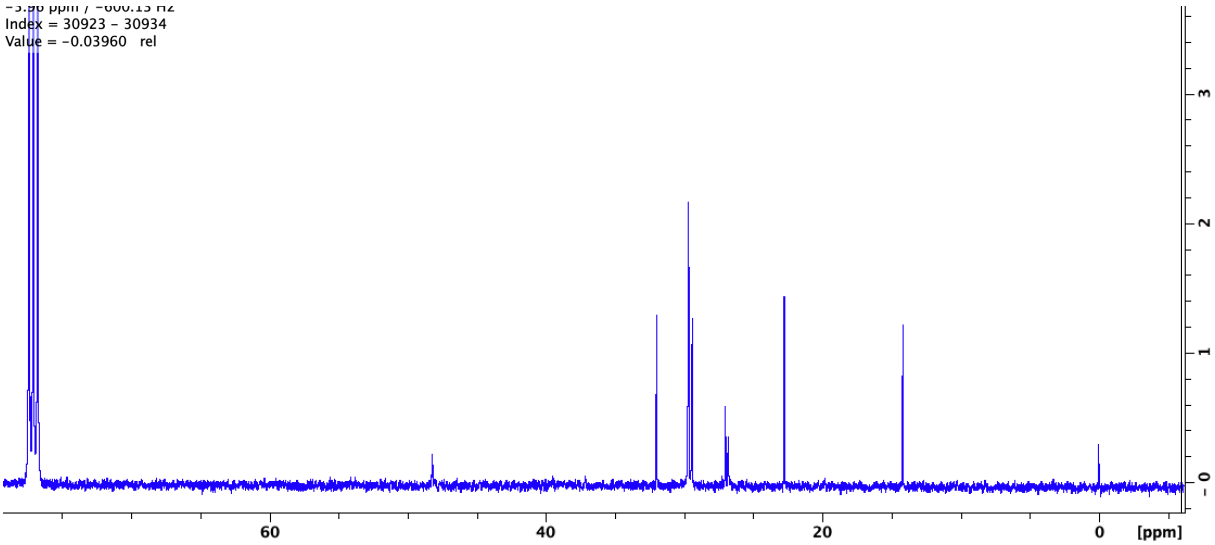

C-NMR Zoomed : IDQ-SQ-P

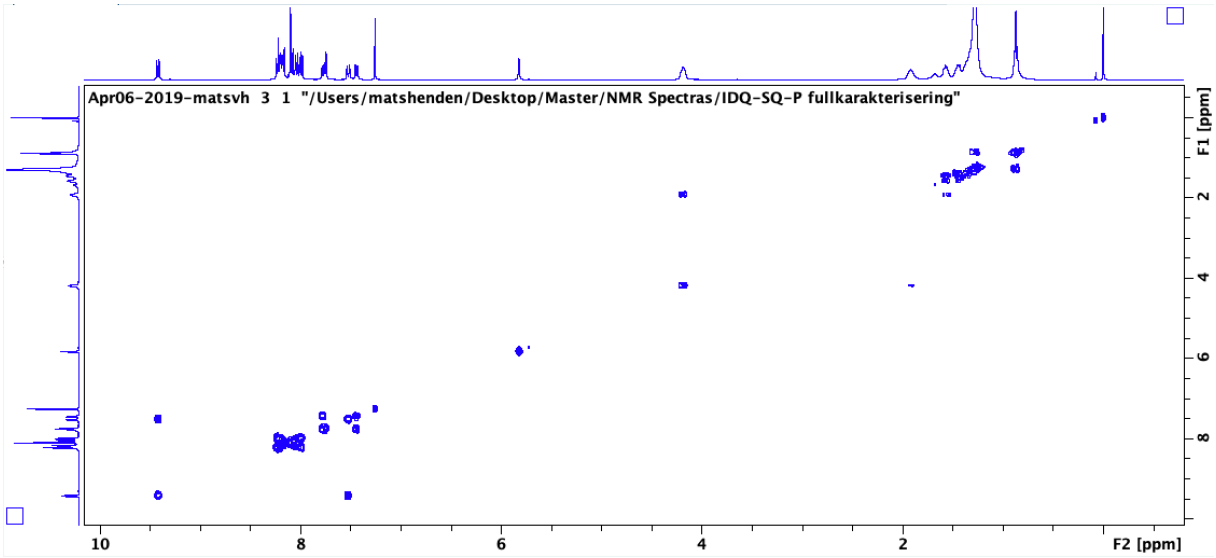

COSY: IDQ-SQ-P

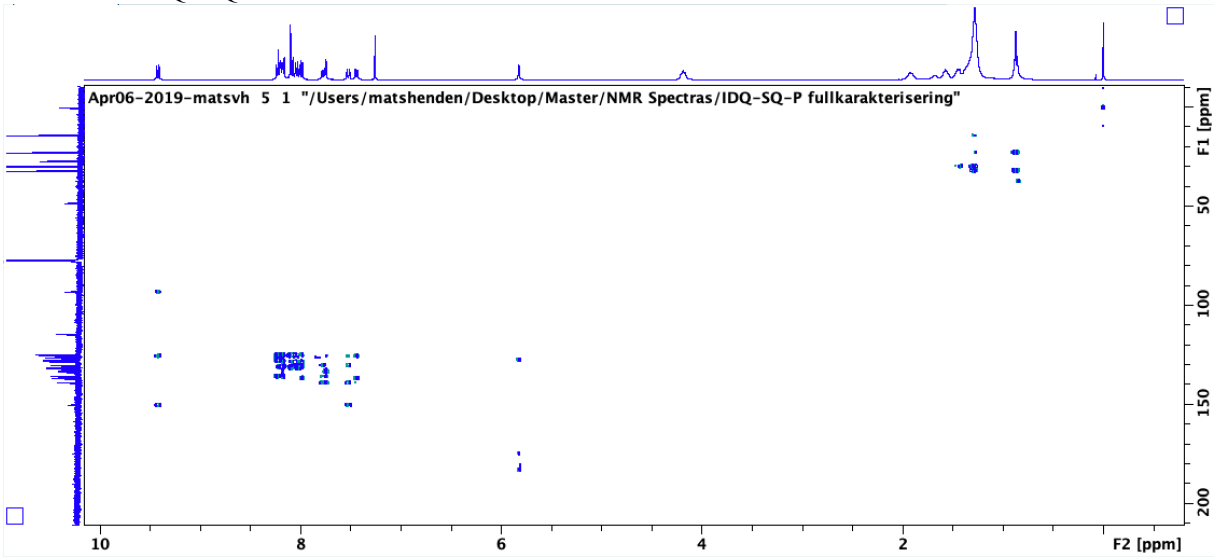

HMBC: IDQ-SQ-P

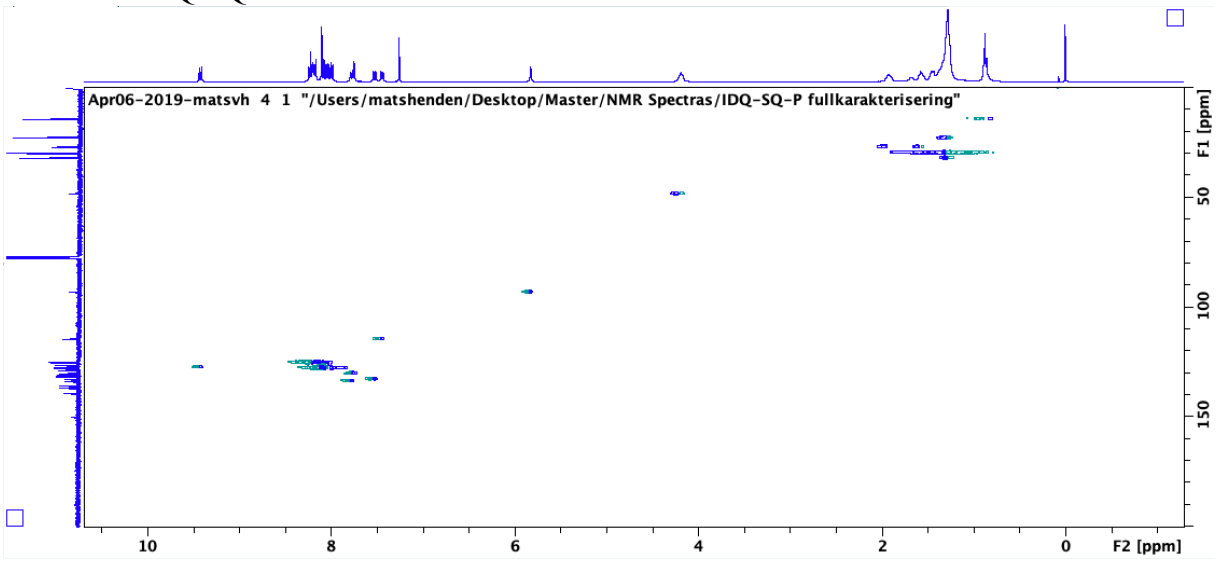

HSQC: IDQ-SQ-P

IPQ-SQ-P H-NMR Data

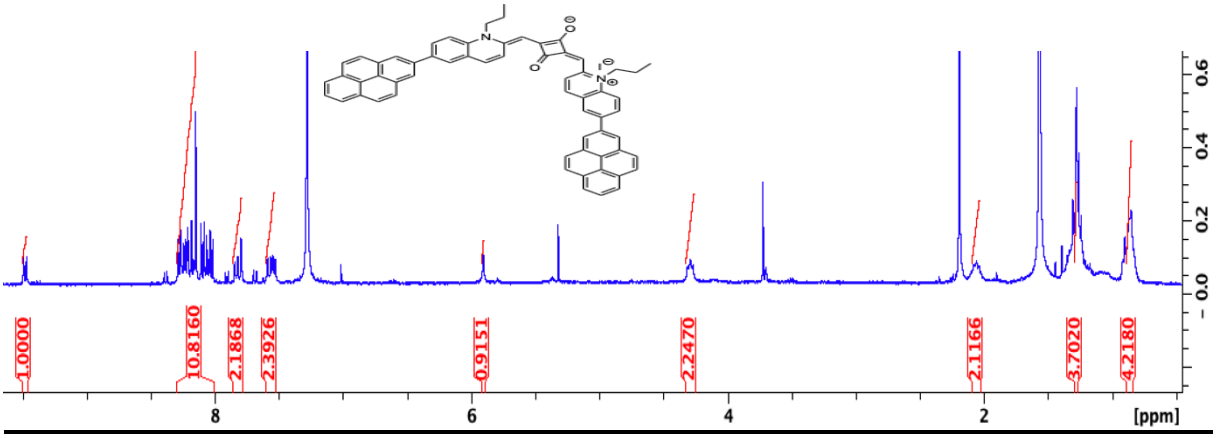

H-NMR Full Spectrum : IPQ-SQ-P

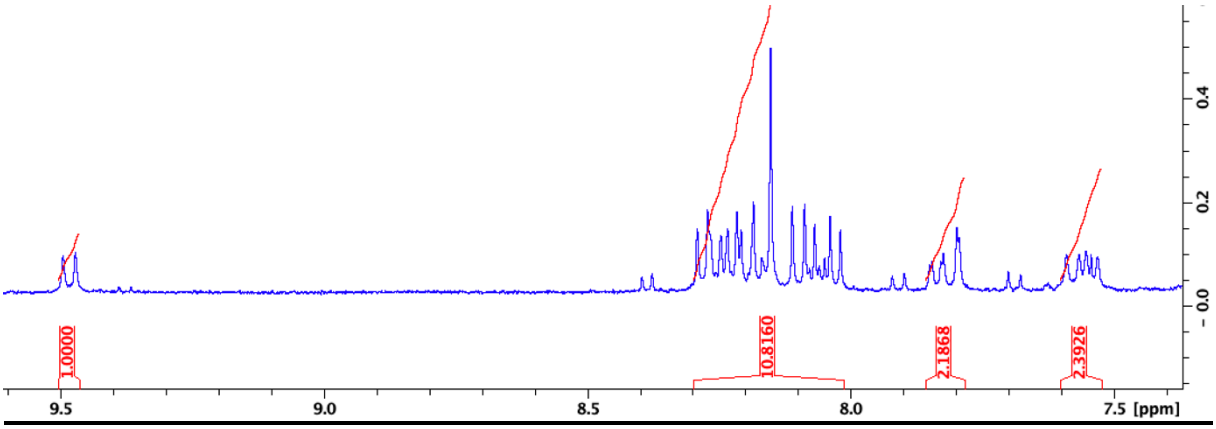

H-NMR Zoomed : IPQ-SQ-P

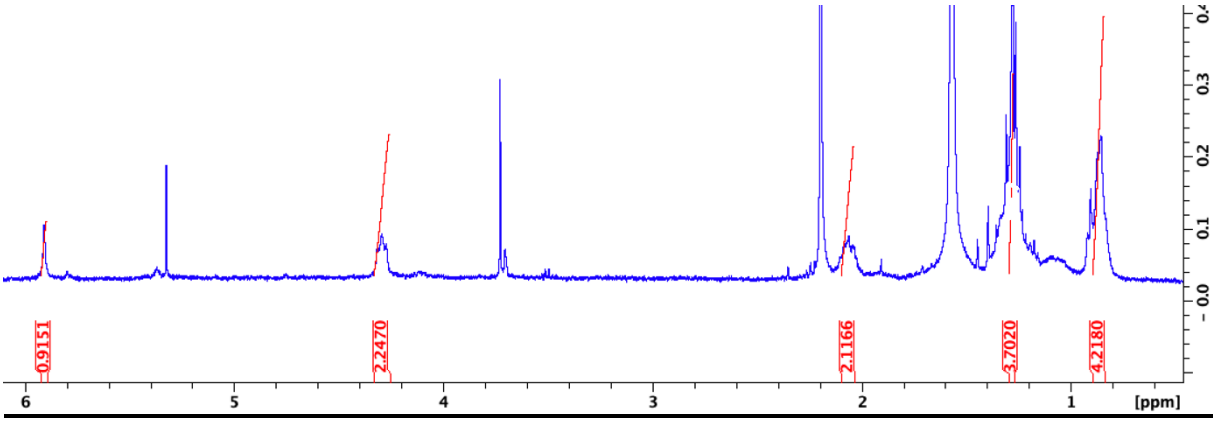

H-NMR Zoomed : IPQ-SQ-P

IDQ-SQ H-NMR Data

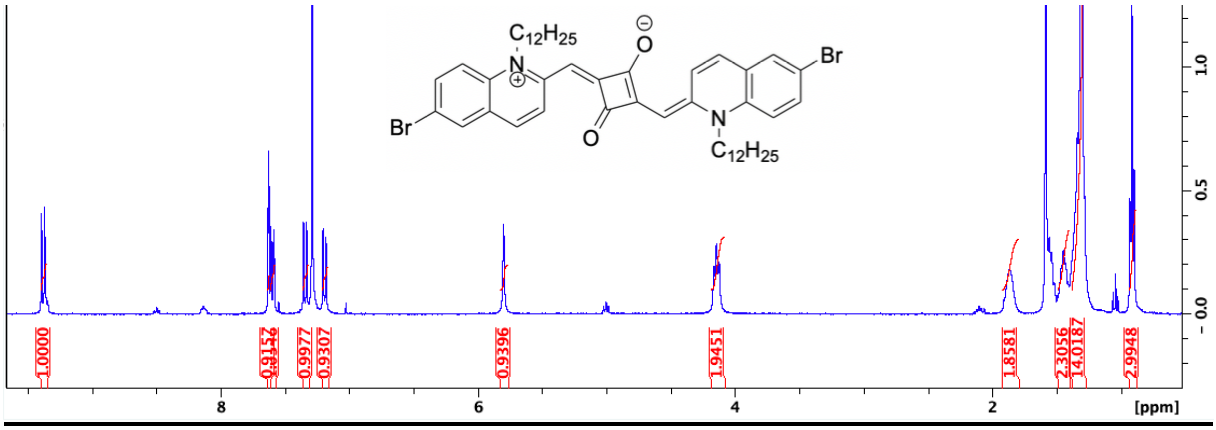

H-NMR Full Spectrum : IDQ-SQ

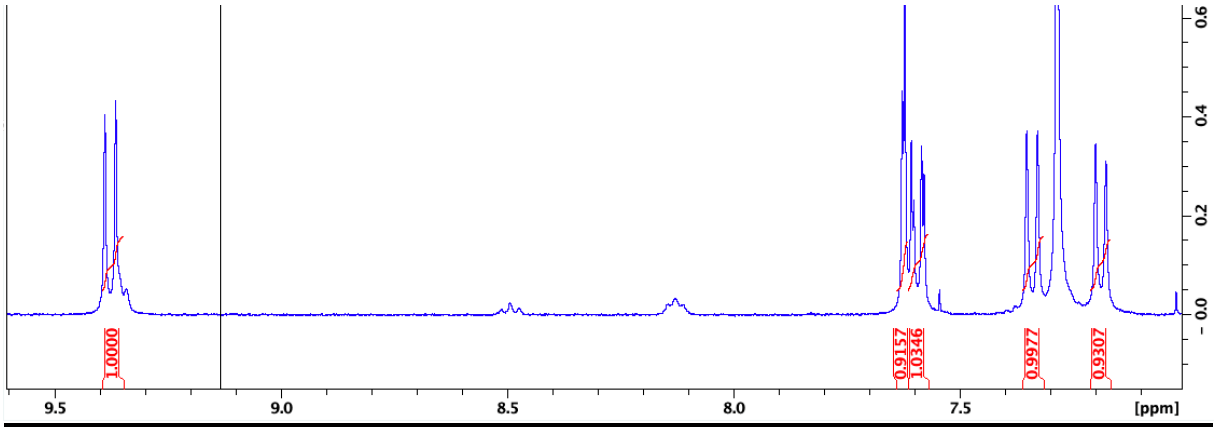

H-NMR Zoomed : IDQ-SQ

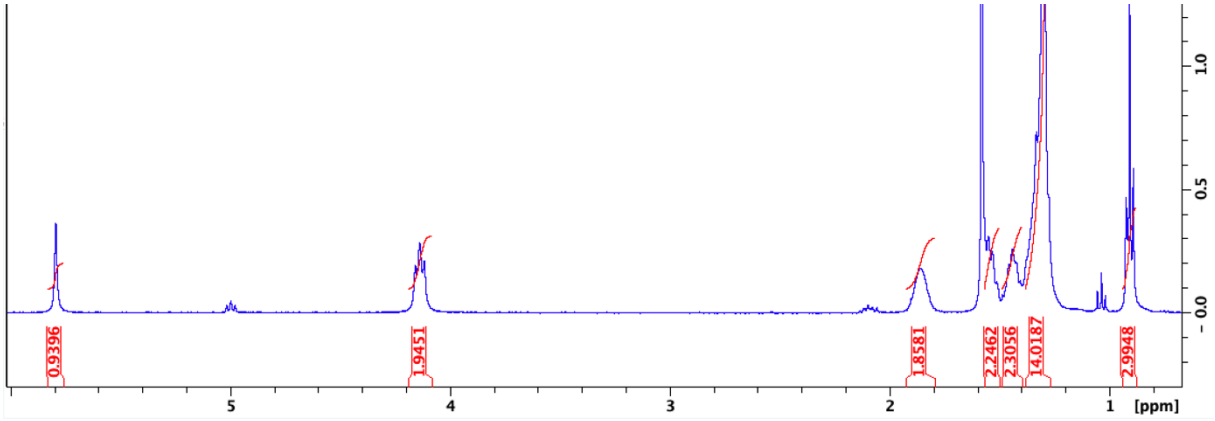

H-NMR Zoomen : IDQ-SQ

IPQ-SQ H-NMR Data

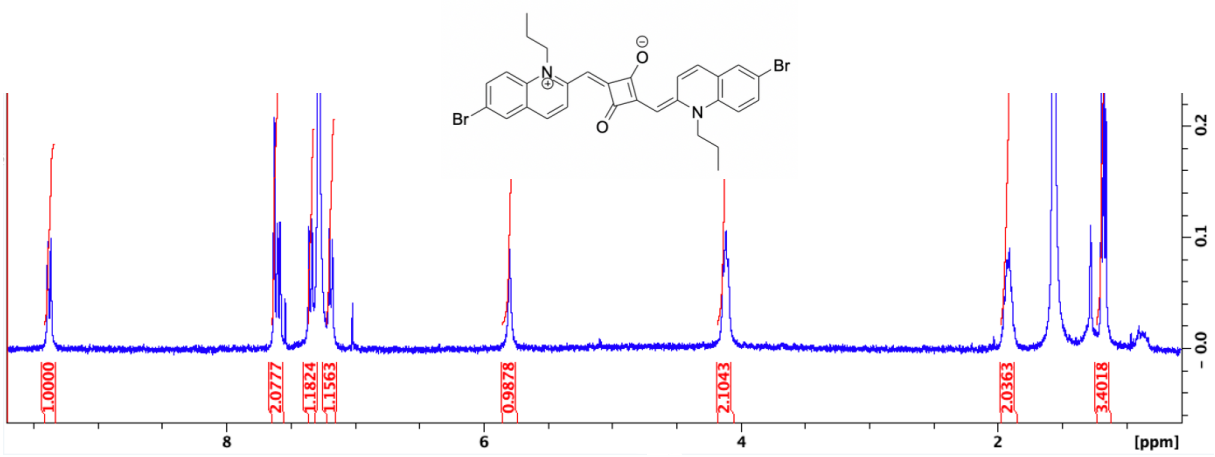

H-NMR Full Spectrum : IPQ-SQ

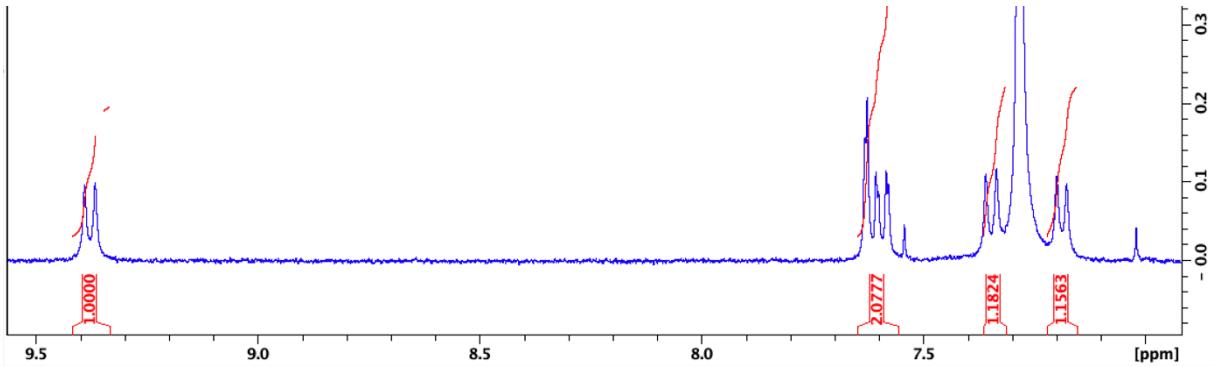

H-NMR Zoomed : IPQ-SQ

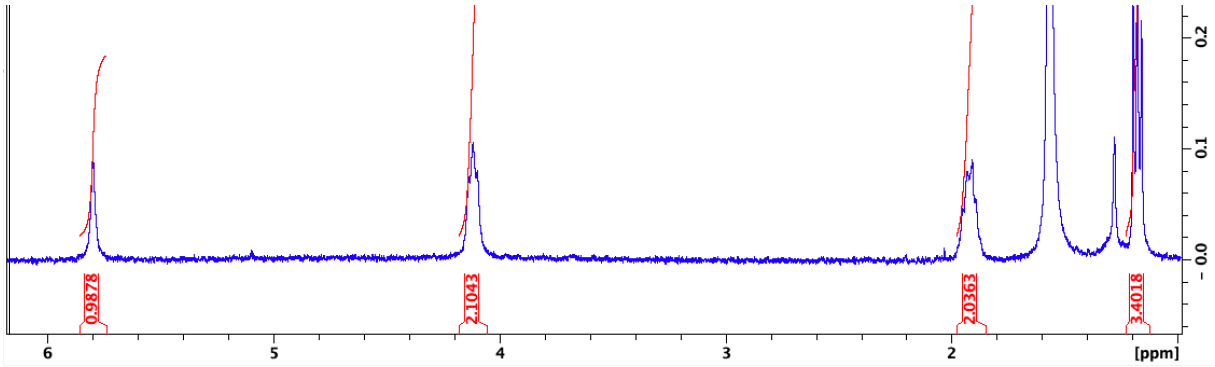

H-NMR Zoomed : IPQ-SQ

IDQ H-NMR Data

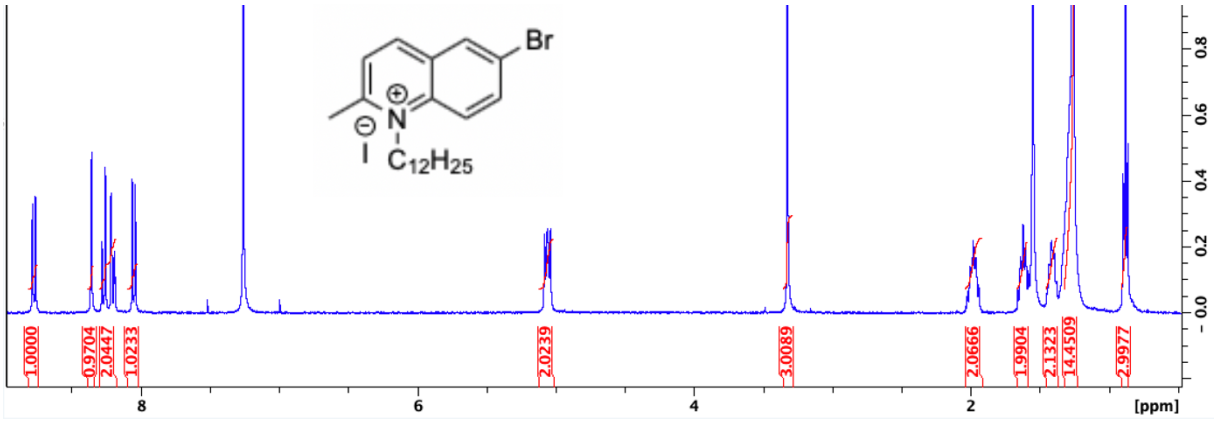

H-NMR Full Spectrum : IDQ

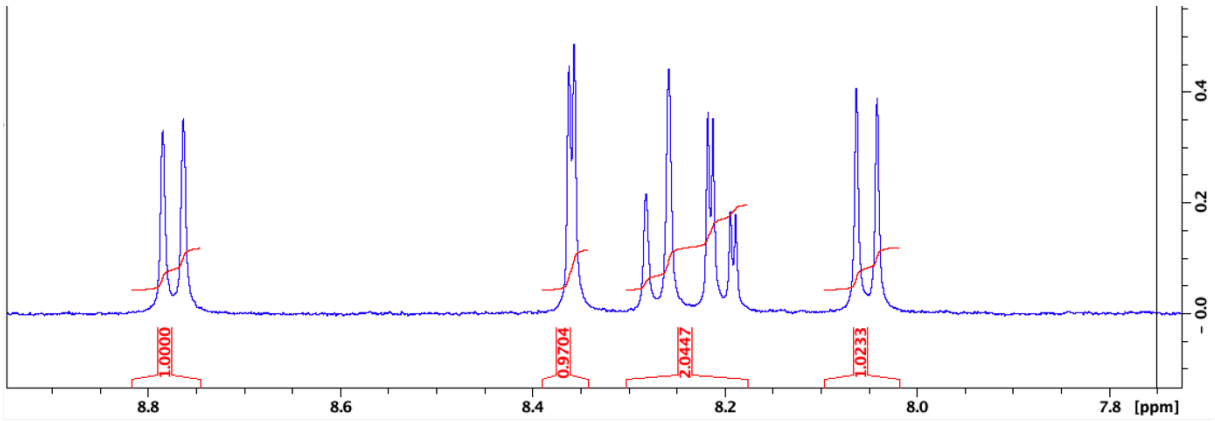

H-NMR Zoomed : IDQ

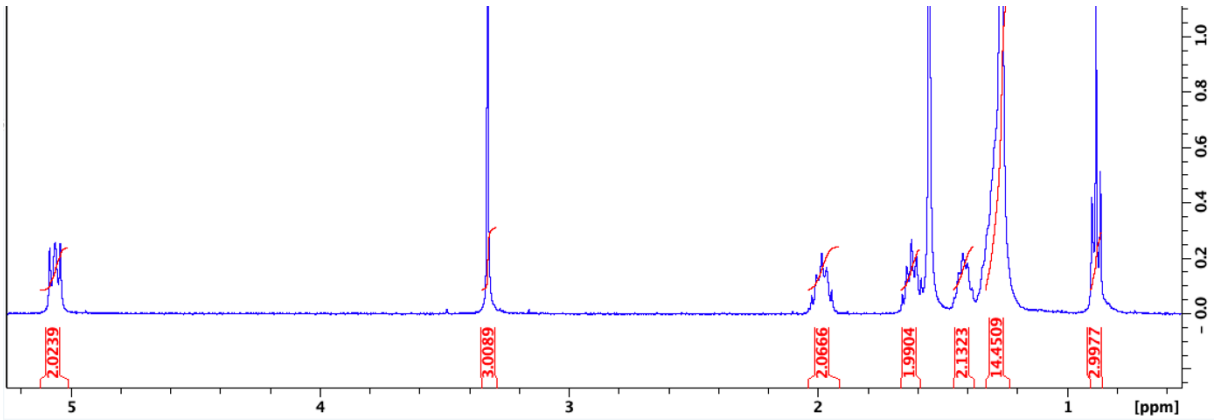

H-NMR Zoomed : IDQ

IPQ H-NMR Data

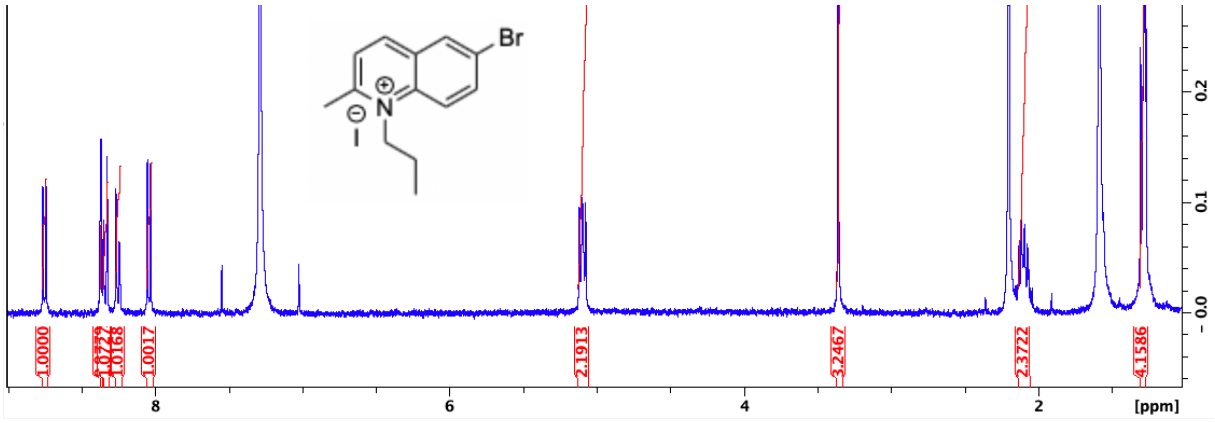

H-NMR Full Spectrum : IPQ

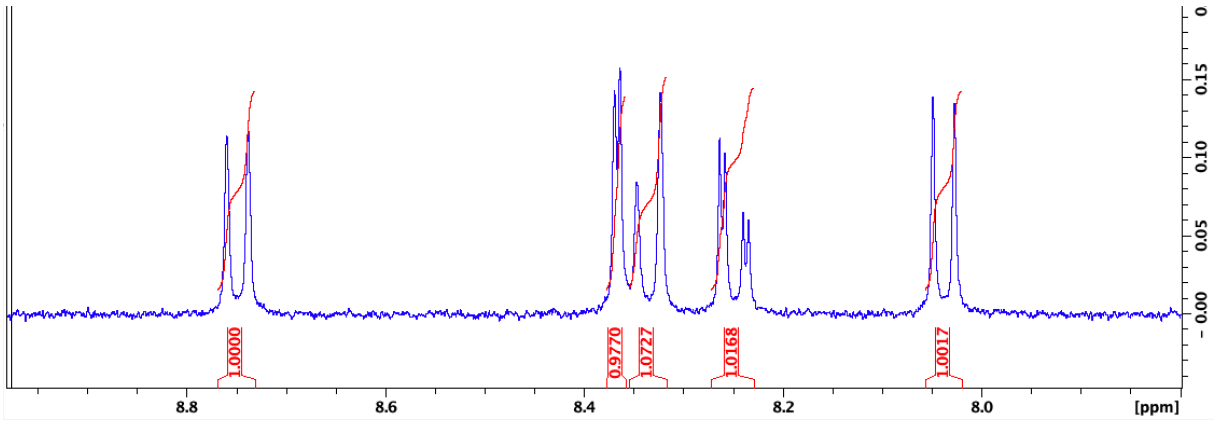

H-NMR Zoomed : IPQ

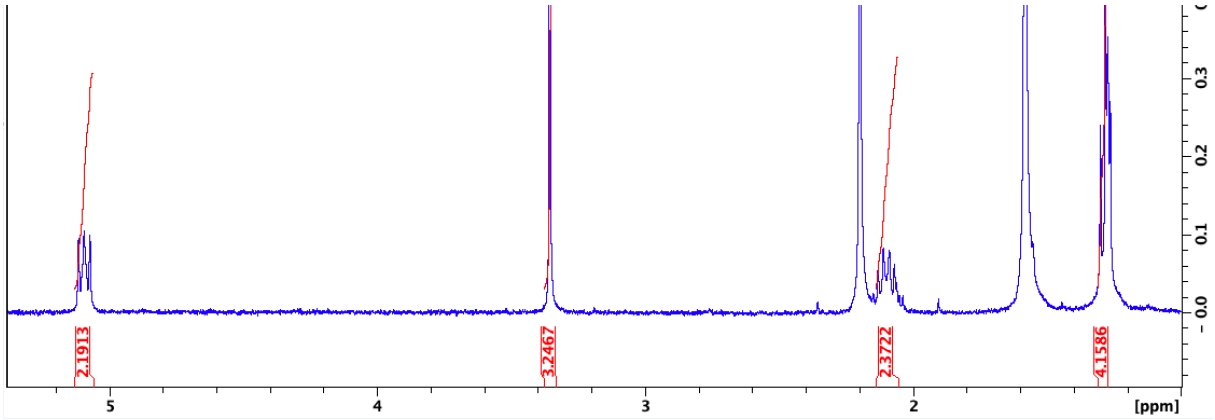

H-NMR Zoomed : IPQ